UNIVERSIDADE FEDERAL DE PERNAMBUCO
DEPARTAMENTO DE FÍSICA – CCEN
PROGRAMA DE PÓS-GRADUAÇÃO EM FÍSICA

LUIS FERNANDO MUÑOZ MARTÍNEZ

GENERATION AND CHARACTERIZATION OF MORE COMPLEX NON-CLASSICAL LIGHT STATES

Recife
2018

LUIS FERNANDO MUÑOZ MARTÍNEZ

GENERATION AND CHARACTERIZATION OF MORE COMPLEX NON-CLASSICAL LIGHT STATES

Tese apresentada ao Programa de Pós-Graduação em Física da Universidade Federal de Pernambuco, como requisito parcial para a obtenção do título de Doutor em Física.

Orientador: Prof. Dr. Daniel Felinto Pires Barbosa

Recife
2018

Catalogação na fonte
Bibliotecária Elaine Cristina de Freitas CRB4-1790

M967g Muñoz Martínez, Luis Fernando
Generation and characterization of more complex non-classical light states / Luis Fernando Muñoz Martínez. – 2018.
118 f., fig.

Orientador: Daniel Felinto Pires Barbosa
Tese (doutorado) – Universidade Federal de Pernambuco. CCEN. Física. Recife, 2018.
Inclui referências.

1. Física quântica. 2. Enmaranhamento. 3. Estado quântico I. Barbosa, Daniel Felinto Pires (Orientador) II. Título.

539 CDD (22. ed.) UFPE-FQ 2018-31

LUIS FERNANDO MUÑOZ MARTÍNEZ

GENERATION AND CHARACTERIZATION OF MORE COMPLEX NON-CLASSICAL LIGHT STATES

Tese apresentada ao Programa de Pós-Graduação em Física da Universidade Federal de Pernambuco, como requisito parcial para a obtenção do título de Doutor em Física.

Aprovada em: 20/04/2018

BANCA EXAMINADORA

Prof. Dr. Daniel Felinto Pires Barbosa
Orientador
Universidade Federal de Pernambuco

Prof. Dr. Fernando Roberto de Luna Parisio Filho
Examinador Interno
Universidade Federal de Pernambuco

Prof. Dr. José Wellington Rocha Tabosa
Examinador Interno
Universidade Federal de Pernambuco

Prof. Dr. Marcelo Paleologo Elefteriadis de França Santos
Examinador Externo
Universidade Federal do Rio de Janeiro

Prof. Dr. Marcos César Santos Oriá
Examinador Externo
Universidade Federal Rural de Pernambuco

Dedicada a Guerly María Angel

Agradecimentos

Ao concluir este trabalho quero agradecer aos que tornaram possível a realização desta experiência na minha vida acadêmica: a Deus e a minha família por me darem forças para alcançar este sonho. Foi um caminho difícil e de muitas batalhas e que sem sua ajuda eu não haveria conseguido.

Menciono também com muito entusiasmo a meus dois excelentes orientadores: Daniel Felinto e Alessandro Villar, os quais me deram a oportunidade de trabalhar com êxito em três diferentes problemas dentro da Ótica Quântica, embora não tenha sido este o plano inicial. Admiro muito a capacidade de ambos para intuir e enfrentar novos desafios científicos além de serem formidáveis no âmbito pessoal.

Ao Prof. Marcelo Martinelli agradeço pela a sua atuação como um terceiro orientador ajudando-me, entre outras coisas, a desenvolver com êxito o modelo de fônons para o OPO. Para mim foi um prazer trabalhar ao lado deste cientista brasileiro de grande prestigio.

Aos membros da banca de avaliação obrigado por me concederem a oportunidade de apresentar nosso trabalho para estes que são grandes cientistas. Ao mesmo tempo agradeço com atenção aos colaboradores deste trabalho: Felippe Barbosa, Antonio Coelho, David Barros, Jefferson Filgueiras, Paulo Saldanha e Paulo Nussenzveig.

Minha gratidão ao meu amigo e colega de experimento: Luis Gustavo Ortiz, pelas experiências compartilhadas ao longo deste processo. Alguns dos resultados presentes nesta tese não seriam possíveis sem a sua presença, eles que foram frutos de inúmeras e agradáveis conversas durante os longos meses que estivemos realizando as medições em laboratório.

Aos amigos que contribuíram nesta caminhada, seja na universidade ou ajudando na adaptação em Recife: Jamerson, Myrelle, André, Renata, Ariday, Fania, Pablo, Lesli, Hugo, Saira, Osvaldo, Johan, Edwin, Oscar, Lucero, Edinson, Russita, Bethe, Alejandro, Wilmer, Julian, Iván, Melissa, Raoni, Alyson, entre outros, bem como os integrantes da Comunidade Neocatecumenal em Recife que se tornaram parte da minha família.

Por fim, meus agradecimentos ao CNPQ pelo apoio financeiro através da bolsa acadêmica de doutorado e à Univerisidade Federal de Pernambuco, instituição onde se realizou todo este trabalho.

A todos meus votos de estima e o meu mais sincero agradecimento. Muito Obrigado!

Abstract

In this thesis, two optical systems that generate non-classical states of light were studied: a triply resonant Optical Parametric Oscillator (OPO) operating above the threshold and a cold atomic ensemble of neutral ^{87}Rb atoms obtained from a magneto-optical trap. The main idea in both cases is to prepare entangled states for future use in quantum information protocols. In relation to the OPO, experimental measurements of the complete quantum state for six modes of the electromagnetic field produced by this system are theoretically explained. The investigation involves the sidebands of the intense pump, signal and idler fields generated by stimulated parametric down-conversion inside the resonator. The model takes into account the coupling of the field modes with the phonon bath of the nonlinear crystal, clearly showing the roles of different physical effects in shaping the structure of the quantum correlations between the six optical modes. Moreover, it is theoretically and experimentally studied how these modes are entangled to one another using the positive partial transpose criterion in the continuous variables regime. It was found that the hexapartite entanglement in this system can be thought of as being generated by a combination of two-mode squeezers and beam splitter Hamiltonians acting on six different colors of light. On the other hand, in relation to the cold atomic ensemble, a "write-read" scheme inspired by the Duan-Lukin-Cirac-Zoller (DLCZ) protocol for long-distance quantum communication was implemented in order to experimentally generate an entangled state between individual photons of a mode of the electromagnetic field and atomic excitations in a particular collective mode. By performing photon statistics analysis it was possible to determine that the quantum state of the system corresponds to an entangled two-mode squeezed vacuum state, as expected from the theory. In the experiments, either one or two excitations are initially stored in the atomic medium, which acts as a quantum memory, and are subsequently mapped to one or two photons, respectively. Moreover, measurements and theoretical modeling of the photonic wave packets were realized, observing an acceleration in the photon emission due to the collective nature of the atomic state, a phenomenon known as *superradiance*. Such progress opens the way to the study and future control of the interaction of nonclassical light modes with collective quantum memories at higher photon numbers.

Keywords: Entanglement. Quantum state. Superradiance.

Resumo

Nesta tese foram estudados dois sistemas óticos geradores de estados da luz não clássicos: um oscilador paramétrico ótico (OPO) triplamente ressonante que opera acima do limiar e um ensamble atômico frio de átomos de ^{87}Rb neutros obtido a partir de uma armadilha magneto-ótica. A ideia principal em ambos os casos é preparar estados emaranhados para uso futuro em protocolos de informação quântica. Em relação ao OPO, medições experimentais do estado quântico completo, para os seis modos do campo eletromagnético produzido por este sistema, são explicadas teoricamente. A investigação envolve as bandas laterais dos campos de bombeio, sinal e complementar gerados por conversão paramétrica descendente espontânea dentro do ressonador. O modelo leva em consideração o acoplamento dos modos do campo com o banho de fônons do cristal não-linear, mostrando claramente os papéis dos diferentes efeitos físicos na formação da estrutura das correlações quânticas entre os seis modos ópticos. Além disso, é estudado teórica e experimentalmente como esses modos estão emaranhados entre si fazendo uso do critério de transposição parcial positiva no regime de variáveis contínuas. Verificou-se que o emaranhamento hexapartite neste sistema pode ser pensado como sendo gerado por uma combinação de Hamiltonianas de compressão de dois modos e de divisores de feixes que atuam sobre seis cores diferentes da luz. Por outro lado, em relação ao ensemble atômico frio, foi implementado um esquema de "leitura-escrita" inspirado no protocolo de Duan-Lukin-Cirac-Zoller (DLCZ) para comunicação quântica de longas distâncias com o fim de gerar experimentalmente um estado emaranhado entre fótons individuais de um modo do campo eletromagnético e excitações atômicas em um modo coletivo particular. Fazendo uma análise da estatística dos fótons foi possível determinar que o estado quântico do sistema corresponde a um estado de vácuo comprimido de dois modos, como esperado pela teoria. Nos experimentos, uma ou duas excitações são inicialmente armazenadas no meio atômico, que atua como memória quântica, e posteriormente são mapeadas para um ou dois fótons, respectivamente. Além disso, foram realizadas medições e uma modelagem teórica dos pacotes de ondas fotônicos, observando-se uma aceleração na emissão de fótons devido à natureza coletiva do estado atômico, um fenômeno conhecido como *superradiância*. Tal progresso abre o caminho para o estudo e controle futuro da interação de modos da luz não-clássica com memórias quânticas coletivas em números de fótons mais altos.

palavras-chave: Enmaranhamento. Estado quântico. Superradiância.

List of Figures

List of Acronyms

DLCZ protocol: Duan-Lukin-Cirac-Zoller protocol

SPDC: Spontaneous Parametric Down Conversion

OPO: Optical Parametric Oscillator

APD: Avalanche Photodiode Detectors

MOT: Magneto-Optical Trap

PPT criterion: Positive Partial Transpose criterion

PT: Partial Transposition

FSR: Free Spectral Range

HD: Homodyne Detection

RD: Resonator Detection

CAEs: Collective Atomic Excitations

FBS: Fiber Beam Splitter

PBS: Polarizing Beam Splitter

AOMs: Acoustic-Optic Modulators

OD: Optical Depth

TGR: Twin Generation Rate

TMD apparatus: Time-Multiplexing detection (TMD) apparatus

EIT: Electromagnetically Induced Transparency

Contents

1 Introduction

In the field of quantum optics, two of the most important systems used to generate nonclassical states of light, as basic elements for quantum information processing, are the Optical Parametric Oscillator (OPO) and cold atomic ensembles.

The OPO consists of a nonlinear crystal that couples three modes of a cavity through the spontaneous parametric down conversion (SPDC) process (Fig. 1). This nonlinear coupling provides the creation (or annihilation) of downconverted photon pairs (modes 1 and 2), through the annihilation (or creation) of a photon in the pump mode 0. Since the pumped nonlinear crystal acts as a gain medium, if this gain matches the cavity losses, the system gets into an oscillatory regime with the generation of intense output beams. By controlling the pump power, it is possible to explore a wide set of different states of light. The long list includes squeezed states [Wu 1986a], intense twin beams [Heidmann 1987], entangled vacuum [Ou 1992], squeezed pump field [Kasai 1997, Zhang 2001], entangled beams [Villar 2005], three mode quantum correlations [Cassemiro 2007] and three mode multicolor entanglement [Coelho 2009]. The field modes produced by the OPO contain intricate quantum properties that are not yet completely understood, both in theory and in experiment.

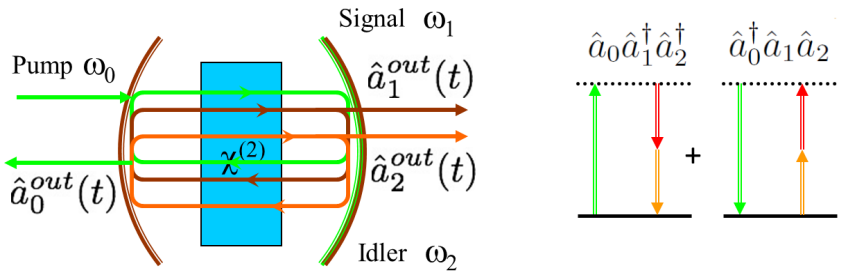

Figure 1: The basic optical parametric oscillator consists in one triply resonant cavity with a nonlinear crystal, that is responsible for coupling the pump mode (0) to the signal (1) and idler (2) downconverted modes. On the left side, the incoming pump field with frequency ω_0 produces one output signal field $\hat{a}_1^{out}$ and one idler field $\hat{a}_2^{out}$, with frequencies ω_1 and ω_2, respectively. A part of the pump field, $\hat{a}_0^{out}$, is reflected from the cavity. On the right side, the nonlinear coupling provides the creation (or annihilation) of downconverted photon pairs, through the annihilation (or creation) of a photon in the pump mode.

The applications of these nonclassical states in the continuous variable domain goes

from the use of squeezing for ultra-sensitive measurements [Caves 1981,Collaboration 2011] to the demands for entanglement in quantum information processing [Furusawa 1998], with convergence of experiments for discrete and continuous variables of the electromagnetic field [Takeda 2013]. Moreover, multimode entangled states in the continuous variable domain are interesting candidates for quantum information processing [Chen 2014], leading to the search of sources involving modes defined either in time [Yokoyama 2013], frequency [Pinel 2012, Chen 2014] or momentum [Wang 2017].

The fundamental process for the generation of these nonclassical states of light is the reversible exchange of energy among the pump field and the two downconverted modes. With the aid of optical cavities, this effect is enhanced, and the output states can be calculated with the help of the input-output formalism for optical cavities and the master equation of the interacting Hamiltonian for the three modes of the field [Reid 1988, Reid 1989].

Nevertheless, a detailed investigation over the detection process leads to a more complete description of the quantum state represented in the basis of field quadratures [Barbosa 2013c]. In fact, optical detection is generally based in interferometric techniques, either by optical homodyning or by resonator self-homodyning [Barbosa 2013b]. On the other hand, the measured quantum noise of light is analyzed in the frequency domain with the help of an electronic local oscillator to filter the contribution at a given frequency, associated with the sidebands of the optical field. Therefore, with careful data treatment, it can be shown that although the three mode description remains a valid approach, a more complete one can be obtained for the six detected modes of the field.

In relation to this system, the principal goal of this thesis is to present an explicit evaluation of the quantum state for the six sideband modes of the OPO that are measured by homodyne techniques and try to access modal correlations that cannot be available in the simplified three-mode picture of single-beam quantum fluctuations (pump, signal and idler). By explicitly using frequency modes of the field in the Hamiltonian, we are able to deal with open cavities, looking for a more faithful description of the optical setups usually involved in the nonclassical state generation. Moreover, the detailed sideband description puts in evidence the role of each field in the evolution of the system, something that remained implicit in the standard treatment [Reid 1988, Reid 1989]. This six mode description allows the complete analysis of entanglement in the OPO, demonstrating a deep hexapartite entangled structure for this system. This will also be treated in detail in this thesis.

On the other hand, cold atomic ensembles are currently one of the most advanced systems for the quantum control of light-matter interaction at the single excitation level. They are usually used to create quantum memories which can faithfully store and retrieve quantum information encoded in photons. These memories are essential building blocks for scalable quantum technologies involving photons, such as linear optics

quantum computing and long-distance quantum communication using quantum repeaters [Briegel 1998, Duan 2001, Sangouard 2011].

Atomic ensembles provide an efficient way of reaching the strong interaction between matter and light required for the implementation of quantum memories, without the need for high-finesse cavities. In addition, they give the possibility to multiplex quantum information, e.g. transmit information from multiple users on a single optical channel, which is desirable in several applications. In particular, in quantum repeater architectures, this alleviates the limitation due to the communication time between the nodes [Simon 2007a]. In atomic ensembles, quantum information is stored as Collective Atomic Excitations (CAEs). Single CAEs offer the important advantage that they can be efficiently transferred to single photons in a well-defined spatial-temporal mode thanks to constructive interference between the involved atoms. The single CAE can be prepared by heralding on detection of a photon that has undergone Raman scattering from an atomic ensemble, according to the Duan, Lukin, Cirac, and Zoller (DLCZ) protocol [Duan 2001]. The Hamiltonian governing the Raman scattering event is identical to that of SPDC, leading to the production of an entangled state of the scattered light and the CAE, the so-called *two-mode squeezed vacuum state*. While DLCZ utilizes only the first-order term of the evolution under this Hamiltonian, higher-order terms can be used in combination with more complex measurements on the scattered optical mode to produce arbitrary quantum CAE states in a way similar to how it is done in systems based on SPDC [Ourjoumtsev 2006, Bimbard 2010, Cooper 2013].

Once the desired collective state has been produced, it needs to be measured. Therefore, the readout stage of the DLCZ protocol may be used, in which the CAE is converted into the optical domain in a manner similar to readout from a quantum optical memory based on Electromagnetically Induced Transparency (EIT) [Fleischhauer 2000].

Several demonstrations of the building block of the DLCZ protocol have been reported [Kuzmich 2003, Chou 2005, Choi 2008, Radnaev 2010] including functional elementary segments of a quantum repeater [Chou 2007, Yuan 2008]. Most of these demonstrations, however, used only one CAE per ensemble, although several ensembles have been already implemented in the same atom trap [Lan 2009, Choi 2010, Pu 2017]. In this thesis we move further by exploring the DLCZ protocol in the two-CAEs regime. In our experiments, the cold atomic ensemble is created by a Magneto-Optical Trap (MOT) and either one or two CAEs are initially stored in the atomic memory. The readout process results in the enhanced emission of one or two photons, respectively, with properties that depend on the quantum state of the memory. This phenomenon of enhanced photon emission from an ensemble of atoms is known as *superradiance* [Dicke 1954] and highlights the coherent nature of spontaneous emission [1]. Due to superradiance, the photon emission in

[1] The first superradiance observations were reported in the 1970s using extended ensembles [Skribanowitz 1973, Gross 1976] and although several of its features could be understood through classical

the read process is highly directional, what permits an efficient detection by selecting the appropriate mode. In relation to this system, our main purpose is to observe the increase of the photon emission rate due to superradiance in both the single- and two-CAEs regime, as well as the characterization of the Fock-state regimes with one or two photons being emitted by the memory. To do so, we measure the wavepackets of the single-photon and bi-photon emissions, evidencing superradiant acceleration in both cases, and perform a photon statistics analysis that indicates the presence of quantum correlations.

1.1 Thesis outline

The main results of this thesis are: on the one hand, the explicit evaluation of the quantum state for the six sideband modes of an OPO operating above the threshold and the exploration of the hexapartite entanglement in this system. On the other hand, the experimental characterization of the quantum state of an atomic memory containing up to two CAEs and the experimental study on one- and two-photon superradiance in this system.

This thesis is organized as follows: In chapter 2, there is a brief discussion about the concepts needed to derive the results of the thesis. In chapter 3, the theory fully describing the quantum state of an OPO operating above threshold is developed. Moreover, a study of hexapartite entanglement in this system is also developed. In chapter 4, we report a series of experiments for the simultaneous study of single- and two-photon superradiance and for the characterization of the quantum state of the atomic memory. Finally, in chapter 5, the conclusions and perspectives on each of the studied systems are presented.

models [Gross 1982a], recent experiments, observing the superradiant collective acceleration of emission with just a single CAE participating in the process (single-photon superradiance) [Mendes 2013b, de Oliveira 2014], indicate that such classical analogues cannot be applied to describe the phenomenon. In fact, this single-photon superradiance is a direct manifestation of the wave-particle duality, with a single particle being emitted faster due to the interference of the probability amplitudes of emission by each atom. Such regime can be approximated by exciting an atomic sample with weak laser light [Roof 2016, Araújo 2016], although the photon statistics in this scheme do not present quantum correlations.

2 Fundamental concepts

In this chapter I briefly review the concepts used in the development of the ideas presented in the next chapters. The goal is not to give a broad overview on each of the addressed topics but to provide the reader with a more self-contained text and useful references.

2.1 Quantum entanglement

Quantum entanglement is a very particular kind of correlation that may exist between subsystems of a composite system, much stronger than any classical correlations. Quantum correlations, including quantum entanglement, seems to be one of the most intriguing problems of contemporary physics. Such correlations play a crucial role not only in searching for the answers to the most fundamental questions concerning the laws ruling quantum reality, but also in more practical applications such as those related to quantum information theory. In particular, in quantum information, entanglement is viewed as a resource, as in the protocols for quantum teleportation [Bennett 1993], superdense coding [Bennett 1992] or entanglement-based quantum cryptography (quantum communication) [Ekert 1991].

Entanglement between physical systems can occur in observables with discrete or continuous spectrum. In the first case, measurement results are restricted to a discrete set of values, not necessarily finite, such as the set of integers; in the second case, any subset of the real numbers can be obtained in a measurement. Examples of discrete observables are the spin and its projections on the spatial axes and the number of photons in the electromagnetic field. The position and momentum of a particle and the quadratures of the electromagnetic field are examples of continuous observables.

In this section, we begin by presenting the formal definition of quantum entanglement following the references [Villar 2007, Cavalcanti 2008] and subsequently the criterion that will be used in this thesis to identify the entanglement produced by an optical parametric oscillator.

2.1.1 *Formal definition of entangled states*

Quantum states are described by semi-definite positive operators of unity trace acting on a Hilbert space $\mathscr{H}$ known as the state space. Thus, an operator $\hat{\varrho} \in \mathcal{A}(\mathscr{H})$ (the Hilbert space of operators acting on $\mathscr{H}$) representing a quantum state satisfies: 1) $\langle\Psi|\hat{\varrho}|\Psi\rangle \geq 0$ for all vectors $|\Psi\rangle \in \mathscr{H}$, or, equivalently, if all eigenvalues are greater or equal zero, and 2) $\mathrm{Tr}(\hat{\varrho})$=1. Such operators are called *density matrices* or *density operators*. Any density operator can be written (non-uniquely) through convex combinations of one-dimensional projectors, namely,

$$\hat{\varrho} = \sum_i p_i |\psi_i\rangle\langle\psi_i|, \tag{2.1.1}$$

with

$$\sum_i p_i = 1 \qquad \text{and} \qquad p_i \geq 0. \tag{2.1.2}$$

A special case of representation Eq. (2.1.1) is when $p_i = 1$ for some i, so we can describe a quantum state by a unidimensional projector, i.e. $\hat{\varrho} = |\psi_i\rangle\langle\psi_i|$. In this case, $\hat{\varrho}$ is called a *pure state*. Pure states are the extreme points of the set of quantum states and then represent those systems from which we have the most complete information.

Systems composed by many subsystems 1, 2, ...,N are also represented by density operators, but now acting on a vectorial space $\mathscr{H}$ with a tensorial structure:

$$\mathscr{H} = \otimes_j^N \mathscr{H}_j = \mathscr{H}_1 \otimes \mathscr{H}_2 \otimes \ldots \otimes \mathscr{H}_N, \tag{2.1.3}$$

where $\mathscr{H}_1, \mathscr{H}_2, \ldots, \mathscr{H}_N$ are the state spaces for each subsystem.

The notion of entanglement appears in these composite spaces. Let me present the definition of entanglement and separability for these systems (also called *multipartite systems*):

Definition 1 - *Separability for multipartite systems*
Multipartite separable states are those which can be written as a convex combination of tensor products of density matrices, i.e.: $\hat{\varrho} \in \mathcal{A}(\otimes_j^N \mathscr{H}_j)$ is separable if

$$\hat{\varrho} = \sum_i p_i (\hat{\varrho}_i^{(1)} \otimes \hat{\varrho}_i^{(2)} \otimes \ldots \otimes \hat{\varrho}_i^{(N)}), \tag{2.1.4}$$

where $\{p_i\}$ is a probability distribution. Alternatively, states that cannot be written in this form are called entangled [Werner 1989]. In particular, when there is no partition that can be written separately from the rest using a product as above, then the system is said to have N-partite entanglement.

An example of a bipartite entangled state is

$$\hat{\varrho} = \frac{1}{2}\left(|00\rangle\langle 00| + |00\rangle\langle 11| + |11\rangle\langle 00| + |11\rangle\langle 11|\right). \tag{2.1.5}$$

Note that the entanglement definition, included in definition 1, is not operational since it does not provide a procedure that allows saying if a certain state can be written as given by Eq. (2.1.4). In fact, doing this is a hugely difficult problem from the computational point of view since in principle there are infinite bases on which it is possible to decompose a density matrix. Therefore, it is necessary to resort to entanglement criteria, which are directly applicable in an experimental context. Currently, there are several criteria for a wide range of applications. However, we will only discuss the criterion explicitly used in this thesis.

2.1.2 *Positive Partial Transpose (PPT) criterion*

In this subsection we will begin by presenting the entanglement criterion developed by Peres and Horodecki [Peres 1996, Horodecki 1996] for bipartite systems in the discrete variables regime and then the extension of it for the continuous variables regime developed by Simon [Simon 2000], saying in each case in which situations it is a necessary and/or sufficient criterion for a state to be entangled. This continuous-variables case is of special interest for this thesis since it will be used in chapter 3 to investigate how the entanglement is distributed among the different modes of the electromagnetic field generated by an optical parametric oscillator.

Discrete variables

PPT criterion (sometimes called Peres-Horodecki criterion) is a simple *separability condition* for a bipartite state. This criterion can be used for both pure and mixed states as well. It was first proposed as a necessary condition for every separable state by Asher Peres in 1996 [Peres 1996]. By being a necessary condition, it means that every separable state satisfy this condition, though some entangled states satisfy it as well. Later, Horodecki familiy studied the criterion in more details and discovered that it was not only a necessary but also sufficient condition for separable states of 2×2 and 2×3 dimensions. Thus for a bipartite qubit state (2×2 dimensions), this criterion can be exploited to confirm exactly whether a state is entangled or separable.

Following [Deesuwan 2010], the description and the principle underlying the criterion can be explained as follows. First, for every physical state, the density matrix must be positive-semidefinite, i.e. all of its eigenvalues must not be negative. Next, let us consider a separable bipartite system, i.e. where the density matrix that describes it can be written in the following way (see definition 1)

$$\hat{\rho} = \sum_i p_i \hat{\rho}^A \otimes \hat{\rho}^B. \tag{2.1.6}$$

where $\hat{\rho}^A$ and $\hat{\rho}^B$ are the density matrices that describe the A and B subsystems.

Let T be the usual transposition operator for matrices. Then to perform transposition on the first subsystem (Partial Transposition or PT) is equivalent to operate $T \otimes I$ on the whole system (I being the identity operator). This gives,

$$\hat{\rho}^{T_A} = (T \otimes I)\hat{\rho} = \sum_i p_i \left(\hat{\rho}^A\right)^T \otimes \hat{\rho}^B. \tag{2.1.7}$$

Because transposition does not change the eigenvalues of a matrix, $\left(\hat{\rho}^A\right)^T$ must still be positive-semidefinite. Thus, $\left(\hat{\rho}^A\right)^T$ is a valid density matrix representing a physical state. It implies directly that $\hat{\rho}^{T_A}$ is also a valid density matrix, representing a physical separable bipartite system and must be positive-semidefinite. This is the Peres's necessary condition:

Every physical separable bipartite density matrix, when a PT operation is applied, must still be a physical density matrix, i.e. all of its eigenvalues must still not be negative.
It was shown by Horodecki, as mentioned above, that this is also a sufficient condition for a two-qubit system which means any qubit state that do not satisfy this criterion is entangled.

Let us now make some comments on the PPT criterion:

- A very important characteristic of the PPT criterion is that eigenvalues of $\hat{\rho}^{T_A}$ are invariant for unitary transformations performed on $\hat{\rho}$ [Peres 1996]. This allows us to apply the criterion in any representation of $\hat{\rho}$.

- The PPT criterion cannot be implemented directly in the laboratory until after the density matrix has been reconstructed. This comes from the PT operation not being a physical transformation since it can map physical states (with positive probabilities) in non-physical states (with negative probabilities).

- The PPT criterion is very useful for the determination of entanglement for bipartite states with a discrete Hilbert space. However, when the Hilbert space increases, the application of this criterion becomes unfeasible. For systems of infinite dimension (continuous-variables regime), like to the one that we consider in the chapter 3, it is totally unfeasible to measure the density matrix. Therefore, instead of $\hat{\rho}$, quasi-probability representations are used that describe the system in the phase space. The adaptation of this criterion for the continuous-variables regime was done by Simon [Simon 2000]. In his article it is demonstrated that the PPT criterion continues to be valid for bipartite quantum systems, being still a necessary and sufficient criterion when the states in consideration are Gaussian. In what follows

we will explain very briefly the implementation of this criterion in the continuous-variables regime. For a more detailed discussion, we recommend consulting the references [Villar 2007, Cassemiro 2008a].

Continuous variables

Systems of continuous variables are constituted by observables whose spectra can assume continuous values. In general, these observables obey the rules of commutation for position and momentum, i.e.,

$$[\hat{q}^{(i)}, \hat{p}^{(j)}] = 2i\delta_{ij}, \tag{2.1.8}$$

where $i, j = 1, 2, \ldots, N$ for a system composed of N modes. In this context, these operators are known as amplitude ($\hat{p}^{(j)}$) and phase ($\hat{q}^{(j)}$) quadrature operators and they are related to the usual annihilation ($\hat{a}^{(j)}$) and creation ($\hat{a}^{(j)\dagger}$) operators as follows

$$\hat{p}^{(j)} = \hat{a}^{(j)} + \hat{a}^{(j)\dagger}, \qquad \text{and} \qquad \hat{q}^{(j)} = -i(\hat{a}^{(j)} - \hat{a}^{(j)\dagger}). \tag{2.1.9}$$

Following [Cassemiro 2008b], Gaussian states[1] are completely characterized by their second order moments, organized in the covariance matrix

$$\mathbf{V} = \left(\langle \vec{\mathbf{X}} \cdot \vec{\mathbf{X}}^T \rangle + \langle \vec{\mathbf{X}} \cdot \vec{\mathbf{X}}^T \rangle^T\right)/2, \tag{2.1.10}$$

where

$$\vec{\mathbf{X}} = (\hat{p}^{(1)}\ \hat{q}^{(1)}\ \hat{p}^{(2)}\ \hat{q}^{(2)} \cdots\ \hat{p}^{(N)}\ \hat{q}^{(N)})^T. \tag{2.1.11}$$

The canonical commutation relations can be written in the compact form as $[\vec{\mathbf{X}}, \vec{\mathbf{X}}^T] = 2i\mathbf{W}$, where

$$\mathbf{W} = \bigoplus_{j=1}^{N} \mathbf{w}, \qquad \mathbf{w} = \begin{pmatrix} 0 & 1 \\ -1 & 0 \end{pmatrix}. \tag{2.1.12}$$

With the purpose of representing a physical state, the covariance matrix must obey the Heisenberg uncertainty principle [Simon 1987, Simon 1994],

$$\mathbf{V} + i\mathbf{W} \geq 0, \tag{2.1.13}$$

which implies a condition in the symplectic eigenvalues $\nu^{(k)}$ of the covariance matrix

$$\nu^{(k)} \geq 1, \qquad k = 1, 2, \ldots, N. \tag{2.1.14}$$

The symplectic eigenvalues of the covariance matrix can be obtained as the square roots

[1] The state of a continuous variable system with N degrees of freedom is called Gaussian if its Wigner function , or equivalently its characteristic function, is Gaussian.

of the ordinary eigenvalues of $-(\mathbf{WV})^2$.

As discussed above, the PPT criterion in the discrete-variables domain relies on the positivity of the partially transposed density matrix [Peres 1996], that could be used to test the entanglement among all possible bipartitions of a system, this map is positive for all separable states, however may be negative to entangled states. In continuous-variables domain it is equivalent to a local inversion of time for the transposed subsystems [Simon 2000] in phase space. In this case, the PT operation over the covariance matrix turns $\hat{q}^{(n)}$ into $-\hat{q}^{(n)}$ for a determined subset of modes. Therefore, the PPT criterion in continuous-variables domain establishes the following: if the resulting PT covariance matrix $\tilde{V}$, violates the inequality of Eq. (2.1.13), then we have a sufficient condition for the existence of entanglement among the transposed subset of modes and the remaining subset [Simon 2000], or equivalently, the symplectic eigenvalues must violate Eq. (2.1.14) in this case. The PPT criterion is both necessary and sufficient for pure or mixed states in partitions $1 \times (N-1)$ [Simon 2000, Werner 2001]. Other partitions may posses bound entanglement, nevertheless it is always sufficient.

The smallest symplectic eigenvalues $\tilde{\nu}_{\min}$ of the PT covariance matrix is useful not only to witness the entanglement but also to quantify it. In fact, the entanglement measure given by the logarithmic negativity [Vidal 2002] can be written as a decreasing function of $\tilde{\nu}_{\min}$, for all $(M+N)$-mode bisymmetric Gaussian state [Adesso 2004]. Thus, a larger violation of Eq. (2.1.14) implies a larger amount of entanglement.

In conclusion, we have an easily implemented criterion that will allow us to identify the entanglement produced by one of the systems of interest in this thesis, an Optical Parametric Oscillator. The results of this implementation are presented in the chapter 3.

2.2 Fabry-Perot cavity

Following closely the discussion in [Barbosa 2013a], a Fabry-Perot cavity is formed by a coupling mirror and an end mirror, with reflection coefficients r and r', respectively, which are separated by a distance L, as shown in Fig. 2. The reflection coefficients are related to the transmission coefficients as $r^2 + t^2 = 1$ and $r'^2 + t'^2 = 1$.
When a field α_{in} with frequency $\omega = kc$ strikes the cavity, a fraction of it is reflected directly by the coupling mirror while the rest is transmitted, entering the cavity. After a round trip through the cavity, part of this field is transmitted by the coupling mirror (the other part was transmitted by the end mirror) and is superimposed on the reflected field directly. The remaining part is reflected and propagates in a second round. This process is repeated successively until reaching a steady state.

In order to know how the fields shown in Fig. 2 are related, we consider that each mirror of the cavity behaves like a beam beam splitter (see Fig. 3), whose transformation is given by [Walls 2008]:

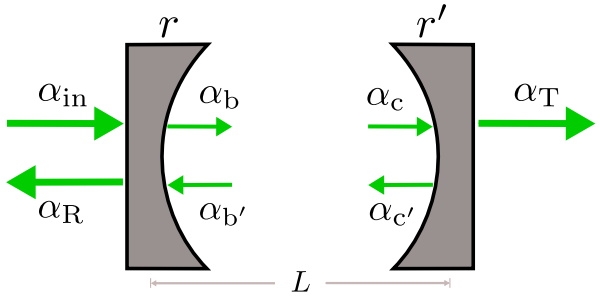

Figure 2: Fabry-Perot cavity. It is composed by a coupling mirror (left) and an end mirror (right), with reflection coefficients r and r', respectively, which are separated by a distance L. The difference in the trajectory of the fields that propagate inside and outside the cavity is only illustrative. In a real cavity, these fields are overlapped.

$$g = r \cdot f + t \cdot e, \qquad h = t \cdot f - r \cdot e. \tag{2.2.1}$$

So, the equations relating each field operator inside and outside the cavity (Fig. 2) in the steady-state regime are given by

$$\alpha_{\mathrm{R}} = r\alpha_{\mathrm{in}} + t\alpha_{b'}, \qquad \alpha_b = t\alpha_{\mathrm{in}} - r\alpha_{b'}, \tag{2.2.2}$$

$$\alpha_{\mathrm{T}} = t'\alpha_c, \qquad \alpha_{c'} = -r'\alpha_c. \tag{2.2.3}$$

Under free space propagation, the intracavity operators are related by a phase factor

$$\alpha_c = e^{-ikL}\alpha_b, \qquad \alpha_{b'} = e^{-ikL}\alpha_{c'}, \tag{2.2.4}$$

depending on the wavelength k and on the optical distance L between the cavity mirrors.

Using the expressions given in Eq. (2.2.4) it is easy to solve the set of equations (2.2.2) and (2.2.3) for the fields α_R and α_T as a function of the incident field α_{in}. The solution is

$$\alpha_{\mathrm{R}} = r_{kL}\alpha_{in}, \qquad \text{and} \qquad \alpha_T = t_{kL}\alpha_{in}, \tag{2.2.5}$$

where the reflection and transmission coefficients of the cavity are given by

$$r_{kL} = \frac{r - r'e^{-2ikL}}{1 - rr'e^{-2ikL}}, \qquad \text{and} \qquad t_{kL} = \frac{tt'e^{-ikL}}{1 - rr'e^{-2ikL}}. \tag{2.2.6}$$

From the expressions given in Eq. (2.2.5) we can say that a Fabry-Perot cavity behaves basically as a frequency-dependent beam splitter where the reflection and transmission coefficients satisfy the energy conservation relation $|r_{kL}|^2 + |t_{kL}|^2 = 1$. The parameter $k(2L) = 2\pi(2L)/\lambda$ measures the number of oscillations that fit within the cavity. The normal (or resonant) modes of the cavity are characterized by $\lambda_m = 2L/m$, m being a natural number.

In order to better understand the behavior of the cavity let us see some particular

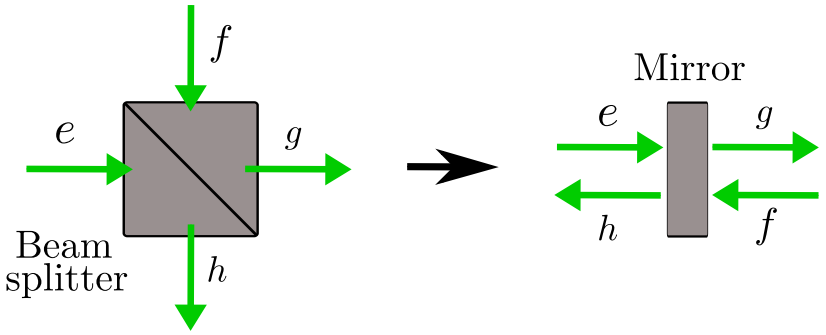

Figure 3: Beam splitter transformation: the output fields g and h are the result of the interference between the input fields e and f.

cases:

- $r = 1$: in this case the incident field does not enter the cavity and is completely reflected by the coupling mirror, as expected.
- $r' = 1$ and $r < 1$: in this case, the incident field is also completely reflected by the cavity but only after it has entered the cavity. For this case $r_{kL} = e^{i\phi_{kL}}$, so the reflected field receives a phase dependent on the frequency in relation to the incident field. This type of cavity is known as a **cavity without losses**, in the sense that the intensity of the reflected and incident fields is equal.
- $r = r'$: in this case, there is a total suppression of the reflected field when the cavity is on resonance. This type of cavity is known as a **cavity with impedance matching**, due to the analogy with electrical circuits, and occurs due to the destructive interference between the field reflected directly by the coupling mirror and the reflected fields from inside the cavity.

There are three important parameters that characterize a Fabry-Perot cavity:

1. The **free spectral range (FSR)** is defined as the frequency difference between two succesive resonant modes and is given by

$$\Delta f = \frac{c}{\lambda_{m+1}} - \frac{c}{\lambda_m} = \frac{c}{2L} = \frac{1}{\tau_{\text{cav}}}, \tag{2.2.7}$$

   where τ_{cav} is the time of flight in one round trip through the cavity.

2. The **finesse** is the parameter that gives us a measure of how narrow are the resonance peaks in relation to the FSR and is given by [Ismail 2016]

$$\mathcal{F} = \frac{\pi}{2}\left[\arcsin\left(\frac{1 - rr'}{2\sqrt{rr'}}\right)\right]^{-1}. \tag{2.2.8}$$

3. The **resonant bandwidth** is defined as the width at half height of a peak of resonance of the cavity and is related to the FSR and finesse as

$$\delta f = \frac{\Delta f}{\mathcal{F}}. \tag{2.2.9}$$

Finally, from the expressions (2.2.7), (2.2.8) and (2.2.9), we can conveniently rewrite the argument that appears in the expressions for r_{kL} and t_{kL} as

$$kL = \frac{2\pi f}{c} L = \frac{\pi}{c/(2L)} f = \pi \frac{f'}{\mathcal{F}}, \tag{2.2.10}$$

where $f' = f/\delta f$ is the frequency in units of bandwidth. Furthermore, because the system is periodic under any frequency shift by an integer multiple of the FSR, then we can substitute f' for the **detuning** in units of bandwidth, $\widetilde{\Delta} = f' - f'_{\text{res}}$, where f'_{res} is the closest resonance frequency. Taking into account the above, the expressions in Eq. (2.2.6) are rewritten as follows

$$r_{\widetilde{\Delta}} = \frac{r - r' e^{-i2\pi\widetilde{\Delta}/\mathcal{F}}}{1 - rr' e^{-i2\pi\widetilde{\Delta}/\mathcal{F}}}, \qquad \text{and} \qquad t_{\widetilde{\Delta}} = \frac{tt' e^{-i\pi\widetilde{\Delta}/\mathcal{F}}}{1 - rr' e^{-i2\pi\widetilde{\Delta}/\mathcal{F}}}. \tag{2.2.11}$$

The squared modulus and phase θ_R of $r_{\widetilde{\Delta}}$ are plotted in Fig. 4 as a function of $\widetilde{\Delta}$. The lorentzian curve $|r_{\widetilde{\Delta}}|^2$ represents an attenuation in the reflected beam relative to the incident one. The phase θ_R varies from 2π to 0 across resonance such that the relative phase between off-resonant and exactly resonant fields is π. The phase of $t_{\widetilde{\Delta}}$ has the same shape, but varies from π to 0 across the resonance, similarly to simple mechanical resonances.

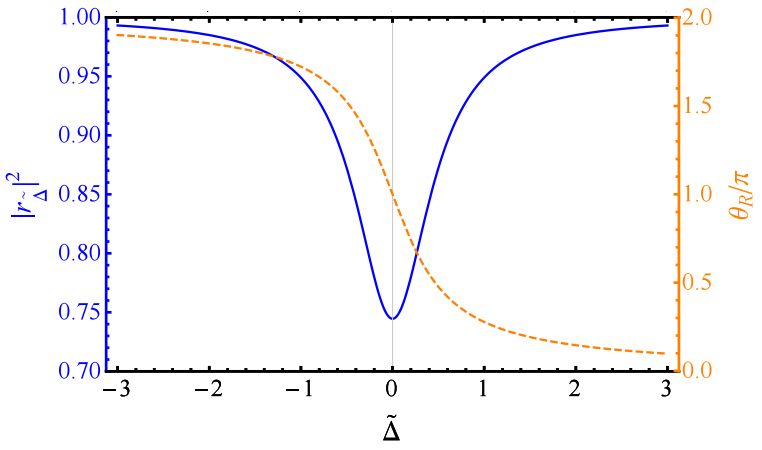

Figure 4: Squared modulus (continuous line) and phase (dashed line) of $r_{\widetilde{\Delta}}$ as functions of the detuning parameter $\widetilde{\Delta}$ relative to the cavity bandwidth. The values used for the reflection coefficients of the mirrors are $R = r^2 = 96.0\%$ and $R' = r'^2 = 99.7\%$.

2.3 Optical parametric oscillator

An OPO is a coherent light source similar to a laser but with an optical gain medium from the parametric conversion. It is basically composed of three elements: an intense light source (pumping laser), a nonlinear material with second-order susceptibility $\chi^{(2)}$ that acts as a gain medium and an optical cavity responsible for feedback of the medium (Figure 5).

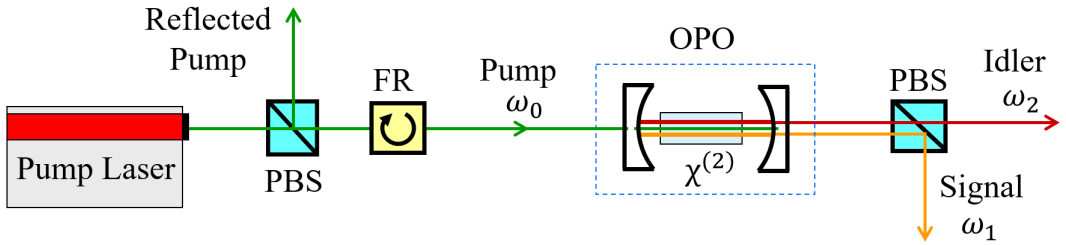

Figure 5: Schematic description of an optical parametric oscillator, consisting of a crystal with nonlinear susceptibility $\chi^{(2)}$ arranged inside a Fabry-Perot cavity. A laser light source supplies the pumping field with frequency ω_0 that interacts with the nonlinear crystal resulting in the creation of two new fields, signal and idler, with frequencies ω_1 and ω_2, respectively. The interaction process also gives rise to a reflected field of frequency equal to the pump beam (reflected pump) that is separated from the incident pump with the use of a Faraday Rotator (FR) and a PBS.

Due to the non-linearity of second order, the crystal absorbs photons from the pump laser (frequency ω_0) with a small probability. Under ideal conditions, for each pumping photon absorbed, the crystal emits two photons of lower frequencies ω_1 and ω_2, respectively. Because they are emitted at the same time, these photons are called ***twin photons*** and the physical process that produces them is known as ***parametric down conversion*** (PDC). In the PDC two conditions are satisfied: energy conservation or ***frequency-matching*** ($\omega_0 = \omega_1 + \omega_2$) and conservation of momentum or ***phase-matching*** ($\vec{k}_0 = \vec{k}_1 + \vec{k}_2$). The most common phase-matching are those of type I, when the twin photons are generated with the same polarization, or of type II, when the polarizations of both photons are orthogonal.

The conversion rate of photons becomes considerably greater when the crystal is placed inside an optical cavity. The crystal happens to act as a gain medium and therefore, in the same way as it happens in a laser, when the parametric gain exceeds the internal losses of the cavity (total losses generated by the transmission of the mirrors, absorption, dispersion and diffraction), it is said that the system oscillates and the OPO emits two new coherent beams, signal and idler. The power of the pumping for which the parametric gain equals the internal losses of the cavity is called **oscillation threshold**. When reaching the oscillation threshold, part of the pumping energy is transferred to the signal and idler beams, decreasing its intensity inside the crystal, which eventually leads to a saturation of the parametric gain. This process allows the OPO to work in a steady state [Debuisschert 1993, Martinelli 2002, Träger 2007, Breunig 2011].

The optical cavity can be resonant for just a subset of the fields involved in the parametric conversion, that is, for one (SRO), two (DRO) or three (TRO) fields. In this thesis we will consider the case of a TRO, that is, a resonant OPO for pump, signal and idler. The main characteristic of this configuration is that it has the lowest oscillation threshold because the parametric gain increases with the intensities of the three fields interacting through the crystal.

From the theoretical point of view, the PDC present in an OPO can be modeled through the effective Hamiltonian of a three-wave mixing process given by [Walls 2008]

$$\hat{H}_\chi = i\hbar\frac{\chi}{\tau}\left[\hat{a}^{(0)}\hat{a}^{(1)\dagger}\hat{a}^{(2)\dagger} - \hat{a}^{(0)\dagger}\hat{a}^{(1)}\hat{a}^{(2)}\right], \tag{2.3.1}$$

where $\hat{a}^{(n)}$ and $\hat{a}^{(n)\dagger}$ are the annihilation and creation operators of the mode $n \in \{0, 1, 2\}$, corresponding to the pump, signal and idler beams, respectively (this notation will be maintained throughout the thesis). Here, τ is the time of flight through the medium, considered the same for the three fields, and χ is a constant proportional to the second-order susceptibility $\chi^{(2)}$[2]. Note that this Hamiltonian describes the creation of a pair of photons with frequencies ω_1 and ω_2 from the annihilation of a photon with frequency ω_0 or the opposite process; creation of ω_0 by the annihilation of ω_1 and ω_2[3].

As we will see in the next subsection, from the Hamiltonian Eq. (2.3.1) one can obtain the main classical properties of a triply resonant OPO operating above the threshold[4]. The quantum properties will be obtained in chapter 3, following the same formalism developed in this section, and is one of the original results of this thesis.

2.3.1 *Classical properties*

From the PDC Hamiltonian given in Eq. (2.3.1), in this section we will obtain the main properties of a triply resonant OPO operating above the oscillation threshold. In the description, it is considered that the intracavity field is formed by the pump, signal and idler beams, which allows us to calculate the average intensity of each of these fields.

Parametric gain of the fields

Let us start by considering the evolution of the fields within the nonlinear crystal, as shown in Fig. 6. Using the PDC Hamiltonian given in Eq. (2.3.1) and the Heisenberg equation, we find the following equations of motion for each of the field operators

[2]The explicit form of χ is not important because it will be associated with the power for the threshold (see section 2.3.1) .

[3]Since the nonlinear susceptibility crystal $\chi^{(2)}$ is placed inside a cavity, the two processes in the Hamiltonian Eq. (2.3.1) can ocurr.

[4]From now on whenever we talk about an OPO we will be referring to this particular case.

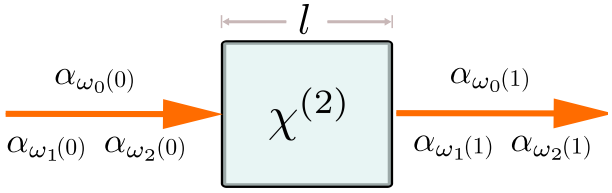

Figure 6: Propagation scheme of the fields within the crystal of nonlinear susceptibility $\chi^{(2)}$ and lenght l.

$$\begin{cases} \frac{d}{d\xi}\hat{a}^{(0)} &= -\chi\hat{a}^{(1)}\hat{a}^{(2)}, \\ \frac{d}{d\xi}\hat{a}^{(1)} &= \chi\hat{a}^{(0)}\hat{a}^{(2)\dagger}, \\ \frac{d}{d\xi}\hat{a}^{(2)} &= \chi\hat{a}^{(0)}a^{(1)\dagger}, \end{cases} \tag{2.3.2}$$

where ξ is the time evolution normalized to the time of flight throught the crystal τ. In what follows, we consider a linearized description of the fields by their mean value and fluctuation, i.e, each mode is described as $\hat{a}^{(n)} = \alpha_{\omega_n} + \delta\hat{a}^{(n)}$, where α_{ω_n} is the mean light field amplitude. In order to determine the evolution of the classical fields we neglect the fluctuations $\delta\hat{a}^{(n)}$ and thus obtain

$$\begin{cases} \frac{d}{d\xi}\alpha_{\omega_0} &= -\chi\alpha_{\omega_1}\alpha_{\omega_2}, \\ \frac{d}{d\xi}\alpha_{\omega_1} &= \chi\alpha_{\omega_0}\alpha^*_{\omega_2}, \\ \frac{d}{d\xi}\alpha_{\omega_2} &= \chi\alpha_{\omega_0}\alpha^*_{\omega_1}. \end{cases} \tag{2.3.3}$$

Because the parametric gain of the crystal is very small, we can expand the expressions of the fields in powers of ξ. Considering only the first order of the expansion, which is sufficient for the description of a typical OPO [Debuisschert 1993], i.e.

$$\alpha_{\omega_n}(\xi) \simeq \alpha_{\omega_n}(0) + \xi\frac{d\alpha_{\omega_n}}{d\xi}(0), \tag{2.3.4}$$

we obtain the variations of the amplitudes of the fields after crossing the nonlinear crystal:

$$\begin{cases} \alpha_{\omega_0}(1) &= \alpha_{\omega_0}(0) - \chi\alpha_{\omega_1}(0)\alpha_{\omega_2}(0), \\ \alpha_{\omega_1}(1) &= \alpha_{\omega_1}(0) + \chi\alpha_{\omega_0}(0)\alpha^*_{\omega_2}(0), \\ \alpha_{\omega_2}(1) &= \alpha_{\omega_n}(0) + \chi\alpha_{\omega_0}(0)\alpha^*_{\omega_1}(0), \end{cases} \tag{2.3.5}$$

From the expressions given in Eq. (2.3.5), which are consistent with those found in the standard classical description [Debuisschert 1993], we can see that the amplitude of the

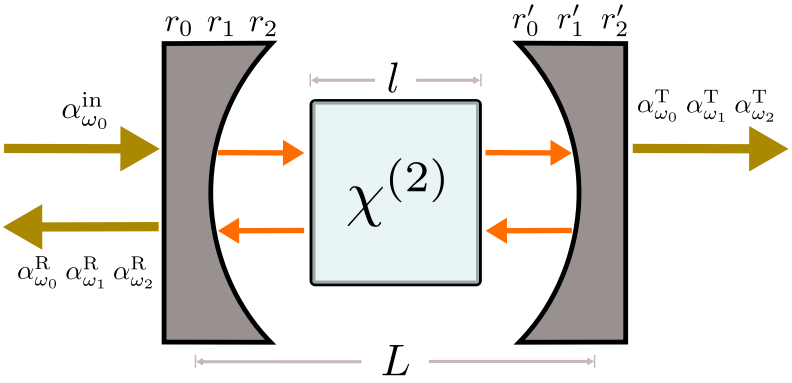

Figure 7: Basic configuration of OPO, consisting of a nonlinear medium of length l inside a Fabry-Perot cavity of length L, made of one coupling mirror (left) and one end mirror (right) accounting for spurious losses. In this theoretical design, the fields measured in the experiment are the fields reflected by the cavity, i.e. $\alpha^{\text{R}}_{\omega_0}$, $\alpha^{\text{R}}_{\omega_1}$ and $\alpha^{\text{R}}_{\omega_2}$. The fields transmitted by the cavity account for all the spurious losses present in the system for each mode, respectively.

pumping field decreases when passing through the crystal and that, on the other hand, the intensity of the twin beams increases, as discussed earlier at the beginning of the section.

Modeling the optical cavity: stationary equations

Once we have found the variation of the amplitudes of the fields when going through the nonlinear crystal, the next step is to find the equations that govern the three fields within the cavity in the stationary regime. Therefore, we are going to consider a Fabry-Perot cavity around the crystal as shown in Fig. 7. It has a coupling mirror (left mirror) with reflection and transmission coefficients r_n and t_n, and an end mirror (right mirror) with reflection coefficient r'_n and transmission coefficient t'_n representing spurious losses (e.g. absortion in the crystal or scattering on the optical interfaces).

For each round trip in the cavity, the fields gain an accumulated phase due to their propagation in free space and within the crystal, which depends on the refractive index $\mathtt{n}_n$ for each mode of the OPO, given by $\varphi_n = 2L^{(n)}_{\text{op}}\omega_n/c$, where $L^{(n)}_{\text{op}} = L + l(\mathtt{n}_n - 1)$ is the ***effective optical lenght*** between the cavity mirrors. We will not consider the phase changes in the mirrors since in principle they will be considered as ideal[5]. In addition, as discussed in the previous section, each field receives a gain introduced by the crystal, as the one described by Eq. (2.3.5). Therefore, we can propose a set of equations similar to those given in the Eqs. (2.2.2), (2.2.3) and (2.2.4), for each field under consideration, and so find the following equations that govern the three intracavity fields $\alpha_{\omega_n} = \alpha_{\omega_n}(0)$ in the steady-state regime for exact phase matching:

[5]In ref. [Debuisschert 1993] it is shown that these phase shifts can increase the oscillation threshold, however, this increase can be compensated by a disagreement in the condition of phase matching. In the worst case, the threshold would increase by a factor of 1.92.

$$\begin{cases} \alpha_{\omega_0} &= e^{-i\varphi_0}\left[\left(\alpha_{\omega_0} - 2\chi\alpha_{\omega_1}\alpha_{\omega_2}\right) r_0 r_0'\right] + t_0\alpha_{\omega_0}^{in}, \\ \alpha_{\omega_1} &= e^{-i\varphi_1}\left[\left(\alpha_{\omega_1} + 2\chi\alpha_{\omega_0}\alpha_{\omega_2}^{*}\right) r_1 r_1'\right], \\ \alpha_{\omega_2} &= e^{-i\varphi_2}\left[\left(\alpha_{\omega_2} + 2\chi\alpha_{\omega_0}\alpha_{\omega_1}^{*}\right) r_2 r_2'\right]. \end{cases} \tag{2.3.6}$$

The coefficients r_n and r_n' can be conveniently described by loss parameters γ_n and γ_n' as

$$r_n = e^{-\gamma_n}, \qquad t_n = \left(1 - r_n^2\right)^{1/2}, \tag{2.3.7}$$

$$r_n' = e^{-\gamma_n'}, \qquad t_n' = \left(1 - r_n'^2\right)^{1/2}. \tag{2.3.8}$$

The total loss in a round trip can be directly evaluated from $\gamma_n^t = \gamma_n + \gamma_n'$. The loss parameter γ_n' will be called spurious losses or intracavity losses since, it can model any coupling of the cavity with the outside that does not occur by means of the coupling mirror. Using Eqs. (2.3.7) and (2.3.8) and considering that the three fields are resonant with the cavity ($e^{-i\varphi_n} = 1$), the expressions in Eq. (2.3.6) are rewritten in the following way:

$$\begin{cases} \alpha_{\omega_0}[1 - e^{-\gamma_0^t}] &= -2\chi\alpha_{\omega_1}\alpha_{\omega_2}e^{-\gamma_0^t} + \sqrt{1 - e^{-2\gamma_0}}\,\alpha_{\omega_0}^{in}, \\ \alpha_{\omega_1}[1 - e^{-\gamma_1^t}] &= 2\chi\alpha_{\omega_0}\alpha_{\omega_2}^{*}e^{-\gamma_1^t}, \\ \alpha_{\omega_2}[1 - e^{-\gamma_2^t}] &= 2\chi\alpha_{\omega_0}\alpha_{\omega_1}^{*}e^{-\gamma_2^t}, \end{cases} \tag{2.3.9}$$

The solution of the system of equations (2.3.9) gives us the different operating regimes of the OPO. From that we obtain the response of the OPO output for different input powers.

Stationary solutions

The last two of Eqs. (2.3.9) form a homogeneous system for signal and idler and their conjugates. This system of equations admits a non-trivial solution if its determinant is null. With this imposed condition we have

$$|\,\alpha_{\omega_0}\,|^2 = \frac{\left(e^{\gamma_1^t} - 1\right)\left(e^{\gamma_2^t} - 1\right)}{4\chi^2}, \qquad \text{and} \qquad \frac{|\,\alpha_{\omega_1}\,|^2}{|\,\alpha_{\omega_2}\,|^2} = \frac{\left(e^{\gamma_2^t} - 1\right)}{\left(e^{\gamma_1^t} - 1\right)}. \tag{2.3.10}$$

From the first expression given in Eq. (2.3.10), we can see that the intracavity pump power does not depend on the incident pump power (above the oscillation threshold)

but only on the losses and the coupling constant χ. Imposing $|\alpha_{\omega_1}| = |\alpha_{\omega_2}| = 0$ in the first expression of Eq.(2.3.9), we can get the power of the minimum pumping so that the intense beams of signal and idler are generated

$$| \alpha^{\text{in}}_{\omega_0} |^2_{\text{th}} = \frac{\left(1 - e^{-\gamma_0^t}\right)^2 \left(e^{\gamma_1^t} - 1\right) \left(e^{\gamma_2^t} - 1\right)}{4\chi^2 \left(1 - e^{-2\gamma_0}\right)}. \tag{2.3.11}$$

From this power up of the input field, the intracavity pump power is kept constant at the value shown in Eq. (2.3.10) and the excess power is transferred to the twin beams.

From the Eqs. (2.3.9), (2.3.10) and (2.3.11) we get the following expressions for intracavity powers of all the fields under consideration

$$| \alpha_{\omega_0} |^2 = \frac{\left(1 - e^{-2\gamma_0}\right)}{\left(1 - e^{-\gamma_0^t}\right)^2} | \alpha^{\text{in}}_{\omega_0} |^2_{\text{th},} \tag{2.3.12}$$

$$| \alpha_{\omega_j} |^2 = \frac{e^{2\gamma_0^t} \left(1 - e^{-2\gamma_0}\right) \left(\sqrt{\sigma} - 1\right)}{\left(e^{\gamma_0^t} - 1\right) \left(e^{\gamma_j^t} - 1\right)} | \alpha^{\text{in}}_{\omega_0} |^2_{\text{th}} \quad \text{with} \quad j = 1, 2, \tag{2.3.13}$$

where the pump power relative to the oscillation threshold, $\sigma = \left|\alpha^{\text{in}}_{\omega_0}\right|^2 / \left|\alpha^{\text{in}}_{\omega_0}\right|^2_{\text{th}}$, has been defined. Furthermore, the following expression is also found for the phases of the fields ($\alpha = |\alpha| \, e^{\phi}$)

$$\phi_0 = \phi_1 + \phi_2. \tag{2.3.14}$$

Note that the sum of the phases of the twin beams is perfectly correlated with the pump phase but the phase difference can fluctuate freely since the system is invariant under the transformation $\alpha_{\omega_1} \rightarrow \alpha_{\omega_1} e^{\phi}$, $\alpha_{\omega_2} \rightarrow \alpha_{\omega_2} e^{-\phi}$. In other words, each of the phases can vary as the three fields propagate through the cavity, however, due to the phase-matching condition, the relationship given in Eq. (2.3.14) remains valid throughout the evolution.

2.4 Photodetection in the spectral domain

As we will see in the chapter 3, complete reconstruction of the quantum state of an OPO operating above the threshold is achieved by performing a photodetection process in the spectral domain, with the help of Fabry-Perot cavities, of each of the light beams generated by this system (see Fig. 19). In order to have a better understanding of this measurement technique, in this section we will describe very briefly its main characteristics following the description done in [Barbosa 2013c].

Usual photodetectors, in continuous variables domain, only detect the intensity of light beams via photoelectric effect, in which excitations of the electromagnetic field, i. e. the photons, become electrons expelled from a material (usually a semiconductor). In this

way, photodetectors generate a time-dependent photocurrent $I(t)$ that gives information about the intensity of the incident light beams. In the high intensity regime ($\sim 10^{16}$ photons per second), it is a continuous signal deprived of quantum jumps associated with individual quanta of light. As the measurement process is given by the photoelectric effect, it is natural that the corresponding measurement operator is directly related to the photon number operator $\hat{a}^\dagger_\omega \hat{a}_\omega$, where $\hat{a}_\omega$ and $\hat{a}^\dagger_\omega$ are the photon annihilation and creation operators in the mode with optical frequency ω, respectively, satisfying $[\hat{a}_\omega, \hat{a}^\dagger_{\omega'}] = \delta(\omega - \omega')$. In fact, in the case of unit quantum efficiency, photodetectors measure directly the quantum observable $\hat{I}(t)$ given by [Glauber 1963]

$$\hat{I}(t) = \hat{E}^-(t)\hat{E}^+(t), \tag{2.4.1}$$

where $\hat{E}^\pm(t)$ are the positive and negative frequency parts of the electric field operator, $\hat{E}(t) = \hat{E}^+(t) + \hat{E}^-(t)$, written in the case of a narrowband light source, and within a multiplicative factor, as

$$\hat{E}^+(t) = \int_0^\infty d\omega\, e^{-i\omega t}\, \hat{a}_\omega\ , \quad \hat{E}^-(t) = \left[\hat{E}^+(t)\right]^\dagger. \tag{2.4.2}$$

where the integration limits enclose a frequency interval compatible with the photodetector bandwidth around the optical frequency ω_0 of a bright auxiliary field, the Local Oscillator (LO). The LO field must posses a well-defined phase relation with respect to the quantum state $|\Psi\rangle$ of remaining modes, i.e. modes in the frequency vicinity of the LO, and is hence effectively described as a coherent state $|\alpha_{\omega_0}\rangle$, where $\alpha_{\omega_0} = |\alpha| \exp(i\varphi)$ denotes its amplitude and phase.

With this general experimental arrangement, the field quantum state just prior to detection is $|\alpha_{\omega_0}\rangle|\Psi\rangle$. Therefore, the quantum state average of Eq. (2.4.1), together with Eq. (2.4.2), yields the photocurrent

$$I(t) \propto |\alpha|^2 + |\alpha| \langle\Psi| \left[e^{-i\varphi}\hat{a}(t) + e^{i\varphi}\hat{a}^\dagger(t)\right] |\Psi\rangle, \tag{2.4.3}$$

where small contributions have been disregarded. In this expression, the new annihilation $\hat{a}(t)$ and creation $\hat{a}^\dagger(t)$ operators are defined as

$$\hat{a}(t) = \int_0^{\prime\infty} d\omega\, e^{-i(\omega-\omega_0)t}\, \hat{a}_\omega, \quad \hat{a}^\dagger(t) = [\hat{a}(t)]^\dagger, \tag{2.4.4}$$

where the integral in ω excludes the mode ω_0 (a fact denoted by the prime).

In Eq. (2.4.3), the term $|\alpha|^2$ is the mean photocurrent while the state-dependent term represents quantum fluctuations of the photocurrent, whose corresponding measurement operator is given by $\delta\hat{I}(t) = e^{-i\varphi}\hat{a}(t) + e^{i\varphi}\hat{a}^\dagger(t)$. Note that the response time of a realistic photodetector will necessarily impose the temporal integration of Eq. (2.4.3), defining the

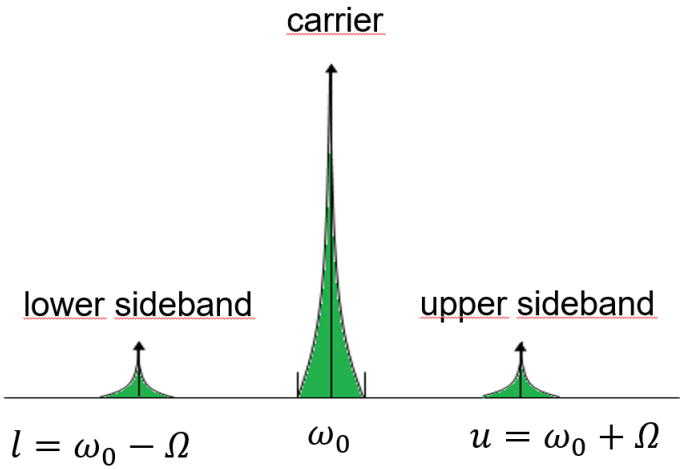

Figure 8: Sideband modes, at a Fourier frequency Ω, and the central mode with frequency ω_0 (carrier) of a narrowband coherent light beam.

spectral shape of measured mode $\hat{a}(t)$ in Eq. (2.4.4) [Yurke 1985b].

The photocurrent fluctuation given by Eq. (2.4.3) can be described in frequency domain by Fourier transform as

$$\hat{I}_\Omega = \int \delta\hat{I}(t)\, \mathrm{e}^{i\Omega t} d\Omega, \tag{2.4.5}$$

where the effective integration limits are determined by detection bandwidth. It is easy to show that the spectral component of the photocurrent is a complex quantity associated with the non-Hermitian operator

$$\hat{I}_\Omega = \mathrm{e}^{-i\varphi}\hat{a}_u + \mathrm{e}^{i\varphi}\hat{a}_\ell^\dagger, \tag{2.4.6}$$

where $\hat{a}_u$ and $\hat{a}_\ell$ are the annihilation operators of the upper and lower sideband modes at frequencies $\omega_0 + \Omega$ and $\omega_0 - \Omega$, respectively (see Fig. 8). Therefore, for each Fourier frequency Ω, spectral analysis implies *necessarily a two-mode detection scheme.*

The non-Hermitian operator $\hat{I}_\Omega$ can be written in terms of quantum-mechanical observables $\hat{I}_{\cos}$ and $\hat{I}_{\sin}$ representing the photocurrent electronic quadratures as $\hat{I}_\Omega = (\hat{I}_{\cos} + i\hat{I}_{\sin})/\sqrt{2}$, with

$$\begin{cases} \hat{I}_{\cos} &= \cos\varphi\, \dfrac{\hat{p}_u + \hat{p}_\ell}{\sqrt{2}} + \sin\varphi\, \dfrac{\hat{q}_u + \hat{q}_\ell}{\sqrt{2}}, \\ \hat{I}_{\sin} &= \cos\varphi\, \dfrac{\hat{q}_u - \hat{q}_\ell}{\sqrt{2}} - \sin\varphi\, \dfrac{\hat{p}_u - \hat{p}_\ell}{\sqrt{2}}, \end{cases} \tag{2.4.7}$$

where $\hat{p}_\omega$ and $\hat{q}_\omega$ are the amplitude and phase quadrature observables representing a single longitudinal mode with optical frequency ω, respectively. In terms of the photon annihilation $\hat{a}_\omega$ and creation $\hat{a}_\omega^\dagger$ operators, they relate as $\hat{a}_\omega = (\hat{p}_\omega + i\hat{q}_\omega)/2$.

The measurement operators in Eq. (2.4.7) are associated with field modes that are symmetric and antisymmetric combinations of sideband modes. A direct measurement of

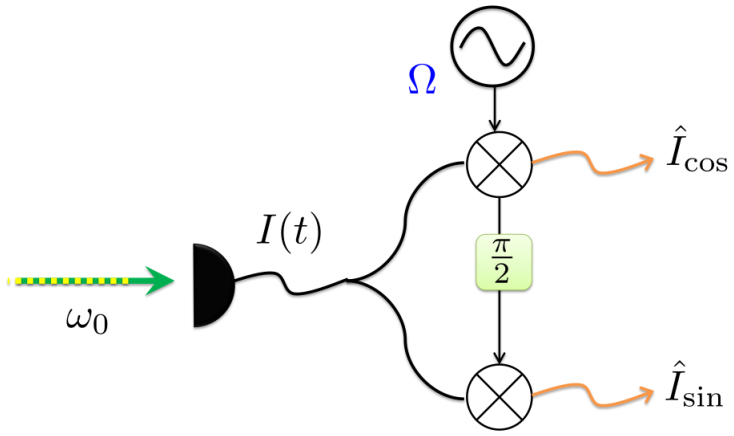

Figure 9: Scheme to measure electronic quadrature components of each photocurrent signal. The photocurrent is mixed with two electronic references in quadrature. Figure adapted from [Barbosa 2013c].

both photocurrent Fourier quadrature components, if possible, would provide direct information about the *optical* quadrature components of these specific modes [Heidmann 1984]. In the ideal case, each measurement of an *electronic* quadrature component thus represents a *single-mode* measurement, free of assumptions. A possible technique to perform this measurement is shown in Fig. 9, by mixing the photocurrent with two electronic references in quadrature [Yuen 1980]. In typical experiments using this technique, the Fourier frequency Ω is in the MHz range [Yurke 1985a, Barbosa 2013c].

Note that only with the use of the technique shown schematically in Fig. 9, it is not possible to access all the information on the optical quadrature components of the field because it does not allow us to control the parameter φ [see Eq. (2.4.7)]. This problem can be solved, however, if this technique is combined with some interferometric detection technique [Barbosa 2013c].

Homodyne Detection (HD) was the first interferometric technique to provide direct access to quadrature field observables and still remains the most widely used measurement technique in the continuous variables domain [Yuen 1978, Shapiro 1979]. Balanced HD is the usual realization of HD in the laboratory [Yuen 1983, Schumaker 1984, Shapiro 1985] and in the present discussion it is implemented as follows (see left panel in Fig. 10): the field modes to characterize are mixed on a 50:50 beam splitter with the LO. Quantum measurement is obtained by the difference between photocurrents recorded on a pair of photodetectors placed on the two outputs of the beam splitter. At this point the spectral analysis of the photocurrent quantum fluctuations is performed, making use of the technique outlined in Fig. 9. The whole process is known as spectral HD. In this case, the spectral HD is essentially described by the ideas presented above, and the measurement operators of Eq. (2.4.7) can be directly applied. It is important to clarify that in order to implement the spectral HD it is necessary to have a reference beam (the LO) with the same frequency as the beam we want to measure (see left panel in Fig. 10). This is the main drawback of being able to apply this technique to reconstruct the quantum state of

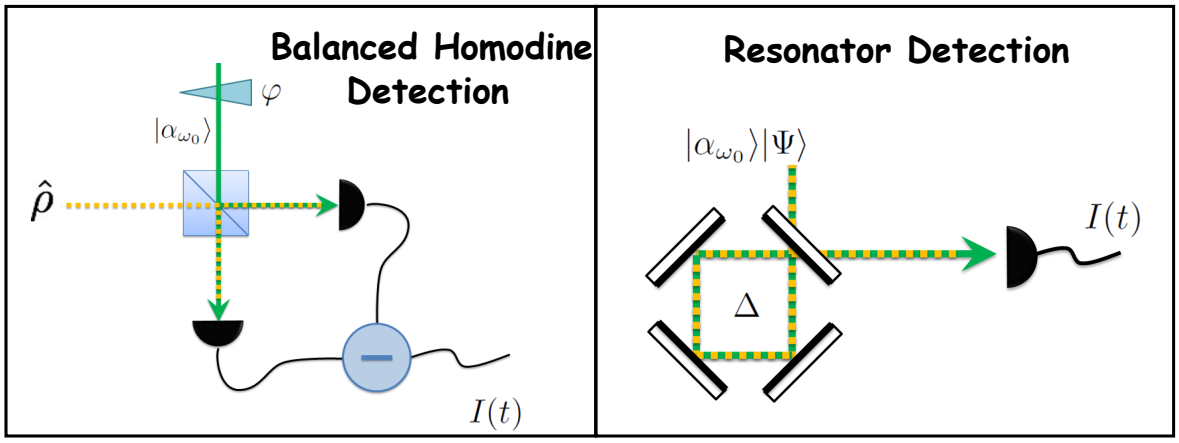

Figure 10: Interferometric techniques. Left panel: Schematic view of the balanced HD. Prior to detecttion, LO field in state $|\alpha_{\omega_0}\rangle$ is added to the quantum field modes of interest with a controlled phase φ, using a 50:50 beam splitter. Information about the quantum field is retrieved after subtraction of the photocurrents. Right panel: Schematic view of RD. The state of interest and the carrier mode are reflected off an optical resonator prior to photodetection. Frequency-dependent losses and phase schifts, controlled by resonator detuning Δ, allow quantum state reconstruction. Figures adapted from [Barbosa 2013c].

an OPO since it is very difficult to have a reference beam for each of the beams produced by this system. Even, if somehow it were possible to implement it in this system, the equation (2.4.7) shows that, although spectral HD is, in principle, able to provide two-mode operator moments, it cannot achieve complete quantum state reconstruction. The reason for that is the fact that symmetric and antisymmetric combinations of sideband modes cannot be probed independently, since their measurement orientations in phase space are fixed with respect to one another by a single parameter φ [Barbosa 2013b].

An alternative technique to spectral HD does not suffer from the same limitations, it is known as Resonator Detection (RD). This technique is based on the dispersive property of an optical resonator close to resonance, bringing an intrinsic asymmetry in the way sideband modes are manipulated before photodetection. RD is realized by measuring the intensity fluctuation of a field after its reflection from an optical resonator, as schematized in the right panel in Fig. 10. Field modes in a narrow band close to resonance with the optical cavity are phase shifted and attenuated just prior to detection. Similarly to HD, RD needs an intense LO field to amplify the quantum fluctuations of the sideband modes in the detection.

An optical resonator with high finesse transforms the field annihilation operators according to

$$\hat{a}_\omega \longrightarrow r(\Delta_\omega)\,\hat{a}_\omega + t(\Delta_\omega)\,\hat{b}_\omega, \tag{2.4.8}$$

where $r(\Delta_\omega)$ and $t(\Delta_\omega) = \sqrt{1 - r^2(\Delta_\omega)}$ are the resonator reflection and transmission frequency responses, respectively. A vacuum mode, described by the annihilation operator $\hat{b}_\omega$, substitutes the missing fraction of reflected modes, a feature which proves essential to the power of the technique regarding quantum state reconstruction [Barbosa 2013c].

Substituting Eq. (2.4.8) in Eq. (2.4.6), the spectral operator of RD reads as

$$\hat{J}_{\Omega}(\Delta) \;=\; R^{*}_{\Omega}(\Delta)\,\hat{a}_u + R_{-\Omega}(\Delta)\,\hat{a}^{\dagger}_{\ell} + T^{*}_{\Omega}(\Delta)\,\hat{b}_u + T_{-\Omega}(\Delta)\,\hat{b}^{\dagger}_{\ell}, \tag{2.4.9}$$

with

$$R_{\Omega}(\Delta) = \frac{1}{\sqrt{2}}\frac{r(\Delta)}{|r(\Delta)|}\,r^{*}(\Delta+\Omega/\gamma), \qquad \text{and} \qquad T_{\Omega}(\Delta)=\frac{1}{\sqrt{2}}\frac{r(\Delta)}{|r(\Delta)|}\,t^{*}(\Delta+\Omega/\gamma),$$

where $\Delta = (\omega_0 - \omega_c)/\gamma$ is the detuning between carrier ω_0 and resonator frequency ω_c (γ is the resonator bandwidth). Note that the coefficients $R_{\Omega}(\Delta)$ and $R^{*}_{-\Omega}(\Delta)$ do not treat LO sidebands in a symmetric manner as the control parameter Δ is varied. This fact alone allows for the full reconstruction of the quantum state of both sidebands, including coherences therein. In fact, the operator in Eq. (2.4.9) can be written in terms of two Hermitian measurement operators for the electronic quadrature components of the photocurrents $\hat{J}_{\cos}$ and $\hat{J}_{\sin}$, together with vacuum terms due to depletion that the sidebands undergo when on resonance ($\hat{J}_{vac}$), by the expression $\hat{J}_{\Omega} = \left(\hat{J}_{\cos} + i\hat{J}_{\sin}\right)/\sqrt{2} + \hat{J}_{vac}$. The Hermitian measurement operators $\hat{J}_{\cos}$ and $\hat{J}_{\sin}$ are given by

$$\begin{cases} \hat{J}_{\cos}(\Delta) &=& x_{+}\hat{p}_u + y_{+}\hat{q}_u + x_{-}\hat{p}_{\ell} - y_{-}\hat{q}_{\ell} \\ \hat{J}_{\sin}(\Delta) &=& y_{-}\hat{p}_u + x_{-}\hat{q}_u - y_{+}\hat{p}_{\ell} + x_{+}\hat{q}_{\ell} \end{cases}, \tag{2.4.10}$$

where $x_{\pm}$ and $y_{\pm}$ are real functions of Δ defined as

$$\begin{aligned} x_{+} + iy_{+} &= (R_{\Omega} + R^{*}_{-\Omega})/2, \\ x_{-} + iy_{-} &= i(R_{\Omega} - R^{*}_{-\Omega})/2. \end{aligned} \tag{2.4.11}$$

The fact that different coefficients appear for each quadrature operators in Eq. (2.4.10) allows one to single out any sideband or combinations of them. Contrarily to HD, the electronic quadrature measurement operators of RD undergo changes of modal basis depending on Δ, revealing the inherent two-mode character of the technique. Thus, a truly two-mode full state characterization is, in principle, possible using this technique. In fact, it was the technique used to reconstruct the quantum state of the triply resonant OPO studied in the chapter 3.

2.5 Magneto-optical trap

The Magneto-Optical Trap (MOT) is the most common technique used to trap neutral atoms since 1987, when it was introduced [Raab 1987]. The Reason for this is the relative

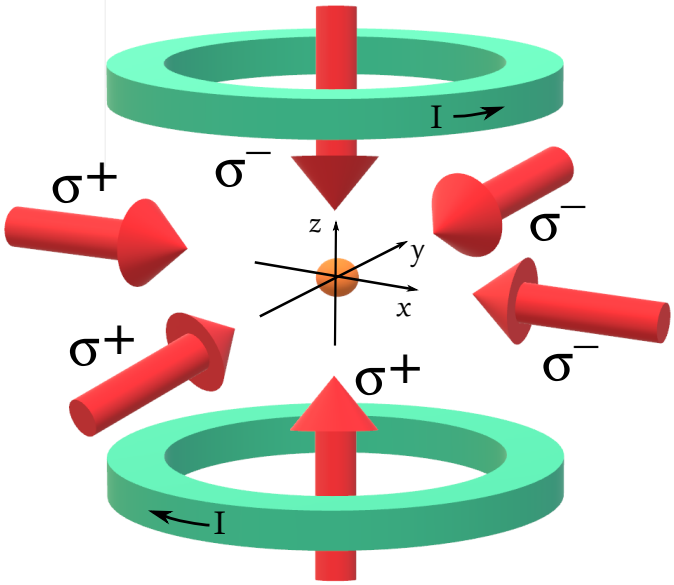

Figure 11: The configuration of the laser beams in a three-dimensional MOT with two coils to produce a quadrupole magnetic field. The orange ball in the middle represents the atomic cloud.

simplicity of the experimental setup for trapping and cooling the atomic gas from room temperature down to the order of micro kelvins.

The basic configuration of a MOT consists of three pairs of counter-propagating red-detuned laser beams arranged, in three perpendicular directions, and a pair of coils in anti-Helmholtz configuration, as shown in Fig. 11. The polarization of each pair of beams is chosen to have mutually orthogonal polarization. In our setup, the polarizations are σ^+ and σ^- which induce transitions into Zeeman sub-levels with the change $\Delta m_F = 1$ and $\Delta m_F = -1$, respectively. Without the magnetic field, these beams only create friction forces since they will come into resonance with atoms that are moving in the opposite direction of the wave's propagation and thus decelerate those atoms. Therefore, this configuration with no magnetic field is known as an ***optical molasses***. This cooling process is called ***Doppler cooling*** due to the use of the Doppler effect in decelerating the atoms [Foot 2005].

Optical molasses alone provides cooling without trapping since it leads only to a velocity dependent force. Therefore, to implement the trapping, it is required to apply a position dependent force in order to confine the atoms. In a MOT, a quadrupole magnetic field is applied to produce such force. This can be implemented by using two magnetic coils with opposite current directions to produce a quadrupole magnetic field which causes an imbalance in the scattering force applied by the laser beams.

In order to better understand the MOT principle, let us consider the one-dimensional scheme in Fig. 12 for a simple atomic transition $F = 0 \rightarrow F' = 1$ (in the same way as it is considered in [Foot 2005]). At the point in the middle of the coils, the magnetic fields produced by the coils cancels out, so that $B = 0$. Close to this zero of the field there

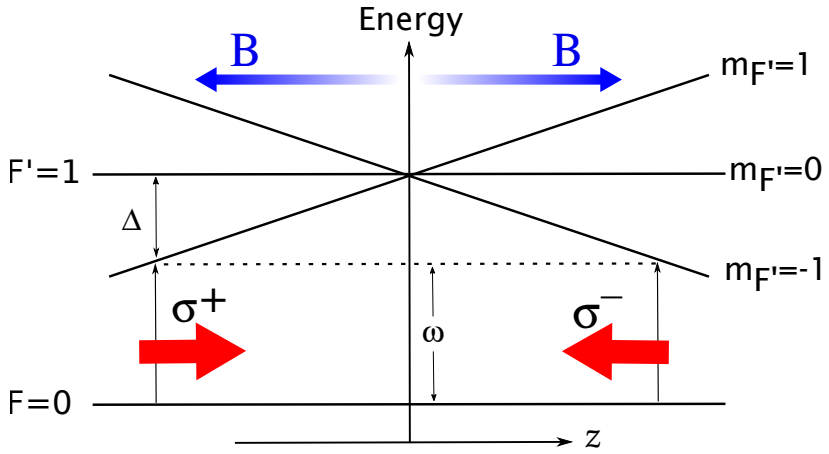

Figure 12: A conceptual scheme for a general one-dimensional MOT. Energy of the Zeeman sub-levels as a function of the position in a one-dimensional MOT for the atomic transition $F = 0 \rightarrow F' = 1$. Two counter-propagating beams of circularly-polarized light with frequency ω(red-detuned by Δ with respect to the atomic transition) interact with the atoms coupling the σ^-component with the $m_{F'} = -1$ sub-level and the σ^+ component with the $m_{F'} = 1$ sub-level according to the selection rules.

is an uniform field gradient that disturbs the atomic excited level[6]; the Zeeman effect causes the energy of two sub-levels (with $m'_F = \pm 1$) of the $F' = 1$ level to vary linearly with the atom's position, as shown for the z-axis in Fig. 12. The atoms are illuminated by counter-propagating laser beams with opposite circular polarizations (σ^+ and σ^-) and a frequency slightly smaller than the atomic resonance frequency (red-detuned) to give damping by the optical molasses mechanism. The Zeeman shift causes an imbalance in the radiation force in the following way: if an atom is displaced from the trap center along the z-axis with $z > 0$, the Zeeman shift moves the sublevel $m'_F = -1$ closer to resonance with the laser frequency. The selection rules lead to absorption of photons from the beam that excites the $\Delta m'_F$ transition and this gives a scattering force that pushes the atom back towards the trap center. A similar process occurs when the atom is displaced towards the opposite direction ($z < 0$). Therefore, the atom will always be pushed back towards $z = 0$, and a cold atomic cloud is formed at the trap center. In the limit of small Zeeman shifts and small velocities the expression for the force on an atom inside a MOT can be written as [Foot 2005]

$$F_{\mathrm{MOT}} = -\alpha \cdot v - \kappa \cdot z, \tag{2.5.1}$$

where α is the damping coefficient as a result of the damping force exerced on the atom by the laser radiation and κ is the spring constant for the restoring force induced by the magnetic field.

In the same way as in the one-dimensional case, the 3D-MOT provides a combination of a velocity dependent force, which damps the atomic motion, and a position depending force, which pushes atoms back to the trap center. This combination of strong damping

[6]This perturbation does not occur for the ground state because its angular momentum is zero.

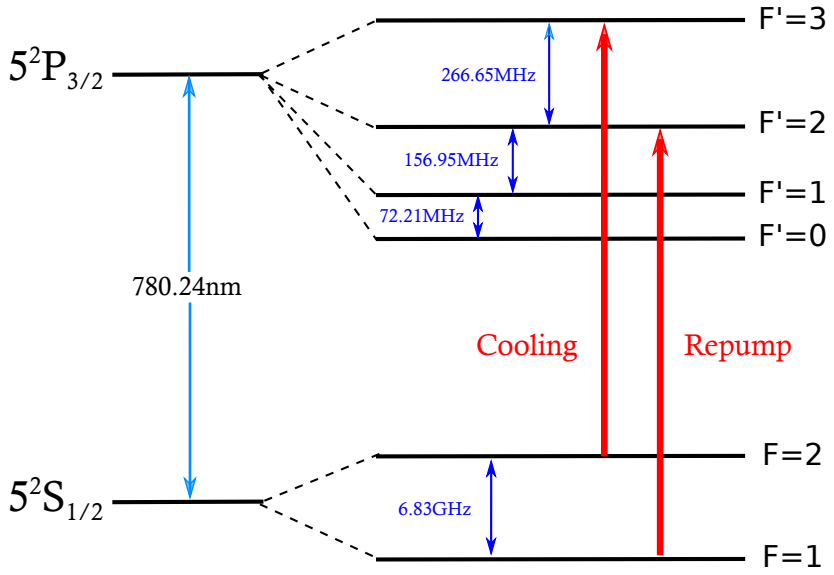

Figure 13: Energy levels for the hyperfine structure of the ^{87}Rb D_2 line. The cooling and repump transitions are indicated by red arrows.

and trapping loads the MOT in a versatile and robust way.

As we will see later in chapter 4, in our experiment we are interested in the D2 transition of Rubidium 87, which has two ground-state hyperfine levels $F = 1$ and $F = 2$ (see Fig. 13). The atoms can decay into any of the F levels with the probabilities dictated by the Clebsch-Gordan coefficients. The trapping transition is chosen to be $F = 2 \rightarrow F' = 3$ with the majority of the atoms decaying back to their original $F = 2$ state, since it is a cyclic transition. This allows the atoms to be addressed by the trapping beams for many consecutive cycles. However, a small portion of the atoms will decay into the dark state $F = 1$ which is not coupled by the cooling laser beam. These atoms do not experience trapping forces and will eventually escape. Therefore, another laser, called the repumping laser is required to excite the atoms from the $F = 1$ level to the $F' = 2$ level from which it can decay back to the $F = 2$ level where it can be excited again by the cooling laser. Using this technique we managed to create a cloud of cold atoms in our experiment using an MOT.

2.6 Photon-pairs generation from a cold atomic ensemble

In this section, we begin by describing the scheme of entangled photon pair generation from a cold atomic ensemble that is considered in this thesis (see chapter 4). The scheme is based on the Duan-Lukin-Cirac-Zoller (DLCZ) protocol, which is one of the most successful experimental implementations of a quantum memory, proposed by Duan et al. in his seminal work published in 2001 [Duan 2001].The operation of this scheme consists of two parts (see subsection 2.6.1): the writing process that is very inefficient and performed with a very low probability and, second, the reading process that is performed with high efficiency and higher probability. This last part of the process is connected with the phe-

nomenon of *superradiance,* which explains, among other things, the high efficiency of the reading process. This phenomenon will be studied in more detail in subsections 2.6.2 and 2.6.3 in the regimes of one and two photons.

2.6.1 *Photon-pairs from the DLCZ-protocol*

The DLCZ protocol uses atomic ensembles that can emit single photons while creating simultaneously single atomic excitations, which are stored in the ensemble. The photons can be used to entangle two distant ensembles [Chou 2005, Laurat 2007]. The atomic excitation can be efficiently converted into a photon thanks to collective interference, which is used for entanglement swapping and various applications of entanglement [Duan 2001, Mendes 2011]. Here we briefly describe the underlying physics following the description done in [Sangouard 2011].

The basic (idealized) scheme is as follows (see Fig. 14). In an ensemble of three-level systems with two ground states ($|g\rangle$ and $|s\rangle$) and an excited state $|e\rangle$, all N atoms are initially in the state $|g\rangle$. Therefore, the atomic state of the system can be written as

$$|0_a\rangle \equiv |g\rangle^{\otimes N} . \tag{2.6.1}$$

An off-resonant laser pulse on the $|g\rangle \rightarrow |e\rangle$ transition (the *write* pulse) may lead to the emission of a photon in field 1 on the $|e\rangle \rightarrow |s\rangle$ transition, via spontaneous Raman emission, and consequently in the transfer of a single atom to state $|s\rangle$ (see write process in Fig. 14). Therefore, the detection of a single photon in field 1, such that no information is revealed about which atom it cames from, creates an atomic state that is a *coherent* superposition of all the possible terms with $N-1$ atoms in $|g\rangle$ and one atom in $|s\rangle$, namely,

$$|1_a\rangle = \frac{1}{\sqrt{N}} \sum_{i=0}^{N} |g_1\rangle \dots |s_i\rangle \dots |g_N\rangle , \tag{2.6.2}$$

which is known in literature as a W-state [Werner 1989].

An important feature of such collective excitations that is of great interest for practical applications is that they can be *read out* very efficiently by converting them into single photons that propagate in a well-defined direction, thanks to collective interference [Duan 2001, Laurat 2006, Simon 2007b, Mendes 2013b]. Resonant laser excitation of such a state on the $|s\rangle \rightarrow |e\rangle$ transition (the *read* laser pulse) leads to an analogous state with $N-1$ atoms in $|g\rangle$ and one delocalized excitation in $|e\rangle$. All the terms in this state can decay to the initial state $|0_a\rangle$, with a probability that grows with the number of atoms squared [Felinto 2005], while emitting a photon in field 2 on the $|e\rangle \rightarrow |g\rangle$ transition (see read process in Fig. 14) [7].

[7] The extraction of the atomic excitation in a photonic mode during the reading process becomes highly

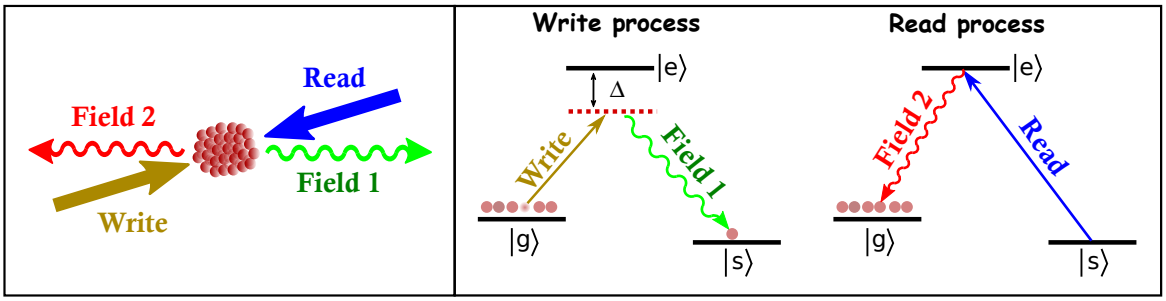

Figure 14: Basic DLCZ scheme for photon-pair generation from a cold atomic ensemble. Write process: All atoms start out in $|g\rangle$. A laser pulse off-resonantly excites the $|g\rangle \rightarrow |e\rangle$ transition, making it possible for a photon (in field 1) to be emitted with small probability on the $|e\rangle \rightarrow |s\rangle$ transition (via spontaneous Raman emission) in addition to storage of a collective atomic excitation. Read process: After a programable time, a resonant laser is applied on the $|s\rangle \rightarrow |e\rangle$ transition, promoting the single atomic excitation from $|s\rangle$ to $|e\rangle$, followed by collective emission on the $|e\rangle \rightarrow |g\rangle$ transition of a photon in field 2 with a well-defined direction.

We have focused on the emission of a single photon into the mode of interest (field 1). However, since there is an ensemble of atoms, there are probability amplitudes for the emission of two or more photons in field 1, accompanied by the creation of the same number of atomic excitations in $|s\rangle$. This dynamics can be described by the following Hamiltonian:

$$\hat{H} = \zeta \left(\hat{a}_1^\dagger \hat{a}_a^\dagger + \hat{a}_1 \hat{a}_a \right), \tag{2.6.3}$$

where ζ is a coupling constant that depends on the intensity and detuning of the laser, number of atoms, and the strengths of the transitions $|g\rangle \rightarrow |e\rangle$ and $|e\rangle \rightarrow |s\rangle$; $\hat{a}_1^\dagger$ is the creation operator for a photon in field 1 and $\hat{a}_a^\dagger$ is the creation operator of an atomic excitation in $|s\rangle$. The vacuum state $|0\rangle$ for the mode $\hat{a}_a$ corresponds to the atomic state with all atoms in $|g\rangle$, the state $\hat{a}_a^\dagger |0\rangle$ with one excitation in $\hat{a}_a$ corresponds to a state as in Eq. (2.6.2) with one atom in $|s\rangle$, etc. This Hamiltonian, whose derivation is discussed in much more detail in [Hammerer 2010], thus describes the creation (and annihilation) of pairs of bosonic excitations[8]. Using operator ordering techniques developed in [Collett 1988], one can show that the application of this Hamiltonian in a two-mode vacuum state creates the following two-mode entangled state (for ζ very small) [Ortiz-Gutiérrez 2017]:

$$\begin{aligned} |\psi_{a,1}\rangle &= \sqrt{1-p}\left[|0_a\rangle |0_1\rangle + e^{i\beta}\sqrt{p}\,|1_a\rangle |1_1\rangle + e^{2i\beta} p\,|2_a\rangle |2_1\rangle + \mathcal{O}\left(p^{3/2}\right)\right], \\ &= \sqrt{1-p}\sum_{n=0}^{\infty} e^{in\beta} p^{n/2}\,|n_a, n_1\rangle\,, \end{aligned} \tag{2.6.4}$$

efficient and directional when the phase matching condition $\vec{k}_w + \vec{k}_r = \vec{k}_1 + \vec{k}_2$ is fulfilled, where $\vec{k}_w$ and $\vec{k}_r$ are the wave vectors for the write and read lasers and $\vec{k}_1$ and $\vec{k}_2$ are the wave vectors for fields 1 and 2, respectively.

[8]Note that this Hamiltonian is formally equivalent to the Hamiltonian for the nonlinear optical process of parametric down-conversion [Burnham 1970, Hong 1985, Wu 1986b, Hong 1987].

where $p = \zeta t$, t is the interaction time, and β is a phase determined by the propagation of the write field. Here we use the basis of the excitation number in the description of the state, so that $|n_1\rangle$ corresponds to the state of field 1 with n photons, associated to the atomic state $|n_a\rangle$ which has n atoms transferred to $|s\rangle$. The excitation probability of a single atom transferred from $|g\rangle$ to $|s\rangle$ is p, and the probabilities to transfer two or more atoms of $|g\rangle$ to $|s\rangle$, associated with the presence of two or more photons in field 1, shall be equal to or less than p^2, as can be seen in the equation.

As discussed above, a reading laser resonant with the transition $|s\rangle \rightarrow |e\rangle$ can be applied to the atomic ensemble in order to map the atomic excitations stored at level $|s\rangle$ in photons in the field 2. If we now look at the joint state between field 1 and field 2, we obtain a state identical to that given in Eq. (2.6.4), just substituting the atomic kets by the photonic kets of field 2 (assuming efficiency equals to 1 for simplicity):

$$|\psi_{2,1}\rangle = \sqrt{1-p}\sum_{n=0}^{\infty} e^{in\beta'} p^{n/2} |n_2, n_1\rangle \,, \tag{2.6.5}$$

where β' is determinated by the propagation of the read field. Note that this state is a two-mode entangled state in the basis of number of photons, in the same way as in the case of PDC [Mandel 1995, Duan 2001].

Finally, it should be noted that the reading process is not necessarily simultaneous with the writing process. In fact, in most experiments based on the DLCZ scheme, these processes are not, so it is necessary that the information recorded in the internal levels of the atoms (during the writing process) to be preserved from decoherence processes, in such a way that the atomic medium behaves like a memory. Therefore, the use of the memory allows the collective atomic excitations entangled with photons in field 1 to be stored in the atomic ensemble for a finite time until they are mapped in photons of field 2. This is basically the main idea of the DLCZ protocol for the generation of pairs of entangled photons from a cold atomic ensemble.

2.6.2 *Single-photon superradiance*

Writing process

Let us consider an ensemble of three-level systems in lambda-like configuration (see write process in Fig. 14), where we initially pump all N atoms to state $|g\rangle$. Thus, the atomic ensemble is initially in the state given by Eq. (2.6.1). The system is excited by an off-resonant writing beam[9], with wavevector $\vec{k}_w$ and frequency $\omega_w = ck_w$, inducing the transition $|g\rangle \rightarrow |e\rangle \rightarrow |s\rangle$ in only one of the atoms of the ensemble. Consequently, it leads to the emission of a photon, with wavevector $\vec{k}$, on the $|e\rangle \rightarrow |s\rangle$ transition whose

[9]This beam acts in the form of a weak square pulse for easy of calculation.

properties depend on the collective atomic state. This process is often called spontaneous Raman emission. Treating the writing beam as a classical field and the other modes of the electromagnetic field as quantum fields initially in vacuum, the effective Hamiltonian that governs the time evolution of the system can be written as [Ortiz-Gutiérrez 2017]

$$\hat{H} = \hat{H}_0 + \hat{V}, \tag{2.6.6}$$

with

$$\hat{H}_0 = \int d^3k\, \hbar\omega_{\vec{k}} \hat{a}^\dagger_{\vec{k}} \hat{a}_{\vec{k}} + \sum_{i=1}^{N} \left[\hbar\omega_g |g_i\rangle\langle g_i| + \hbar\omega_s |s_i\rangle\langle s_i|\right], \tag{2.6.7}$$

$$\hat{V} = \int d^3k \sum_{i=1}^{N} \left[\hbar\Omega_{\vec{k},i} \hat{\sigma}_{gs,i} \hat{a}_{\vec{k}} e^{-i\left(\vec{k}_w - \vec{k}\right)\cdot\vec{r}_i} e^{i(\omega_w + \omega_{gs} - \omega_{\vec{k}})t} + H.c.\right], \tag{2.6.8}$$

where $\hat{\sigma}_{gs,i} \equiv |g_i\rangle\langle s_i|$ and the summation is evaluated over all atoms of the ensemble (each one at the position $\vec{r}_i$). $\hat{a}_{\vec{k}}$ corresponds to the annihilation operator for an electromagnetic mode with wavevector $\vec{k}$. $\hat{H}_0$ is the free Hamiltonian for the atoms of the ensemble and the electromagnetic field. $\hat{V}$ corresponds to the term that governs the effective interaction of the atoms with the incident writing beam, which induces transitions between levels $|g\rangle$ and $|s\rangle$[10]with the effective Rabi frequency $\Omega_{\vec{k},i}$, which depends on the amplitude ($\mathcal{E}_w$) and detuning (Δ) of the writing beam and on the dipole moments (μ) of the transitions $|g\rangle \to |e\rangle$ and $|e\rangle \to |s\rangle$, i.e., $\Omega_{\vec{k},i} \propto \mathcal{E}_w \mu_{ge} \mu_{es}/\Delta$.

Considering the initial state of the atom-light system as given by

$$|\psi(t=0)\rangle_I = |0_a\rangle|0\rangle = |g,0\rangle, \tag{2.6.9}$$

where the field in the $|e\rangle \to |s\rangle$ transition is in an electromagnetic vacuum state $|0\rangle$, the Hamiltonian evolution generates the following state in the interaction picture (at first order in $\Omega_{\vec{k},i}$)

$$|\psi(t > T_p)\rangle_I = |g,0\rangle - i \int d^3k \sum_{i=1}^{N} \Omega^*_{\vec{k},i} e^{i\left(\vec{k}_w - \vec{k}\right)\cdot\vec{r}_i} \int_0^{T_p} dt' e^{-i(\omega_w + \omega_{gs} - \omega_{\vec{k}})t'} |s_i, 1_{\vec{k}}\rangle, \tag{2.6.10}$$

where $\omega_{gs} \equiv \omega_g - \omega_s$, T_p is the temporal width of the writing pulse, and $|s_i, 1_{\vec{k}}\rangle$ represents a state with atom i in $|s\rangle$, all others in the state $|g\rangle$, and with one photon with wavevector $\vec{k}$ in the system.

The state of Eq. (2.6.10) presents intricate entanglement between the atomic collective state (where we do not know which atom was transferred to the state $|s\rangle$) and the light

[10]Note that we have considered the detuning of the writing beam large enough to adiabatically eliminate the level $|e\rangle$ and describe the Raman process as a direct transition $|g\rangle \to |s\rangle$.

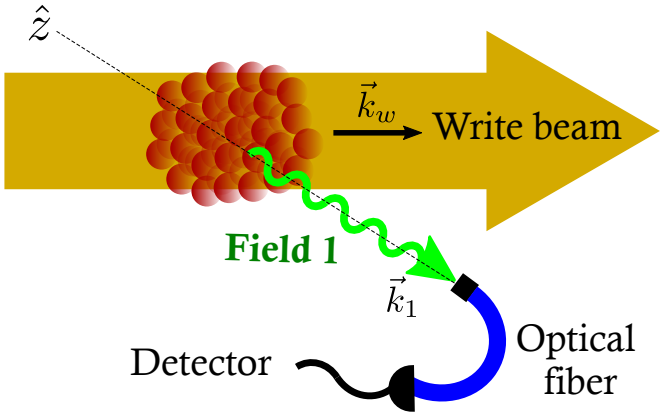

Figure 15: Gaussian optical mode selected by an optical fiber in the writing process.

mode with one photon. However, the light mode is not very well defined. In principle, the photon $\left|1_{\vec{k}}\right\rangle$ can point in any direction. Therefore, in order to overcome this problem, we will concentrate on a single mode of emission, which will then be entangled with a single well-defined collective mode. For this, the first step is to use a write beam that can be approximated by a plane wave. Next, we consider the projection in a specific Gaussian mode $\hat{a}_1$ of the field, which can be selected by a single-mode optical fiber and detected in a photon detector as shown in Fig. 15. We consider the direction of detection as being the z-axis. This optical mode can be written as a superposition of modes $\hat{a}_{\vec{k}}$ of plane wave, namely,

$$\hat{a}_1 = \int d\vec{q}_1 \phi_1(\vec{q}_1) \hat{a}_{\vec{q}_1 + \sqrt{k_1^2 - q_1^2}\hat{z}}, \tag{2.6.11}$$

where $\vec{q}_1$ represents the component of $\vec{k}_1$ in the xy plane and the function $\phi_1(\vec{q}_1)$ defines the mode (considered to be monochromatic). A quantum state with a photon in this mode can be written as $\hat{a}_1^\dagger|0\rangle$, so that the projection in that state is made from the operator $\langle 0|\hat{a}_1$. We can see the writing process as the coherent scattering of one photon of the writing laser beam, which is treated as a classical field, into one photon in the mode defined by $\hat{a}_1$, together with a corresponding change on the quantum state of the atom that scattered the photon [Monken 2013].

Considering that T_p is long enough and using the paraxial approximation $\sqrt{k_1^2 - q_1^2} \approx k_1 - q_1^2/(2k_1)$, we have that the state of the system after performing the projection in the detected mode is given by

$$\langle 0|\hat{a}_1|\psi(t > T_p)\rangle_I \propto |1_a\rangle, \tag{2.6.12}$$

with

$$|1_a\rangle = \sum_{i=1}^{N} c_i e^{i(\vec{k}_w - k_1\hat{z})\cdot\vec{r}_i}|s_i\rangle, \tag{2.6.13}$$

and

$$c_i = \int d\vec{q}_1 \phi_1(\vec{q}_1) e^{i[-\vec{q}_1\cdot\vec{\rho}_i + z_i q_1^2/2k_1]}, \tag{2.6.14}$$

where $\vec{\rho}_i$ is the component of $\vec{r}_i$ in the xy plane and $\sum_i |c_i|^2 = 1$.

Equation (2.6.12) provides, in a simplified way, the result of the projection of the atomic state due to the detection of a photon in mode 1. Once this detection has occurred, the resulting state needs to be normalized again, leading to the final state of the detection process

$$|\psi_f\rangle_I = |1_a\rangle. \tag{2.6.15}$$

We can see then that the detection of a photon in mode 1 "prepares" the ensemble of atoms in a well defined collective state, which can be read out very efficiently by converting the collective atomic excitation into one photon that propagates in a well-defined direction, thanks to collective interference. This will be discussed in what follows.

Reading process

Once the atomic medium is prepared in the state given by Eq. (2.6.15), it is possible to convert the atomic excitation to a second mode of the light field, field 2, with high efficiency. In what follows, we briefly discuss this conversion process. The technical details of the calculations can be found in [Ortiz-Gutiérrez 2017].

As discussed in the subsection 2.6.1, we consider now the incidence of another intense field, the reading beam, resonant on the $|s\rangle \rightarrow |e\rangle$ transition (see read process in Fig. 14). This beam has amplitude $\mathcal{E}_r$, wavevector $\vec{k}_r$ and frequency $\omega_r = ck_r$. We act with the reading beam in resonance for two reasons: to increase the probability of the mapping $|s\rangle \rightarrow |e\rangle$, and to induce transparency in the medium to increase the extraction efficiency of light emitted in the $|e\rangle \rightarrow |g\rangle$ transition [Boller 1991]. It is important to stress from the beginning that the $|s\rangle \rightarrow |e\rangle \rightarrow |g\rangle$ transition must be much more probable that the $|s\rangle \rightarrow |e\rangle \rightarrow |s\rangle$ transition, because in the first all the atoms end in the same state of the ensemble before the writing process (see Eq. 2.6.1). This results in a large constructive interference reinforcing a global parametric process (same initial and final states), with conservation of momentum and energy in the atomic ensemble. Even so, we will consider the $|s\rangle \rightarrow |e\rangle \rightarrow |s\rangle$ transition in the theoretical model in order to obtain a better quantitative description of the reading process. The Hamiltonian that governs the time evolution of the system can then be written as

$$\hat{H} = \hat{H}_0 + \hat{V}_1 + \hat{V}_2 + \hat{V}_3, \tag{2.6.16}$$

with

$$\hat{H}_0 = \int d^3k\, \hbar\omega_{\vec{k}} \hat{a}^\dagger_{\vec{k}} \hat{a}_{\vec{k}} + \sum_i \left[E_g|g_i\rangle\langle g_i| + E_s|s_i\rangle\langle s_i| + E_e|e_i\rangle\langle e_i|\right], \tag{2.6.17}$$

$$\hat{V}_1 = -\sum_i \left[\hbar g_{es} \hat{\sigma}_{es,i} \mathcal{E}_r e^{i\vec{k}_r\cdot\vec{r}_i} e^{i(\omega_{es}-\omega_r)t} + H.c.\right], \tag{2.6.18}$$

$$\hat{V}_2 = -\sum_i \left[\int d^3k\, \hbar g_{eg,\vec{k}} \hat{\sigma}_{eg,i} \hat{a}_{\vec{k}} e^{i\vec{k}\cdot\vec{r}_i} e^{i(\omega_{eg}-\omega_{\vec{k}})t} + H.c.\right], \tag{2.6.19}$$

$$\hat{V}_3 = -\sum_i \left[\int d^3k\, \hbar g_{es,\vec{k}} \hat{\sigma}_{es,i} \hat{a}_{\vec{k}} e^{i\vec{k}\cdot\vec{r}_i} e^{i(\omega_{es}-\omega_{\vec{k}})t} + H.c.\right]. \tag{2.6.20}$$

Here $\hat{H}_0$ is the free Hamiltonian for the atoms of the ensemble and the electromagnetic field. $\hat{V}_1$ corresponds to the term that governs the interaction of the atoms with the incident reading beam, which induces transitions between levels $|s\rangle$ and $|e\rangle$. g_{es} depends on the dipole moment of the transition. This term generates Rabi oscillations between levels $|s\rangle$ and $|e\rangle$ [Scully 1997]. $\hat{V}_2$ and $\hat{V}_3$ correspond to the terms that govern the interaction of the atoms with other modes of the electromagnetic field, which are treated as quantum fields, inducing a spontaneous decay from level $|e\rangle$ to levels $|g\rangle$ or $|s\rangle$ with the emission of one photon [Scully 1997]. $g_{eg,\vec{k}}$ and $g_{es,\vec{k}}$ depend on the dipole moment of the transition and on the wavevector $\vec{k}$ of the interacting electromagnetic mode.

Considering the initial state of the atom-light system is

$$|\psi(0)\rangle = |1_a\rangle|0\rangle = \sum_{i=1}^{N} c_i e^{i(\vec{k}_w - k_1\hat{z})\cdot\vec{r}_i} |s_i, 0\rangle, \tag{2.6.21}$$

where $|1_a\rangle$ is given by Eq. (2.6.15), the Hamiltonian evolution generates the following general state in the interaction picture:

$$|\psi(t)\rangle_I = \sum_i e^{i(\vec{k}_w - k_1\hat{z})\cdot\vec{r}_i} \left[A_i(t)|s_i, 0\rangle + B_i(t)|e_i, 0\rangle\right] + \int d^3\vec{k}\, C_{\vec{k}}(t)|g, 1_{\vec{k}}\rangle + \sum_i \int d^3\vec{k}\, D_{i,\vec{k}}(t)|s, 1_{\vec{k}}\rangle, \tag{2.6.22}$$

where $|e_i, 0\rangle$ represents a state with atom i in state $|e\rangle$, with all other atoms in state $|g\rangle$, and with no photons in the system; $|g, 1_{\vec{k}}\rangle$ represents a state with all atoms in state $|g\rangle$ and one photon with wavevector $\vec{k}$ in the system; and so on. Note that since there is initially only one excitation in state $|s\rangle$, the temporal evolution remains essentially restricted to

the space of a single excitation.

The time evolution of the state of Eq. (2.6.22) can be computed using the Schrödinger equation in the interaction picture, from which we conclude that the coefficients A_i, B_i, $C_{\vec{k}}$ and $D_{i,\vec{k}}$ obey the following set of differential equations:

$$\frac{\partial A_i(t)}{\partial t} = ig^*_{es}\mathcal{E}^*_r e^{-i\vec{k}_r\cdot\vec{r}_i}B_i(t), \tag{2.6.23}$$

$$\frac{\partial B_i(t)}{\partial t} = ig_{es}\mathcal{E}_r e^{i\vec{k}_r\cdot\vec{r}_i}A_i(t) + i\int d^3k e^{i(-\vec{k}_w+k_1\hat{z}+\vec{k})\cdot\vec{r}_i}\times \times\left[g_{eg,\vec{k}}e^{i(\omega_{eg}-\omega_{\vec{k}}t)}C_{\vec{k}}(t)\ g_{es,\vec{k}}e^{i(\omega_{es}-\omega_{\vec{k}})}D_{i,\vec{k}}(t)\right], \tag{2.6.24}$$

$$\frac{\partial C_{\vec{k}}(t)}{\partial t} = i\sum_i g^*_{eg,\vec{k}}e^{i(\vec{k}_w-k_1\hat{z}-\vec{k})\cdot\vec{r}_i}e^{-i(\omega_{eg}-\omega_{\vec{k}})t}B_i(t), \tag{2.6.25}$$

$$\frac{\partial D_{i\vec{k}}(t)}{\partial t} = ig^*_{es,\vec{k}}e^{i(\vec{k}_w-k_1\hat{z}-\vec{k})\cdot\vec{r}_i}e^{-i(\omega_{es}-\omega_{\vec{k}})t}B_i(t). \tag{2.6.26}$$

To solve this system of equations, we assume the following tentative form to $B_i(t)$ [Mendes 2013b]:

$$B_i(t) = \beta_i(t)b_i(t)e^{i\vec{k}_r\cdot\vec{r}_i}, \tag{2.6.27}$$

such that

$$\beta_i(t)\frac{\partial b_i(t)}{\partial t} = ig_{es}\mathcal{E}_r A_i(t), \tag{2.6.28}$$

$$\frac{\partial\beta_i(t)}{\partial t}\cdot b_i(t) = i\int d^3k e^{i(-\vec{k}_W+k_1\hat{z}+\vec{k}-\vec{k}_r)\cdot\vec{r}_i}\times \times\left[g_{eg,\vec{k}}C_{\vec{k}}(t)e^{i(\omega_{eg}-\omega_{\vec{k}}t)} + g_{es,\vec{k}}D_{i\vec{k}}(t)e^{i(\omega_{es}-\omega_{\vec{k}})}\right]. \tag{2.6.29}$$

The advantage of using this form of solution for $B_i(t)$ is that now we have two sets of coupled equations with clearly distinct roles in the system. Eqs. (2.6.23) and (2.6.28) form a system similar to the one for the Rabi oscillation dynamics, while Eqs. (2.6.25), (2.6.26) and (2.6.29) form a system similar to the spontaneous decay dynamics [Scully 1997]. This method of solution will be used to solve the system (2.6.25), (2.6.26) and (2.6.29) and substitute the results to solve the system (2.6.23) and (2.6.28). The final result is the following[11]:

[11] To find the expressions given by Eq. (2.6.30) and (2.6.31) we have considered that the atoms are roughly uniformly illuminated by both write and read fields, which leads to the atomic dynamics for the optical excitation $|s\rangle \rightarrow |e\rangle$ to not vary appreciably from one atom the other, i.e., $\beta_i(t) \approx \beta_j(t)$ and $b_i(t) \approx b_j(t)$.

$$\beta_i(t) = e^{-\chi_i \Gamma t/2}, \tag{2.6.30}$$

$$b_i(t) = i\frac{\Omega_0 c_i e^{\chi_i \Gamma t/4}}{\sqrt{\frac{\chi_i^2\Gamma^2}{4} - |\Omega_0|^2}} \sinh\left(\sqrt{\frac{\chi_i^2\Gamma^2}{4} - |\Omega_0|^2}\, t/2\right), \tag{2.6.31}$$

with

$$\Gamma \equiv \Gamma_{eg} + \Gamma_{es} = \frac{\omega_{eg}^3 \mu_{ge}^2 + \omega_{es}^3 \mu_{se}^2}{3\pi\hbar\epsilon_0 c^3}, \tag{2.6.32}$$

and

$$\chi_i \equiv 1 + \frac{3}{8\pi}\frac{\Gamma_{eg}}{\Gamma}\sum_{j\neq i}\int_0^{2\pi} d\phi \int_0^{\pi} d\theta \sin\theta \cos^2\theta e^{i(\vec{k}_w - k_1\hat{z} - \vec{k} + \vec{k}_r)\cdot(\vec{r}_j - \vec{r}_i)}, \tag{2.6.33}$$

where we have used that $\Omega_0 \equiv 2g_{es}\mathcal{E}_r$, $|g_{eg,\vec{k}}|^2 = \omega_{eg}\mu_{ge}^2 \cos^2\theta/[2(2\pi)^3\epsilon_0\hbar]$, with θ being the angle between $\overrightarrow{\mu}_{eg}$ and the polarization vector of the emitted photon, and similarly for $|g_{es,\vec{k}}|^2$. Here, Γ is the decay rate from the state $|e\rangle$ to the states $|g\rangle$ or $|s\rangle$ for a free atom, according to the Weisskopf-Wigner theory for the spontaneous decay [Scully 1997], and χ_i is the *superradiant enhancement parameter*.

It is possible to find a simpler expression for the parameter χ_i if we consider typical experimental conditions. To do this we need to substitute the summation in Eq. (2.6.33) by an integral over the atomic density of the ensemble, i.e.,

$$\sum_j \to \int d^3r \rho(\vec{r}) \qquad \text{with} \qquad \rho(\vec{r}) = \frac{N}{(2\pi)^{3/2}W^2 L} e^{-\left(x^2+y^2\right)/\left(2W^2\right)} e^{-z^2/(2L^2)}, \tag{2.6.34}$$

where W is the waist of the mode of the detected photon (considered to be Gaussian), L is the width of the ensemble in the z-direction and N is the total number of atoms in this region[12]. For the usual atomic ensembles used for performing quantum memories, typical values for the quantities k, W and L are $k \approx 10^7\,\mathrm{m}^{-1}$, $W \approx 10^{-4}\,\mathrm{m}$ and $L \approx 10^{-3}\,\mathrm{m}$. Thus, since $\vec{k}_w \approx -\vec{k}_r$ and $k_1 \approx k$, we find that the average value for χ_i is given by [Mendes 2013b]

$$\chi = \langle\chi_i\rangle = 1 + \frac{N}{2W^2k^2}. \tag{2.6.35}$$

An important point to note in this expression is the independence of χ on L, typical of a superradiant emission from a cigar-shaped ensemble. Optical depth (OD) is defined as the natural logarithm of the ratio of incident to transmitted radiant power through a

[12]Only the atoms that are in the region of the mode of the detected photon can store the excitation, so only these atoms are considered to compute χ_i

material. From an experimental point of view $N \propto \mathrm{OD}$. In this way, the optical depth parameterize the modification of χ in the ensemble.

Substituting Eqs. (2.6.30) and (2.6.31) in Eq. (2.6.27), we arrive at

$$B_i(t) = i\frac{\Omega_0 c_i e^{-\chi_i \Gamma t/4} e^{i\vec{k}_r\cdot\vec{r}_i}}{\sqrt{\frac{\chi_i^2\Gamma^2}{4} - |\Omega_0|^2}} \sinh\left(\sqrt{\frac{\chi_i^2\Gamma^2}{4} - |\Omega_0|^2}\, t/2\right). \tag{2.6.36}$$

In this expression we can see clearly the Rabi oscillation behavior superposed with the spontaneous decay. Unlike the semiclassical treatment where similar time dependences for the optical coherence (combining exponential decay and a hyperbolic sine function) are commonly deduced [Moretti 2008], we have now a *spontaneous superradiant emission* (for $\chi_i > 1$) with a single photon being emitted collectively by the ensemble of atoms. In other words, we have an increase of the decay rate induced by the presence of the other atoms, a phenomenon known as *superradiance* [Dicke 1954]. This increase of the decay rate is not the result of stimulated emission, since only one photon is emitted by the ensemble, but an effect that depends on the coherent distribution of the excitation through the atoms of the ensemble, that is, it depends on a strong constructive interference of the atoms induced by the system's entanglement.

Wave function of the emitted photon in the reading process

We can now proceed to finding the spatial mode and temporal dependence of the photon emitted in the reading process. There are two possibilities for the generation of a photon from the spontaneous emission of level $|e\rangle$:

1. $|e\rangle \to |s\rangle$ *emission*: in this case, we necessarily have that the atom that was in $|s_i\rangle$ will return to $|s_i\rangle$. According Eq. (2.6.22), if we trace out the atomic degrees of freedom, we have an expression of the type $\sum_i |D_{i,\vec{k}}(t)|^2$, with $D_{i,\vec{k}}(t)$ given by Eq. (2.6.26), for each component $\vec{k}$ of the field. Note that the dependence of $D_{i,\vec{k}}$ on the spatial phase $e^{i(\vec{k}_w - k_1\hat{z} - \vec{k} + \vec{k}_r)\cdot\vec{r}_i}$ does not select any preferential direction on the photon emission and therefore the information imprinted in the quantum memory is lost.

2. $|e\rangle \to |g\rangle$ *emission*: in this case, all atoms will end up in the same level $|g\rangle$. According Eq. (2.6.22), if we trace out the atomic degrees of freedom, we have then an expression such as $|\int d^3\vec{k} c_{\vec{k}}(t)|^2$, with $C_{\vec{k}}(t)$ given by Eq. (2.6.25), highly sensitive to the spatial phase $e^{i(\vec{k}_w - k_1\hat{z} - \vec{k} + \vec{k}_r)\cdot\vec{r}_i}$ of each atom. We can see that the summation of the spacial terms in Eq. (2.6.25) generates the directionality of the emitted photon, since $\vec{k}_w \approx -\vec{k}_r$ in the experiments and there is constructive interference only for $\vec{k} \approx -k_1\hat{z}$. So, the information imprinted in the quantum memory is transferred to the photonic state. On the other hand, if the atomic density of the ensemble is small

(OD small) such that there are no superradiance effects on the photon emission and $\chi \approx 1$ (see Eq. (2.6.35)), since the decay rates from level $|e\rangle$ to levels $|g\rangle$ and $|s\rangle$ are aproximately the same, there is a fundamental limit of 50% for the efficiency of this quantum memory even if all decoherence processes and losses are perfectly eliminated. However, when $\chi > 1$, this efficiency may increase since the decay rate from level $|e\rangle$ to level $|g\rangle$ increases by a factor $2\chi - 1$ in relation to the decay rate from level $|e\rangle$ to level $|s\rangle$ [Mendes 2013b]. So, the higher the value of χ, the more efficient the overall quantum memory readout is [de Oliveira 2014].

Let us focus now in the second situation, i.e., in the emission of a photon on $|e\rangle \rightarrow |g\rangle$ transition. In this case the decomposition into wavevectors of the state of the emitted photon is given by $\mathrm{Lim}_{t\rightarrow\infty} C_{\vec{k}}(t)$, with $C_{\vec{k}}(t)$ given by Eq. (2.6.25). To find the wave packet of the emitted photon we must apply a Fourier transform over its frequency spectrum. Let's define the photonic mode ψ_2 in terms of $\vec{q}$, the wave vector component of photon 2 extracted in the xy plane. We have thus

$$\psi_2(\vec{q}, t) \propto \int d\omega_{\vec{k}} e^{-i\omega_{\vec{k}} t} \lim_{t'\rightarrow\infty} C_{\vec{k}}(t'). \tag{2.6.37}$$

In order to obtain an analytical expression for the photonic wave packet extracted from the memory, we consider an important approximation: χ_i will have the same value for all atoms in the ensemble, i.e., $\chi_i \approx \chi$. Therefore, Eq. 2.6.36 becomes

$$B_i(t) = c_i e^{i\vec{k}_r \cdot \vec{r}_i} B(t), \tag{2.6.38}$$

with

$$B(t) = i \frac{\Omega_0 e^{-\chi\Gamma t/4}}{\sqrt{\frac{\chi^2\Gamma^2}{4} - |\Omega_0|^2}} \sinh\left(\sqrt{\frac{\chi^2\Gamma^2}{4} - |\Omega_0|^2}\, t/2\right), \tag{2.6.39}$$

having the same value for all atoms in the ensemble. Replacing Eq. (2.6.25) in Eq. (2.6.37), using Eqs. (2.6.36) and (2.6.14), and considering a cigar-shaped ensemble with atomic density given by Eq. (2.6.34), we obtain [Mendes 2013a, Ortiz-Gutiérrez 2017]

$$\psi_2(\vec{q}, t) \propto \phi_1(-\vec{q}) e^{-L^2(k_{1z}+k_z)^2/2} B(t) e^{-i\omega_{eg} t}. \tag{2.6.40}$$

This expression demonstrates that the second photon is extracted in the conjugated mode to field 1, with $k_z \approx -k_{1z}$ and the corresponding transverse mode ϕ_1, as expected[13]. In addition, we can see that its wave packet oscillates with a central frequency ω_{eg}. The

[13]It worth mentioning that this directionality on the emission of the second photon depends only on the extension of the atomic ensemble over large distances compared to λ. Once this condition is fulfilled, the directionality in the reading process grows proportionally to N^2, a very well known effect in such four-wave mixing systems [Mendes 2013b].

conditional probability density $\rho_c(t)$ to detect the second photon at time t once the first photon was detected is then given by

$$\rho_c(t) = F|B(t)|^2, \tag{2.6.41}$$

with F being a proportionality constant including, among other factors, the detection efficiency, and $B(t)$ given by Eq. (2.6.39). Obviously, in Eq. (2.6.41) we consider a very small detection window, so we can assume F constant throughout its duration. Another important quantity is the total conditional probability p_c:

$$p_c = \int_0^\infty \rho_c(t)dt, \tag{2.6.42}$$

which gives the total probability of extracting the information stored in the medium, mapping it in a photon in field 2. To compare theory and experiment, the normalized conditional probability density is particularly important:

$$\widetilde{\rho}_c(t) \equiv \frac{\rho_c(t)}{p_c} = \frac{|B(t)|^2}{\int_0^\infty |B(t)|^2 dt}, \tag{2.6.43}$$

which is independent of F. Finally, using Eq. (2.6.39), the above equation can be rewritten as follows

$$\widetilde{\rho}_c(t) = \alpha\, e^{-\chi\Gamma t/2} \sin^2\left(\frac{\Omega t}{2}\right), \tag{2.6.44}$$

with $\alpha = \chi\Gamma\Omega_0^2/\Omega^2$ and $\Omega = \sqrt{\Omega_0^2 - \chi^2\Gamma^2/4}$. Remember that Γ is the natural linewidth for level $|e\rangle$, Ω_0 the reading Rabi frequency, and χ the superradiant enhancement for the $|e\rangle \to |g\rangle$ decay.

2.6.3 *Two-photon superradiance*

Recently, a theoretical analysis of the reading process of an atomic memory containing two excitations of a collective atomic state was developed [Barros 2018]. Basically, this analysis tells us that if we neglect the reabsorption of the photons by the atomic ensemble, the two-photon wavepacket can be found from the following simple expression

$$\widetilde{\rho}_{cc}(t_1, t_2) = \widetilde{\rho}_c(t_1)\widetilde{\rho}_c(t_2), \tag{2.6.45}$$

where $\widetilde{\rho}_c(t)$ is the single-photon wavepacket given by Eq. (2.6.44). This approximation is well justified in our system (see chapter 4) since the reading process occurs in a condition of Electromagnetically Induced Transparency (EIT) [Boller 1991], in which the read pulse induces a transparency in the medium for the outgoing photons. As highlighted in Ref. [de Oliveira 2014], this is an interesting feature of the present system to study superradiance,

since it eliminates various complications coming from propagation effects mixed with the superradiant dynamics [Gross 1982b].

From Eq. (2.6.44) and the simple expression above relating it to the two-photon wavepacket, we derive then the corresponding theoretical functions. By having $t_2 = t_1 + \tau > t_1$, we can integrate over τ to obtain the normalized conditional probability density to detect in t_1 the first photon of the pair in field 2:

$$\widetilde{\rho}_{c1}(t_1) = 2\,\alpha\, e^{-\chi\Gamma t} \sin^2\left(\frac{\Omega t}{2}\right)\left[1 + \frac{\chi\Gamma\Omega}{2\Omega_0^2}\sin(\Omega t) - \left(\frac{\chi\Gamma}{2\Omega_0}\right)^2 \cos(\Omega t)\right]. \qquad (2.6.46)$$

On the other hand, if the integration run over t_1, we obtain the normalized conditional probability density to detect the second photon in field 2 at a time τ after the first one was detected:

$$\widetilde{\rho}_{c\tau}(\tau) = \frac{\chi\Gamma\Omega_0^4}{2\Omega^4} e^{-\chi\Gamma\tau/2}\left\{\frac{\Omega^2}{\Omega^2 + \chi^2\Gamma^2} + \left(\frac{\Omega}{\Omega^2 + \chi^2\Gamma^2} - \frac{\Omega}{2\Omega_0^2}\right)\left[\Omega\cos(\Omega\tau) + \chi\Gamma\sin(\Omega\tau)\right]\right\}. \qquad (2.6.47)$$

These wavepackets clearly reproduce the essential aspects found in the previous subsection, that is, an exponential decay amplified by the superradiance effect combined with an oscillatory term.

3 Quantum description of the optical parametric oscillator

In this chapter, we present a new theoretical model that completely describes the quantum state of an OPO operating above threshold [Muñoz Martínez 2017]. The formalism is carried out in the frequency domain in order to compare its predictions with experimental results obtained using methods of self-homodyning [Villar 2004] and demodulation by in-quadrature local oscillators [Barbosa 2013c]. In addition, we also present an analysis of the entanglement in this system, which is published in [Barbosa 2017].

We begin by presenting the Hamiltonian for the sideband coupling in the nonlinear medium (Sec. 3.1), and the evolution of the field operators under propagation on this medium (Sec. 3.2). It is followed by the detailed model for the open cavity that is used to evaluate the operators of the output field (Sec. 3.3). With the relation between the output and the input modes, momenta of any order can be evaluated. In the present scenario, we will limit the study to the second order momenta, and the reconstruction of the covariance matrix (Sec. 3.4). Nevertheless, the description wouldn't be complete without the coupling of phonons to the sideband modes, included in the Hamiltonian of the system (Sec. 3.5). The obtained results are used to describe experimental results at different pump powers (Sec. 3.6), with pump powers up to 75% above the oscillation threshold. Finally, in subsection 3.6.2, we analyze in detail the hexapartite entanglement present in this system from the experimental data and with the help of the PPT criterion discussed in subsection 2.1.2.

3.1 Interaction Hamiltonian in the sidebands

As discussed in Sec. 2.3, on the heart of the OPO lies the coupling of three modes of the electromagnetic field, that can be described by the well known Hamiltonian of spontaneous parametric down conversion process, given by [Eq. (2.3.1)]

$$\hat{H}_\chi = i\hbar\frac{\chi}{\tau}\left[\hat{a}^{(0)}(t)\hat{a}^{(1)\dagger}(t)\hat{a}^{(2)\dagger}(t) - \text{h.c.}\right]. \tag{3.1.1}$$

Each annihilation operator of the field $\hat{a}^{(n)}(t)$ is associated with the electric field operator of a propagating wave and, in the limit of a cavity of infinite size, can be described

by the contribution of operators at each frequency mode as [Walls 2008]

$$\hat{a}^{(n)}(t) = e^{-i\omega_n t} \int_{-\omega_n}^{\infty} d\Omega e^{-i\Omega t} \hat{a}^{(n)}_{\omega_n+\Omega}, \tag{3.1.2}$$

where $\hat{a}_{\omega_n+\Omega}$ is the photon annihilation operator in the mode of frequency $\omega = \omega_n + \Omega$, and we explicitly identify the carrier frequency of each field (ω_n) and the frequency shift of each sideband relative to this carrier Ω. The mode (n) specifies different directions of propagation, polarizations or carrier frequencies. As in the situations we have in the laboratory $\Omega \ll \omega_n$ then we can approximate ω_n by ∞ in the integration limit in Eq. (3.1.2).

A usual treatment in optical systems considers as *carrier* the mode with a significant population of photons, that is much larger than the average number of photons on all other modes. Therefore, in a linearized description of the fields by their mean value and a fluctuation, where each mode is described as $\hat{a}^{(n)}_{\omega_n+\Omega} = \langle \hat{a}^{(n)}_{\omega_n+\Omega} \rangle + \delta\hat{a}^{(n)}_{\omega_n+\Omega}$, we consider that $|\alpha_{\omega_n}|^2 \equiv \langle \hat{a}^{(n)\dagger}_{\omega_n} \hat{a}^{(n)}_{\omega_n} \rangle \gg \langle \hat{a}^{(n)\dagger}_{\omega_n+\Omega} \hat{a}^{(n)}_{\omega_n+\Omega} \rangle$ for $|\Omega| > \epsilon$, where α_{ω_n} is the mean field of the carrier mode (n) and ϵ is the carrier linewidth. In this approximation,

$$\hat{a}_n(t) \simeq \alpha_{\omega_n} \hat{1} + \int' d\Omega e^{-i\Omega t} \hat{a}^{(n)}_{\omega_n+\Omega}, \tag{3.1.3}$$

where the symbol $\int'$ represents integration in $(-\infty, \infty)$, but without the null frequency.

Using Eq. (3.1.3), we have

$$\begin{aligned}
\hat{a}^{(0)\dagger}(t)\hat{a}^{(1)}(t)\hat{a}^{(2)}(t) &= \left(\alpha^*_{\omega_0} + \int^{'} d\Omega e^{i\Omega t}\hat{a}^{(0)\dagger}_{\omega_0+\Omega}\right)\left(\alpha_{\omega_1} + \int^{'} d\Omega' e^{-i\Omega' t}\hat{a}^{(1)}_{\omega_1+\Omega'}\right) \\
&\qquad \left(\alpha_{\omega_2} + \int^{'} d\Omega'' e^{-i\Omega'' t}\hat{a}^{(2)}_{\omega_2+\Omega'}\right), \\
&= e^{i(\omega_0-\omega_1-\omega_2)t}\left[\alpha^*_{\omega_0}\alpha_{\omega_1}\alpha_{\omega_2} + \alpha^*_{\omega_0}\alpha_{\omega_1}\int^{'} d\Omega e^{-i\Omega t}\hat{a}^{(2)}_{\omega_2+\Omega}\right. \\
&\quad +\alpha^*_{\omega_0}\alpha_{\omega_2}\int^{'} d\Omega e^{-i\Omega t}\hat{a}^{(1)}_{\omega_1+\Omega} + \alpha_{\omega_1}\alpha_{\omega_2}\int^{'} d\Omega e^{i\Omega t}\hat{a}^{(0)\dagger}_{\omega_0+\Omega} \\
&\quad +\alpha^*_{\omega_0}\int^{'} d\Omega d\Omega' e^{-i(\Omega+\Omega')t}\hat{a}^{(1)}_{\omega_1+\Omega}\hat{a}^{(2)}_{\omega_2+\Omega'} \\
&\quad +\alpha_{\omega_1}\int^{'} d\Omega d\Omega' e^{i(\Omega-\Omega')t}\hat{a}^{(0)\dagger}_{\omega_0+\Omega}\hat{a}^{(2)}_{\omega_2+\Omega'} \\
&\quad +\alpha_{\omega_2}\int^{'} d\Omega d\Omega' e^{i(\Omega-\Omega')t}\hat{a}^{(0)\dagger}_{\omega_0+\Omega}\hat{a}^{(1)}_{\omega_1+\Omega'} \\
&\quad \left. +\int^{'} d\Omega d\Omega' d\Omega'' e^{i(\Omega-\Omega'-\Omega'')t}\hat{a}^{(0)\dagger}_{\omega_0+\Omega}\hat{a}^{(1)}_{\omega_1+\Omega'}\hat{a}^{(2)}_{\omega_2+\Omega''}\right]. \quad (3.1.4)
\end{aligned}$$

As we are interested in processes which fulfill the condition of energy conservation, the exponential outside the brackets is equal to 1. Now, the first term in the brackets is constant and can be disregarded from the Hamiltonian. The next three terms do not satisfy the condition of energy conservation and therefore will give positive or negative contributions, depending on the region within the crystal. For a long crystal, they have no effective contribution. The last term within the brackets, only depends on the sidebands and is much smaller than those that depend linearly on the carriers. Thus, Eq (3.1.4) can be approximated by

$$\begin{aligned}
\hat{a}^{(0)\dagger}(t)\hat{a}^{(1)}(t)\hat{a}^{(2)}(t) = \alpha^*_{\omega_0}&\int^{'} d\Omega d\Omega' e^{-i(\Omega+\Omega')t}\hat{a}^{(1)}_{\omega_1+\Omega}\hat{a}^{(2)}_{\omega_2+\Omega'} \\
&+ \alpha_{\omega_1}\int^{'} d\Omega d\Omega' e^{i(\Omega-\Omega')t}\hat{a}^{(0)\dagger}_{\omega_0+\Omega}\hat{a}^{(2)}_{\omega_2+\Omega'} \\
&+ \alpha_{\omega_2}\int^{'} d\Omega d\Omega' e^{i(\Omega-\Omega')t}\hat{a}^{(0)\dagger}_{\omega_0+\Omega}\hat{a}^{(1)}_{\omega_1+\Omega'}. \quad (3.1.5)
\end{aligned}$$

Only frequencies such that $\Omega' = -\Omega$, for the first term, or $\Omega' = \Omega$ for the second and third terms, satisfy the energy conservation condition. Consequently, for a long crystal, we have

$$\hat{a}^{(0)\dagger}(t)\hat{a}^{(1)}(t)\hat{a}^{(2)}(t) = \int' d\Omega \left[\alpha^{*}_{\omega_0}\hat{a}^{(1)}_{\omega_1+\Omega}\hat{a}^{(2)}_{\omega_2-\Omega} + \alpha_{\omega_1}\hat{a}^{(0)\dagger}_{\omega_0+\Omega}\hat{a}^{(2)}_{\omega_2+\Omega} + \alpha_{\omega_2}\hat{a}^{(0)\dagger}_{\omega_0+\Omega}\hat{a}^{(1)}_{\omega_1+\Omega}\right], \quad (3.1.6)$$

Finally, the Hamiltonian given in Eq (3.1.1) can be rewritten with the help of Eq (3.1.6) as follows

$$\hat{H}_{\chi} = \int_{\epsilon}^{\infty} d\Omega \hat{H}_{\chi}(\Omega), \quad (3.1.7)$$

where

$$\begin{aligned}\hat{H}_{\chi}(\Omega) = -i\hbar\frac{\chi}{\tau}\Big[\alpha^{*}_{\omega_0}\Big(\hat{a}^{(1)}_{\omega_1+\Omega}\hat{a}^{(2)}_{\omega_2-\Omega} + \hat{a}^{(1)}_{\omega_1-\Omega}\hat{a}^{(2)}_{\omega_2+\Omega}\Big) + \\ \alpha_{\omega_1}\left(\hat{a}^{(0)\dagger}_{\omega_0+\Omega}\hat{a}^{(2)}_{\omega_2+\Omega} + \hat{a}^{(0)\dagger}_{\omega_0-\Omega}\hat{a}^{(2)}_{\omega_2-\Omega}\right) + \\ \alpha_{\omega_2}\left(\hat{a}^{(0)\dagger}_{\omega_0+\Omega}\hat{a}^{(1)}_{\omega_1+\Omega} + \hat{a}^{(0)\dagger}_{\omega_0-\Omega}\hat{a}^{(1)}_{\omega_1-\Omega}\right) - \text{h.c.}\Big]. \quad (3.1.8)\end{aligned}$$

Note that, under the validity of linearization, each set of sideband pairs defined by $\Omega > \epsilon$ is decoupled from others sets defined by $\Omega' \neq \Omega$.

On the other hand, upper and lower sidebands are coupled in pairs in Eq. (3.1.8). The field operators of these sidebands are pairwise measured by the treatment of detected photocurrents in the frequency domain [Barbosa 2013b, Barbosa 2013c]. The treatment for the evolution of these operators can be simplified if we change to the measurement basis involving symmetric ($\mathcal{S}$) and antisymmetric ($\mathcal{A}$) combinations of upper and lower sidebands operators [Barbosa 2013c]

$$\hat{a}^{(n)}_{s(a)} = \frac{1}{\sqrt{2}}\Big[\hat{a}^{(n)}_{\omega_n+\Omega} \pm \hat{a}^{(n)}_{\omega_n-\Omega}\Big]. \quad (3.1.9)$$

On this basis, the Hamiltonian given in Eq. (3.1.8) is rewritten as

$$\hat{H}_{\chi}(\Omega) = \hat{H}_{\chi s} + \hat{H}_{\chi a}, \quad (3.1.10)$$

where

$$\hat{H}_{\chi s(a)} = -i\hbar\frac{\chi}{\tau}\Big[\pm\alpha^{*}_{\omega_0}\hat{a}^{(1)}_{s(a)}\hat{a}^{(2)}_{s(a)} + \alpha_{\omega_1}\hat{a}^{(0)\dagger}_{s(a)}\hat{a}^{(2)}_{s(a)} + \alpha_{\omega_2}\hat{a}^{(0)\dagger}_{s(a)}\hat{a}^{(1)}_{s(a)} - \text{h.c.}\Big], \quad (3.1.11)$$

where the $+$ $(-)$ signal is used for the symmetric (antisymmetric) combination of sidebands along this article. This Hamiltonian describes a process leading to two-mode squeezing involving downconverted modes $\hat{a}^{(1)}_{s(a)}$ and $\hat{a}^{(2)}_{s(a)}$ mediated by the intense pump field, and two beam splitter processes exchanging photons between the pump and each down-

converted mode, mediated by the intense complementary downconverted field. These three processes lead to a rich entanglement dynamics, that was understood as a source of tripartite entangled fields in the symmetric mode description [Villar 2006]. Beyond this three mode description, a rich mesh of entanglement dynamics involving six modes is generated by Eq. (3.1.8), combining creation and annihilation of pairs of photons in downconverted sidebands and photon exchange between pump and downconverted sidebands, leading to hexapartite entanglement among the involved modes as we will see later in subsection 3.6.2.

On the other hand, Eq. (3.1.11) shows that the subspaces of symmetric and antisymmetric combinations of sidebands are not coupled by the nonlinear medium. Nevertheless, these correlations were already observed in experiments [Barbosa 2013c], and their origin is found somewhere else in the OPO, as we will see in Sec. 3.3.

3.2 Parametric gain of the fields

After passing through the nonlinear medium, the modes in subspaces of $\mathcal{S}/\mathcal{A}$ combinations of sidebands will interact according to the Hamiltonian given by Eq.(3.1.10). Therefore, the equations describing the evolution of the operators during their propagation through the medium are given by

$$\frac{d\hat{a}^{(0)}_{s(a)}}{d\xi} = -\chi\Big[\alpha_{\omega_1}\hat{a}^{(2)}_{s(a)} + \alpha_{\omega_2}\hat{a}^{(1)}_{s(a)}\Big] \tag{3.2.1}$$

$$\frac{d\hat{a}^{(1)}_{s(a)}}{d\xi} = \chi\Big[\pm\,\alpha_{\omega_0}\hat{a}^{(2)\dagger}_{s(a)} + \alpha^{*}_{\omega_2}\hat{a}^{(0)}_{s(a)}\Big] \tag{3.2.2}$$

$$\frac{d\hat{a}^{(2)}_{s(a)}}{d\xi} = \chi\Big[\pm\,\alpha_{\omega_0}\hat{a}^{(1)\dagger}_{s(a)} + \alpha^{*}_{\omega_1}\hat{a}^{(0)}_{s(a)}\Big], \tag{3.2.3}$$

where ξ is the normalized time evolution given by $\xi = t/\tau$.

Defining $\vec{\mathbf{A}}_{s(a)} = (\hat{a}^{(0)}_{s(a)}\ \hat{a}^{(0)\dagger}_{s(a)}\ \hat{a}^{(1)}_{s(a)}\ \hat{a}^{(1)\dagger}_{s(a)}\ \hat{a}^{(2)}_{s(a)}\ \hat{a}^{(2)\dagger}_{s(a)})^{T}$, the set of differential equations given by Eqs. (3.2.1-3.2.3) and their Hermitian adjoints can be written as

$$\frac{d\vec{\mathbf{A}}_{s(a)}}{d\xi} = \mathbf{M}_{\chi s(a)}\vec{\mathbf{A}}_{s(a)}, \tag{3.2.4}$$

where

$$\mathbf{M}_{\chi s(a)} = \chi \begin{pmatrix} 0 & 0 & -\alpha_{\omega_2} & 0 & -\alpha_{\omega_1} & 0 \\ 0 & 0 & 0 & -\alpha^*_{\omega_2} & 0 & -\alpha^*_{\omega_1} \\ \alpha^*_{\omega_2} & 0 & 0 & 0 & 0 & \pm\alpha_{\omega_0} \\ 0 & \alpha_{\omega_2} & 0 & 0 & \pm\alpha^*_{\omega_0} & 0 \\ \alpha^*_{\omega_1} & 0 & 0 & \pm\alpha_{\omega_0} & 0 & 0 \\ 0 & \alpha_{\omega_1} & \pm\alpha^*_{\omega_0} & 0 & 0 & 0 \end{pmatrix}. \tag{3.2.5}$$

From Eq. (3.2.4) the field leaving the crystal can be written as

$$\vec{\mathbf{A}}_{s(a)}\Big|_{\xi=1} = \mathbf{G}_{s(a)}(\chi)\vec{\mathbf{A}}_{s(a)}\Big|_{\xi=0}, \tag{3.2.6}$$

where

$$\mathbf{G}_{s(a)}(\chi) = \exp\left(\int_0^1 d\xi\ \mathbf{M}_{\chi s(a)}\right). \tag{3.2.7}$$

The matrix $\mathbf{G}_{s(a)}(\chi)$ is defined as the *gain matrix of the medium*, and allows the evaluation of all $\hat{a}^{(n)}_{\omega_n\pm\Omega}$ and their Hermitian adjoints after passing through the crystal.

In the calculation of the evolution of the terms inside the cavity, it will be useful to play with all creation and annihilation operators of the involved sidebands in a vector form $\vec{\mathbf{A}} = (\hat{a}^{(0)}_{\omega_0+\Omega}\ \hat{a}^{(0)\dagger}_{\omega_0+\Omega}\ \cdots\ \hat{a}^{(0)}_{\omega_0-\Omega}\ \hat{a}^{(0)\dagger}_{\omega_0-\Omega}\ \cdots)^T$, related to vectors $\vec{\mathbf{A}}_{s(a)}$ as

$$\vec{\mathbf{A}} = \mathbf{\Lambda}\left(\vec{\mathbf{A}}_s, \vec{\mathbf{A}}_a\right)^T, \tag{3.2.8}$$

where the transformation matrix is of the form

$$\mathbf{\Lambda} = \mathbf{\Lambda}^{-1} = \frac{1}{\sqrt{2}}\begin{pmatrix} \mathbf{1}_{6\times6} & \mathbf{1}_{6\times6} \\ \mathbf{1}_{6\times6} & \text{-}\mathbf{1}_{6\times6} \end{pmatrix}, \tag{3.2.9}$$

where $\mathbf{1}_{6\times6}$ are identity matrices of order 6. Taking into account Eqs. (3.2.6) and (3.2.8), the transformation of the field operators that propagated through the medium is given by

$$\vec{\mathbf{A}}\Big|_{\xi=1} = \mathbf{G}(\chi)\vec{\mathbf{A}}\Big|_{\xi=0}, \tag{3.2.10}$$

where

$$\mathbf{G}(\chi) = \mathbf{\Lambda}\left(\mathbf{G}_s(\chi) \oplus \mathbf{G}_a(\chi)\right)\mathbf{\Lambda}. \tag{3.2.11}$$

The symbol $\oplus$ represents a direct sum, resulting in a block diagonal matrix.

Thanks to the bilinear form of the Hamiltonian in Eq. (3.1.8), we have a linear

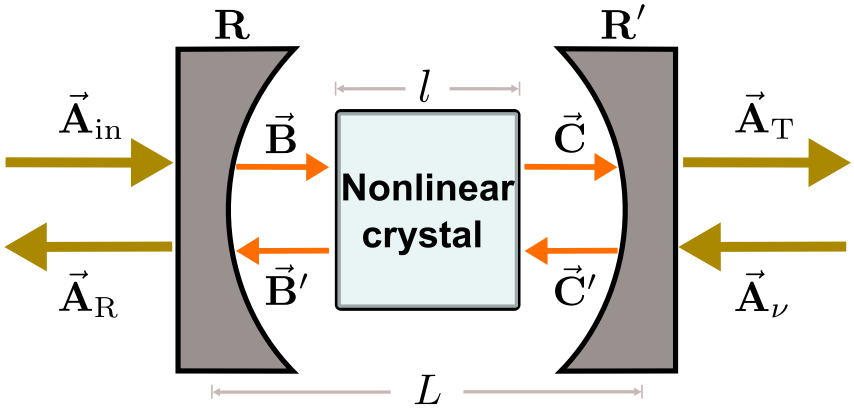

Figure 16: Basic configuration of OPO.

evolution of the coupling of different fields through the medium, that will contribute to the equations describing their evolution inside a cavity.

3.3 Physical effect of the optical cavity

It must be kept in mind that our goal is to theoretically model the evolution of the sideband modes of an OPO, consisting of a nonlinear crystal located in a Fabry-Perot cavity that we assume to have arbitrary losses for the fields involved, as shown in Fig. 16. In the same way as the cavity was modeled in subsection 2.3.1, the coupling mirror (left mirror in the figure) has reflection and transmission coefficients, r_n and t_n, for each carrier, and the end mirror (right mirror in the figure), with reflection coefficient r'_n and transmission coefficient t'_n, accounts for spurious losses (that may include absorption in the crystal or scattering on the optical interfaces). These coefficients can be conveniently described by loss parameters γ_n and γ'_n as

$$r_n = e^{-\gamma_n}, \qquad t_n = \left(1 - r_n^2\right)^{1/2}, \tag{3.3.1}$$

$$r'_n = e^{-\gamma'_n}, \qquad t'_n = \left(1 - r_n'^2\right)^{1/2}. \tag{3.3.2}$$

The total loss in a round trip can be directly evaluated from $\gamma_n^t = \gamma_n + \gamma'_n$. The formalism adopted here remains valid even in the open cavity regime, enabling the treatment in the limit where the cavity is completely open for one of the modes, as in the case of a doubly resonant OPO [de Andrade 2017].

The equations relating each field operator inside and outside the cavity (Fig. 16) are given by the beam splitter transformation

$$\vec{\mathbf{A}}_{\mathrm{R}} = \mathbf{R}\vec{\mathbf{A}}_{\mathrm{in}} + \mathbf{T}\vec{\mathbf{B}}', \qquad \vec{\mathbf{B}} = \mathbf{T}\vec{\mathbf{A}}_{\mathrm{in}} - \mathbf{R}\vec{\mathbf{B}}', \tag{3.3.3}$$

$$\vec{\mathbf{A}}_{\mathrm{T}} = \mathbf{R}'\vec{\mathbf{A}}_{\nu} + \mathbf{T}'\vec{\mathbf{C}}, \qquad \vec{\mathbf{C}}' = \mathbf{T}'\vec{\mathbf{A}}_{\nu} - \mathbf{R}'\vec{\mathbf{C}}, \tag{3.3.4}$$

with

$$\begin{aligned}
\mathbf{R} &= \mathrm{diag}\big(r_0\ r_0\ r_1\ r_1\ r_2\ r_2\ r_0\ r_0\cdots\big),\\
\mathbf{T} &= \mathrm{diag}\big(t_0\ t_0\ t_1\ t_1\ t_2\ t_2\ t_0\ t_0\cdots\big),\\
\mathbf{R}' &= \mathrm{diag}\big(r'_0\ r'_0\ r'_1\ r'_1\ r'_2\ r'_2\ r'_0\ r'_0\cdots\big),\\
\mathbf{T}' &= \mathrm{diag}\big(t'_0\ t'_0\ t'_1\ t'_1\ t'_2\ t'_2\ t'_0\ t'_0\cdots\big),
\end{aligned} \tag{3.3.5}$$

keeping the vector ordering for the field operators we used in the previous section. The fields described by $\vec{\mathbf{A}}_{\mathrm{in}}$ enters the cavity through the coupling mirror, while $\vec{\mathbf{A}}_{\nu}$ models the fields associated with vacuum modes coupled through spurious losses. Each field $\hat{a}^{(n)}_{\omega_n\pm\Omega}$ will be transformed by the gain inside the crystal as described by Eq. (3.2.10). Besides that, their phases will evolve during propagation along the cavity. Under perfect phase matching conditions [Debuisschert 1993], if the refractive index for the fields are close enough, we may consider that the evolution of the phase commutes with the gain. Therefore the relation between the propagating fields on each side of the cavity will be given by

$$\vec{\mathbf{C}} = e^{-i\boldsymbol{\varphi}}\mathbf{G}(\chi)\vec{\mathbf{B}}, \qquad \vec{\mathbf{B}}' = e^{-i\boldsymbol{\varphi}}\mathbf{G}(\chi)\vec{\mathbf{C}}'. \tag{3.3.6}$$

The phase vector

$$\boldsymbol{\varphi} = \boldsymbol{\varphi}(\Omega)\oplus\boldsymbol{\varphi}(-\Omega),\ \text{with}\ \boldsymbol{\varphi}(\Omega) = \mathrm{diag}\big(\varphi^{(0)}_{\Omega}, -\varphi^{(0)}_{\Omega}\varphi^{(1)}_{\Omega}, -\varphi^{(1)}_{\Omega}, \varphi^{(2)}_{\Omega}-\varphi^{(2)}_{\Omega}\big), \tag{3.3.7}$$

gives a different contribution for each sideband depending on the frequency shift Ω and on the carrier frequency ω_n

$$\boldsymbol{\varphi}^{(n)}_{\Omega} = \frac{\omega_n+\Omega}{2\,\mathrm{FSR}_n}, \tag{3.3.8}$$

where $\mathrm{FSR}_n = c/2L^{(n)}_{\mathrm{op}}$ is the free spectral range for the mode n, with $L^{(n)}_{\mathrm{op}} = L + l(\mathtt{n}_n - 1)$ being the effective optical length between the cavity mirrors, depending on the crystal refractive index $\mathtt{n}_n$ and on the speed of light c. Evidently the effective phase contribution will depend on the detuning between the carrier and the nearest cavity mode ω^c_n, an integer multiple of $2\pi\mathrm{FSR}_n$, given by $\Delta_n = \omega_n - \omega^c_n$.

An important point related to the evolution of the sidebands should be noticed. Each operator will undergo a different phase evolution, depending on their frequency. That will mix symmetric and antisymmetric modes, even for null carrier detuning, since upper and lower sidebands will, in this case, undergo opposite phase evolutions. This is the cause for the correlations between symmetric and antissymetric modes observed in [Barbosa 2013c].

Combining beam splitter transformation, phase evolution and gain, expressed in Eqs. (3.3.3)–(3.3.6) we can derive a linear transformation for the reflected modes, coupled to the incident modes on the OPO, as

$$\vec{\mathbf{A}}_{\mathrm{R}} = \mathbf{R}_{\chi}\vec{\mathbf{A}}_{\mathrm{in}} + \mathbf{T}'_{\chi}\vec{\mathbf{A}}_{\nu}, \tag{3.3.9}$$

where

$$\mathbf{R}_{\chi} = \mathbf{R} - \mathbf{T}e^{-i\boldsymbol{\varphi}}\mathbf{G}(\chi)\mathbf{R}'e^{-i\boldsymbol{\varphi}}\mathbf{G}(\chi)\mathbf{D}(\chi)\mathbf{T}, \tag{3.3.10}$$

$$\mathbf{T}'_{\chi} = \mathbf{T}e^{-i\boldsymbol{\varphi}}\mathbf{G}(\chi)\left[\mathbf{I} + \mathbf{R}'e^{-i\boldsymbol{\varphi}}\mathbf{G}(\chi)\mathbf{D}(\chi)\mathbf{R}e^{-i\boldsymbol{\varphi}}\mathbf{G}(\chi)\right]\mathbf{T}', \tag{3.3.11}$$

and

$$\mathbf{D}(\chi) = \left(\mathbf{1} - \mathbf{R}e^{-i\boldsymbol{\varphi}}\mathbf{G}(\chi)\mathbf{R}'e^{-i\boldsymbol{\varphi}}\mathbf{G}(\chi)\right)^{-1}. \tag{3.3.12}$$

We should notice that the conversion matrix given by Eq. (3.2.9), relating individual modes to symmetric/antisymmetric combinations, commutes with the reflection and transmission matrices given by Eq. (3.3.5), but not with the phase evolution matrix. It is consistent with the fact that the coupling of symmetric and antisymmetric modes comes from the opposite phase evolution for the sidebands. Another interesting point of the formalism here adopted is that it allows the evaluation of the complete covariance matrix for the sideband modes, in an approach valid for lossy cavities beyond the narrowband regime employed in ref. [Collett 1984]. In the extreme limit, it can be used to study the transformation of fields in doubly resonant cavities, even for the mode undergoing a single pass through the nonlinear medium.

3.4 Hexapartite quantum state: covariance matrix in the eigenbasis of quadrature operators

Consistent with the description used in [Barbosa 2013c], we can evaluate the covariance matrix for the field quadratures $\hat{p}_{\omega}^{(n)}$ and $\hat{q}_{\omega}^{(n)}$ related to photon annihilation $\hat{a}_{\omega}^{(n)}$ operator as $\hat{a}_{\omega}^{(n)} = (\hat{p}_{\omega}^{(n)} + i\hat{q}_{\omega}^{(n)})/2$ and satisfying the commutation relation $[\hat{p}_{\omega}^{(n)}, \hat{q}_{\omega'}^{(n)}] = 2i\delta(\omega - \omega')$. The relevant quadrature operators can be ordered in a column vector $\vec{\mathbf{X}} = (\hat{p}_{\omega}^{(0)}\ \hat{q}_{\omega}^{(0)}\ \cdots\ \hat{p}_{\omega'}^{(n)}\ \hat{q}_{\omega'}^{(n)}\cdots)^{T}$, that is directly related to the vector of field operators by $\vec{\mathbf{X}} = \mathbf{N}\vec{\mathbf{A}}$, where $\mathbf{N}$ is the transformation matrix between these vectors.

Second order momenta of the field operators are all contained in the symmetrized covariance matrix, evaluated over the quantum state of the system as

$$\mathbf{V} = \frac{1}{2}\left(\langle\vec{\mathbf{X}}\cdot\vec{\mathbf{X}}^{T}\rangle + \langle\vec{\mathbf{X}}\cdot\vec{\mathbf{X}}^{T}\rangle^{T}\right). \tag{3.4.1}$$

Diagonal elements of $\mathbf{V}$ represent variances of single-mode quadrature operators, denoted as, e.g., $\Delta^2\hat{p}_\omega^{(n)} \equiv \langle \hat{p}_\omega^{(n)}\hat{p}_\omega^{(n)}\rangle$. Off-diagonal elements are correlations between different quadratures operators, such as in, e.g., $C(\hat{p}_\omega^{(n)}\hat{p}_{\omega'}^{(m)}) \equiv (\langle \hat{p}_\omega^{(n)}\hat{p}_{\omega'}^{(m)}\rangle + \langle \hat{p}_{\omega'}^{(m)}\hat{p}_\omega^{(n)}\rangle)/2$.

The basis transformation given by matrix $\mathbf{N}$ applied to Eq. (3.3.9) results in quadrature operators $\vec{\mathbf{X}}_{\mathrm{R}} = \widetilde{\mathbf{R}}_\chi \vec{\mathbf{X}}_{\mathrm{in}} + \widetilde{\mathbf{T}}'_\chi \vec{\mathbf{X}}_\nu$, where $\widetilde{\mathbf{R}}_\chi = \mathbf{N}\mathbf{R}_\chi\mathbf{N}^{-1}$, $\widetilde{\mathbf{T}}'_\chi = \mathbf{N}\mathbf{T}'_\chi\mathbf{N}^{-1}$. Thus, the evaluation of the covariance matrix for the output fields results in

$$\mathbf{V}_{\mathrm{R}} = \widetilde{\mathbf{R}}_\chi \mathbf{V}_{\mathrm{in}} \widetilde{\mathbf{R}}_\chi^T + \widetilde{\mathbf{T}}'_\chi \mathbf{V}_\nu \widetilde{\mathbf{T}}'^T_\chi , \tag{3.4.2}$$

where $\mathbf{V}_{\mathrm{in}}$ is the input field covariance matrix and $\mathbf{V}_\nu$ is the covariance matrix of the field entering through the cavity loss channels. For losses coupling the cavity to vacuum modes we have $\mathbf{V}_\nu = \mathbf{1}$. The identity matrix $\mathbf{1}$ is associated with the standard quantum level of noise (known in the literature as *shot noise*), characteristic of coherent states (including vacuum).

The covariance matrix in the basis of $\mathcal{S}/\mathcal{A}$ combinations of sidebands will have the same form described in ref. [Barbosa 2013c]

$$\mathbf{V}_{\mathrm{R}(s/a)} = \begin{pmatrix} \mathbf{V}_s & \mathbf{C}_{s/a} \\ (\mathbf{C}_{s/a})^T & \mathbf{V}_a \end{pmatrix}. \tag{3.4.3}$$

It is important to notice that the elements in the covariance matrices $\mathbf{V}_s$ and $\mathbf{V}_a$ are related by a $\pi/2$ rotation on the quadrature phase space, changing $\hat{p}_s \to \hat{q}_a$ and $\hat{q}_s \to -\hat{p}_a$ in covariance terms (e.g., $C(\hat{p}_s^{(n)}\hat{q}_s^{(m)}) = -C(\hat{q}_a^{(n)}\hat{p}_a^{(m)})$, $\Delta^2\hat{p}_s^{(n)} = \Delta^2\hat{q}_a^{(n)}$,...). Therefore, the modeling described here is equivalent to the semiclassical approach often used in evaluation of the noise spectra with the help of Langevin equations [Collett 1984, Walls 2008, César 2009, Barbosa 2013c], and both methods can be used to obtain the same amount of information about the 2n modes of sidebands for n modes of carriers. However, it is important to clarify that the method developed here is explicit in presenting the physical origin of the correlations between symmetric and antisymmetric modes, something that was elusive in the semiclassical model. As demonstrated in Secs. (3.1) and (3.3), these correlations are not generated only by the cavity, or by the squeezing generating term in Eq. (3.1.11), that is the only remaining term for operation below the oscillation threshold. It is their combination with the beam splitting term, associated with signal and idler mean fields, that will lead to these correlations.

Considering the particular case where the input is also a coherent state ($\mathbf{V}_{\mathrm{in}} = \mathbf{1}$), for exact resonance of the carriers ($\Delta_n = 0$), we have

$$\mathbf{V}_s = \begin{array}{c} \\ \hat{p}_s^{(0)} \\ \hat{q}_s^{(0)} \\ \hat{p}_s^{(1)} \\ \hat{q}_s^{(1)} \\ \hat{p}_s^{(2)} \\ \hat{q}_s^{(2)} \end{array} \begin{array}{c} \begin{array}{cccccc} \hat{p}_s^{(0)} & \hat{q}_s^{(0)} & \hat{p}_s^{(1)} & \hat{q}_s^{(1)} & \hat{p}_s^{(2)} & \hat{q}_s^{(2)} \end{array} \\ \begin{pmatrix} \rho^{(0)} & 0 & \mu^{(01)} & 0 & \mu^{(02)} & 0 \\ 0 & \beta^{(0)} & 0 & \nu^{(01)} & 0 & \nu^{(02)} \\ \mu^{(01)} & 0 & \rho^{(1)} & 0 & \zeta^{(12)} & 0 \\ 0 & \nu^{(01)} & 0 & \beta^{(1)} & 0 & \epsilon^{(12)} \\ \mu^{(02)} & 0 & \zeta^{(12)} & 0 & \rho^{(2)} & 0 \\ 0 & \nu^{(02)} & 0 & \epsilon^{(12)} & 0 & \beta^{(2)} \end{pmatrix} \end{array}, \tag{3.4.4}$$

with 12 independent terms and

$$\mathbf{C}_{s/a} = \begin{array}{c} \\ \hat{p}_s^{(0)} \\ \hat{q}_s^{(0)} \\ \hat{p}_s^{(1)} \\ \hat{q}_s^{(1)} \\ \hat{p}_s^{(2)} \\ \hat{q}_s^{(2)} \end{array} \begin{array}{c} \begin{array}{cccccc} \hat{p}_a^{(0)} & \hat{q}_a^{(0)} & \hat{p}_a^{(1)} & \hat{q}_a^{(1)} & \hat{p}_a^{(2)} & \hat{q}_a^{(2)} \end{array} \\ \begin{pmatrix} 0 & 0 & 0 & -\kappa^{(01)} & 0 & -\kappa^{(02)} \\ 0 & 0 & \lambda^{(01)} & 0 & \lambda^{(02)} & 0 \\ 0 & \kappa^{(01)} & 0 & 0 & 0 & -\varrho^{(12)} \\ -\lambda^{(01)} & 0 & 0 & 0 & \eta^{(12)} & 0 \\ 0 & \kappa^{(02)} & 0 & \varrho^{(12)} & 0 & 0 \\ -\lambda^{(02)} & 0 & -\eta^{(12)} & 0 & 0 & 0 \end{pmatrix} \end{array}, \tag{3.4.5}$$

with 6 independent terms.

Evaluation of the covariance matrix depends on the value of the mean fields, as can be seen in Eq.(3.2.5). As discussed in Sec. 2.3.1, the contributions to the gain matrix can be explicitly scaled to the oscillation threshold $|\alpha_{\omega_0}^{\text{in}}|^2_{\text{th}}$ as [Eqs. (2.3.12) and (2.3.13)]

$$\chi^2 \mid \alpha_{\omega_0} \mid^2 = \frac{(1-e^{-2\gamma_0})}{(1-e^{-\gamma^t{}_0})^2}\, \chi^2 \mid \alpha_{\omega_0}^{\text{in}} \mid^2_{\text{th},} \tag{3.4.6}$$

$$\chi^2 \mid \alpha_{\omega_j} \mid^2 = \frac{e^{2\gamma^t{}_0}\,(1-e^{-2\gamma_0})\,(\sqrt{\sigma}-1)}{(e^{\gamma^t{}_0}-1)\,(e^{\gamma^t{}_j}-1)}\, \chi^2 \mid \alpha_{\omega_0}^{\text{in}} \mid^2_{\text{th}} \quad \text{with,} \quad j=1,2, \tag{3.4.7}$$

where the normalized pump power is given by $\sigma = |\alpha_{\omega_0}^{\text{in}}|^2/|\alpha_{\omega_0}^{\text{in}}|^2_{\text{th}}$. Moreover, [Eq. (2.3.11)]

$$\chi^2 |\, \alpha_{\omega_0}^{\text{in}} \mid^2_{\text{th}} = \frac{\left(1-e^{-\gamma^t{}_0}\right)^2 \left(e^{\gamma^t{}_1}-1\right)\left(e^{\gamma^t{}_2}-1\right)}{4\,(1-e^{-2\gamma_0})}, \tag{3.4.8}$$

implies that all the mean values can be related only to the cavity coupling terms and the normalized pump power. Note that we have retained here the consideration that evolution of the mean field amplitude inside the crystal is negligible, as discussed in Sec. 2.3.1. Further development can be done if we consider that these fields vary along the

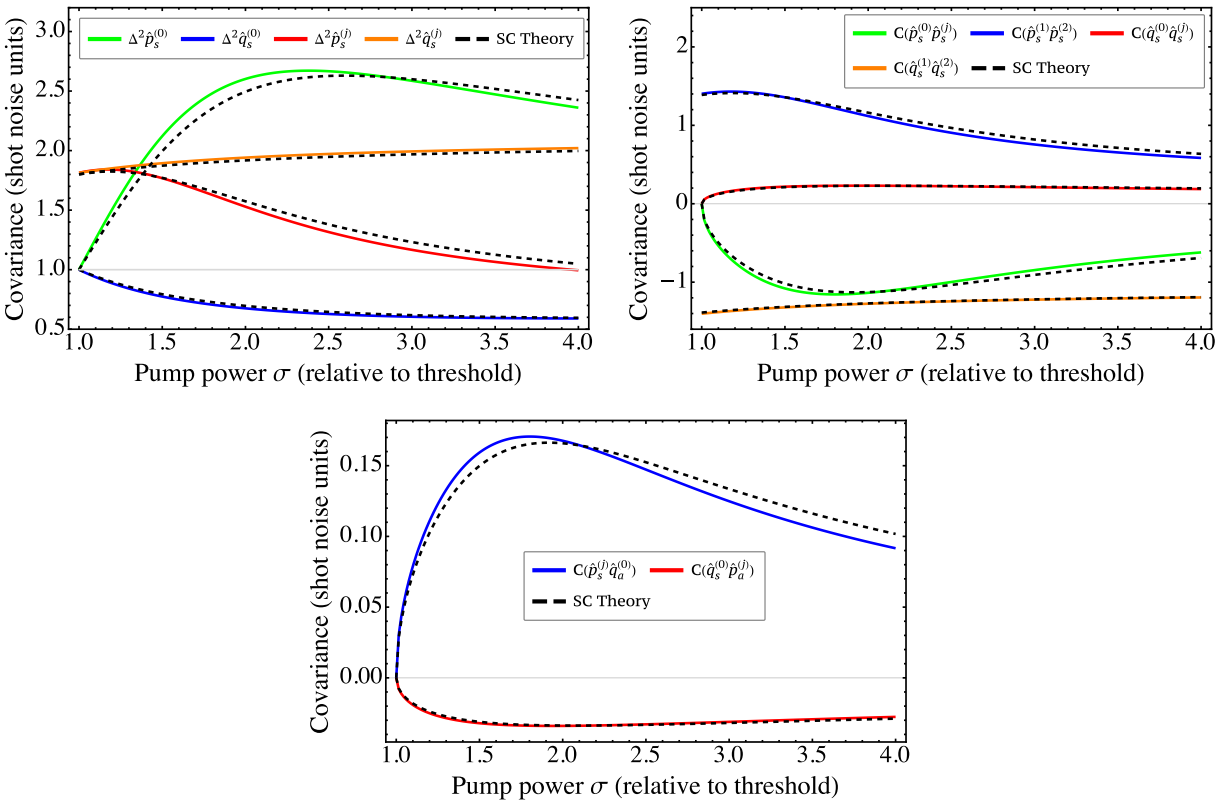

Figure 17: Covariance of the amplitude and phase quadratures of the three fields coming from the OPO, Eqs. (3.4.4) and (3.4.5), as a function of the normalized pump power. All quantities are in units of *shot noise*, i.e. the standard quantum level of noise, characteristic of coherent states (including vacuum).We employ in our numerical results the typical experimental values $\gamma_0 = 0.178$ and $\gamma = 0.020$ for the OPO cavity mirrors transmissions, analysis frequency $\Omega/2\pi = 21$ MHz, and free spectral range FSR= 4.3 GHz. For losses channels we use $\gamma_0^t = 0.209$ and $\gamma^t = 0.025$. We assume equal mirror transmissions for signal and idler beams, i.e., $\gamma_1 = \gamma_2 \equiv \gamma$ and $\gamma_1^t = \gamma_2^t \equiv \gamma^t$. The dashed lines are obtained from the semiclassical model presented in [César 2009].

crystal [de Andrade 2017]. Nevertheless, in the integration in Eq. (3.2.7), we see that their evolution will not affect the linearity of the solution regarding the mode operators, and an effective contribution can be evaluated to obtain a precise description of the resulting covariances.

The behavior of all elements from the Eqs. (3.4.4) and (3.4.5) as functions of normalized pump power σ are presented in Fig. 17. For comparison, the same terms were also plotted using the semiclassical theory presented in [César 2009] (dashed lines). We can see that there is an excellent agreement between our theory and the semiclassical theory. The discrepancies are due to the fact that the semiclassical theory is only valid for closed cavities ($\gamma_n, \gamma_n^t \ll 1$) while our theory does not have any kind of approximation about these quantities, so we can conclude that a consistent and complete OPO theory has been developed.

While this treatment could account for the OPO spectra above the threshold, it doesn't account for extra noise sources, as the phonon-photon coupling in the crystal [César 2009]. Its effect can be included in the interaction Hamiltonian, as we will see next. This extra

phonon noise may also introduce correlations between $\hat{p}$ and $\hat{q}$ quadratures within $\mathbf{V}_{s(a)}$ matrices, as well as correlations in the $\mathbf{C}_{s/a}$ matrix, that can be also found in the case of non-zero cavity detunings.

3.5 Physical effect of phonons in the nonlinear crystal in the quantum noise of light

In many experiments with above-threshold OPO's, an extra phase noise appears on the optical fields which is caused by the scattering of light by thermal phonons within the crystal and which considerably modifies the quantum state of the system. A detailed semi-classical analysis of this effect was realized in [César 2009]. In this section we are going to establish a quantum model for this excess phase noise in order to have a consistent and complete quantum description of an OPO operating above threshold.

3.5.1 *Complete interaction Hamiltonian*

Photons that circulate inside the optical cavity of an OPO may eventually exert a small radiation pressure on the crystal, leading to local density fluctuations associated with acoustic phonons. On the other hand, fluctuations of the refractive index, of optical or mechanical origin, will result in small phase fluctuations, leading to Stokes and Brillouin light scattering [Boyd 1992] with frequency shifts in the scattered light. This process can also be seen as a random detuning of the optical cavity, since it modifies its optical length $L_{\mathrm{op}}^{(n)}$.

In the present case, we will be interested in the fraction of the scattering that is coupled to the cavity modes, with small shifts in the frequency (within the cavity bandwidth). The Hamiltonian that correctly models this type of photon-phonon interaction is known as optomechanical Hamiltonian[1] [Law 1995], which for this case is given by

$$\hat{H}_g = \sum_{n=0}^{2} \sum_{j=1}^{3} \hat{H}_g^{(n,j)}, \tag{3.5.1}$$

where

$$\hat{H}_g^{(n,j)} = -\hbar g_{nj} \hat{a}^{(n)\dagger}(t) \hat{a}^{(n)}(t) \left(\hat{d}^{(j)}(t) + \hat{d}^{(j)\dagger}(t) \right), \tag{3.5.2}$$

is the optomechanical Hamiltonian for the optical mode $\hat{a}^{(n)}$ coupled to the mechanical vibration mode $\hat{d}^{(j)}$. We may consider three possible modes of oscillation: one longitudi-

[1] A rigorous derivation of this Hamiltonian (for the specific case of a Fabry-Perot resonator with a moveable end mirror) was given in [Law 1995]. This derivation keeps all the resonant modes of the optical cavity, and shows how in principle one also obtains interaction terms where the mechanical resonator can mediate scattering between different optical modes, and also terms corresponding to the dynamical Casimir effect, where, e.g. , destruction of a phonon can result in the creation of a pair of photons. Such additional terms are of negligible importance in the standard situation where the mechanical frequency is much smaller than all optical frequency scales.

nal, with propagation parallel to the wave vector of the field, and two transversal modes. The optomechanical coupling strength g_{nj} is expressed as a frequency. It quantifies the interaction between a single phonon and a single photon. The Hamiltonian in Eq. (3.5.2) reveals that the interaction of a vibrating non-linear crystal with the radiation field is fundamentally a nonlinear process, involving three operators (three-wave mixing), coupling photon number operators to the creation and annihilation of phonons.

Following a procedure similar to that done in Sec. 3.1, we can write the bosonic operator $d^{(j)}$ with the help of the Fourier transform as

$$\hat{d}^{(j)}(t) = \int_0^\infty d\Omega_m e^{-i\Omega_m t} \hat{d}^{(j)}_{\Omega_m}, \tag{3.5.3}$$

with $\hat{d}^{(j)}_{\Omega_m}$ the phonon annihilation operator in the mechanical mode of frequency Ω_m. The Hamiltonian in Eq. (3.5.1) can also be described by a sum of contributing terms over many different frequencies as $\hat{H}_g = \int_\epsilon^\infty d\Omega \hat{H}_g(\Omega)$, where

$$\hat{H}_g(\Omega) = \sum_{n=0}^{2}\sum_{j=1}^{3} -\hbar g_{nj}\left[\alpha_{\omega_n}\left(\hat{a}^{(n)\dagger}_{\omega_n-\Omega}\hat{d}^{(j)\dagger}_{\Omega} + \hat{a}^{(n)\dagger}_{\omega_n+\Omega}\hat{d}^{(j)}_{\Omega}\right) + \text{h.c.}\right]. \tag{3.5.4}$$

Note that, satisfying energy conservation, different processes may occur from the annihilation of a photon of the carrier, described in the linearization by the field amplitude α_{ω_n}. Either we may have the production of a photon in the lower sideband and the production of a phonon from the annihilation of a carrier photon, or the production of a photon in the upper sideband with the annihilation of a phonon. The reverse processes are described by the Hermitian conjugate terms.

The complete Hamiltonian of the system, which includes the parametric down conversion and the photon-phonon interaction, would be given by

$$\hat{H}(\Omega) \;=\; \hat{H}_\chi(\Omega) + \hat{H}_g(\Omega), \tag{3.5.5}$$

where $\hat{H}_\chi(\Omega)$ and $\hat{H}_g(\Omega)$ are given by the Eqs. (3.1.8) and (3.5.4), respectively. Now a complete evaluation of the contribution of both parametric down conversion and Brillouin scattering to the OPO dynamics can be performed.

3.5.2 *Parametric gain of the fields*

The evolution of the system should now include the modes of the phonon bath. Let be $\vec{\mathbb{A}} = \left(\vec{\mathbf{A}}, \vec{\mathbf{D}}\right)^T$, where the field operator vector $\vec{\mathbf{A}}$ was defined in the Sec. 3.2 and $\vec{\mathbf{D}} = (\hat{d}^{(1)}_\Omega\ \hat{d}^{(1)\dagger}_\Omega\ \hat{d}^{(2)}_\Omega\ \hat{d}^{(2)\dagger}_\Omega\ \hat{d}^{(3)}_\Omega\ \hat{d}^{(3)\dagger}_\Omega)^T$ lists the bosonic operators on the phononic reservoirs. Therefore the set of differential equations describing the dynamics of operators can be

written in compact form as follows:

$$\frac{d\vec{\mathbb{A}}}{d\xi} = \mathbb{M}_{(\chi,g)}\vec{\mathbb{A}}, \tag{3.5.6}$$

where

$$\mathbb{M}_{(\chi,g)} = \begin{pmatrix} \mathbf{M}_\chi & i\mathbf{J}_g \\ i\mathbf{K}_g & \mathbf{0}_{6\times 6} \end{pmatrix}. \tag{3.5.7}$$

Here $\mathbf{M}_\chi = \mathbf{\Lambda}(\mathbf{M}_{\chi s} \oplus \mathbf{M}_{\chi a})\mathbf{\Lambda}^{-1}$ and

$$\mathbf{J}_g = \begin{pmatrix} \mathbf{L} \\ \mathbf{L}^{'} \end{pmatrix}, \qquad \mathbf{K}_g = \begin{pmatrix} \mathbf{L}^\dagger & -\mathbf{L}^{'\dagger} \end{pmatrix}, \tag{3.5.8}$$

where

$$\mathbf{L}_{nj} = g_{nj}\begin{pmatrix} \alpha_{\omega_n} & 0 \\ 0 & -\alpha^*_{\omega_n} \end{pmatrix}, \tag{3.5.9}$$

$$\mathbf{L}^{'}_{nj} = g_{nj}\begin{pmatrix} 0 & \alpha_{\omega_n} \\ -\alpha^*_{\omega_n} & 0 \end{pmatrix}, \tag{3.5.10}$$

are the elements matrix of the matrices $\mathbf{L}$ and $\mathbf{L}^{'}$, respectively. In Eq. (3.5.8) the "dagger" denotes conjugate transpose of the matrix.

The solution of Eq. (3.5.6) is given by

$$\vec{\mathbb{A}}\Big|_{\xi=1} = \mathbb{G}(\chi, g)\vec{\mathbb{A}}\Big|_{\xi=0}, \tag{3.5.11}$$

where

$$\mathbb{G}(\chi, g) = \exp\left(\int_0^1 d\xi\ \mathbb{M}_{(\chi,g)}\right). \tag{3.5.12}$$

3.5.3 *Modeling the optical cavity*

Following a procedure similar to that done in Sec. 3.3, we get similar expressions for the output fields of the cavity. Specifically,

$$\vec{\mathbb{A}}_{\mathrm{R}} = \mathbb{R}_{(\chi,g)}\vec{\mathbb{A}}_{\mathrm{in}} + \mathbb{T}'_{(\chi,g)}\vec{\mathbb{A}}_{\nu}. \tag{3.5.13}$$

The expressions for the matrices $\mathbb{R}_{(\chi,g)}$ and $\mathbb{T}'_{(\chi,g)}$ are similar to those given in Eqs. (3.3.10) and (3.3.11) but with the following modifications to account for the phonon operators.

$$\begin{aligned}
\boldsymbol{\varphi} &\to \Psi = (\boldsymbol{\varphi} \oplus \mathbf{0}_{6\times 6})\,, \\
\mathbf{R} &\to \mathbb{R} = (\mathbf{R} \oplus \mathbf{0}_{6\times 6}), \\
\mathbf{T} &\to \mathbb{T} = (\mathbf{T} \oplus \mathbf{1}_{6\times 6}), \\
\mathbf{R}' &\to \mathbb{R}' = (\mathbf{R}' \oplus \mathbf{0}_{6\times 6}), \\
\mathbf{T}' &\to \mathbb{T}' = (\mathbf{T}' \oplus \mathbf{1}_{6\times 6}).
\end{aligned}$$

3.5.4 *Solution for the Gaussian quantum state*

In analogy to Eq. (3.4.2), the covariance matrix for all fields (optical and phononic) is

$$\mathbb{V}_{\mathrm{R}} = \widetilde{\mathbb{R}}_{(\chi,g)} \mathbb{V}_{\mathrm{in}} \widetilde{\mathbb{R}}^{T}_{(\chi,g)} + \widetilde{\mathbb{T}}'_{(\chi,g)} \mathbb{V}_{\nu} \widetilde{\mathbb{T}}'^{T}_{(\chi,g)}. \tag{3.5.14}$$

Considering the case where the field inputs are in a vacuum state, and the phonon reservoir is in a thermal state, $\mathbf{V}_{\mathrm{th}} = (1 + 2\bar{n}_{\mathrm{th}})\mathbf{1}_{6\times 6}$, we have

$$\mathbb{V}_{in} = \mathbb{V}_{\nu} = (\mathbf{1}_{12\times 12} \oplus \mathbf{V}_{\mathrm{th}})\,, \tag{3.5.15}$$

considering here that the three phonon modes of the reservoir have the same temperature and the same average number of phonons $\bar{n}_{\mathrm{th}}$.

The resulting covariance matrix will be given by

$$\mathbf{V}_s = \begin{array}{c} \\ \hat{p}_s^{(0)} \\ \hat{q}_s^{(0)} \\ \hat{p}_s^{(1)} \\ \hat{q}_s^{(1)} \\ \hat{p}_s^{(2)} \\ \hat{q}_s^{(2)} \end{array} \begin{array}{c} \begin{array}{cccccc} \hat{p}_s^{(0)} & \hat{q}_s^{(0)} & \hat{p}_s^{(1)} & \hat{q}_s^{(1)} & \hat{p}_s^{(2)} & \hat{q}_s^{(2)} \end{array} \\ \begin{pmatrix} \rho^{(0)} & e_1 & \mu^{(01)} & e_2 & \mu^{(02)} & e_3 \\ e_1 & \beta^{(0)} & e_4 & \nu^{(01)} & e_5 & \nu^{(02)} \\ \mu^{(01)} & e_4 & \rho^{(1)} & e_6 & \zeta^{(12)} & e_7 \\ e_2 & \nu^{(01)} & e_6 & \beta^{(1)} & e_8 & \epsilon^{(12)} \\ \mu^{(02)} & e_5 & \zeta^{(12)} & e_8 & \rho^{(2)} & e_9 \\ e_3 & \nu^{(02)} & e_7 & \epsilon^{(12)} & e_9 & \beta^{(2)} \end{pmatrix} \end{array}, \tag{3.5.16}$$

and

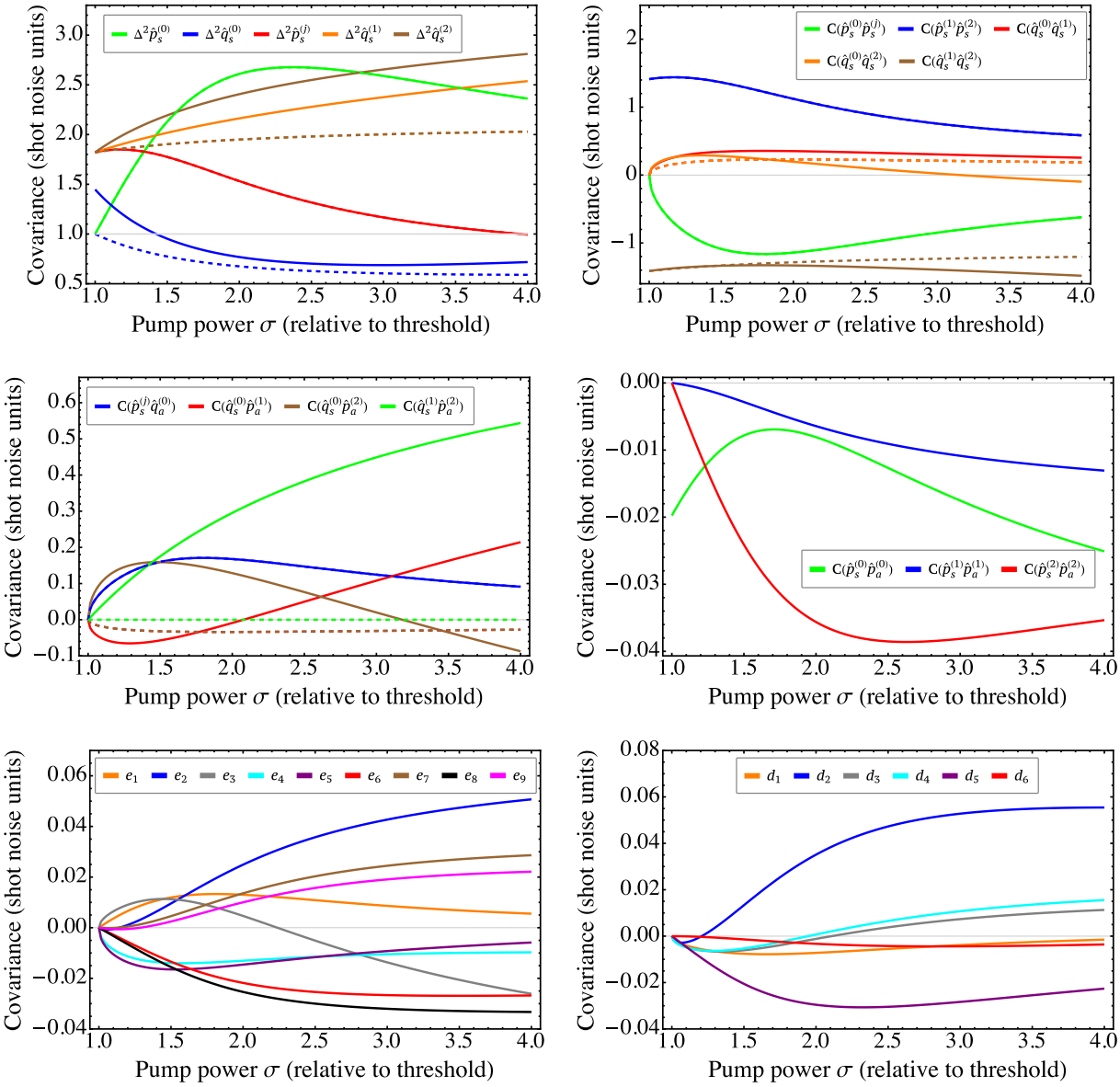

Figure 18: Covariance of the amplitude and phase quadratures of the three fields coming from the OPO, Eqs. (3.5.16) and (3.5.17), as a function of the normalized pump power. We employ in our numerical results arbitrary values for optomechanical couplings: $g_{01} = g_{02} = g_{03} = 7.0$ mHz, $g_{11} = g_{12} = g_{13} = 0.5$ mHz, $g_{21} = 1.0$ mHz and $g_{22} = g_{23} = 3.0$ mHz. Thermal phonon density was arbitrarily set to $\bar{n}_{\rm th}$=10. The dashed lines are the results we would expect in the absence of phonons noise (continuous lines in Fig. 17).

$$\mathbf{C}_{s/a} = \begin{array}{c} \\ \hat{p}_s^{(0)} \\ \hat{q}_s^{(0)} \\ \hat{p}_s^{(1)} \\ \hat{q}_s^{(1)} \\ \hat{p}_s^{(2)} \\ \hat{q}_s^{(2)} \end{array} \begin{array}{c} \begin{array}{cccccc} \hat{p}_a^{(0)} & \hat{q}_a^{(0)} & \hat{p}_a^{(1)} & \hat{q}_a^{(1)} & \hat{p}_a^{(2)} & \hat{q}_a^{(2)} \end{array} \\ \begin{pmatrix} \delta^{(0)} & 0 & h_1 & -\kappa^{(01)} & h_2 & -\kappa^{(02)} \\ 0 & \delta^{(0)} & \lambda^{(01)} & h_3 & \lambda^{(02)} & h_4 \\ h_3 & \kappa^{(01)} & \delta^{(1)} & 0 & h_5 & -\varrho^{(12)} \\ -\lambda^{(01)} & h_1 & 0 & \delta^{(1)} & \eta^{(12)} & h_6 \\ h_4 & \kappa^{(02)} & h_6 & \varrho^{(12)} & \delta^{(2)} & 0 \\ -\lambda^{(02)} & h_2 & -\eta^{(12)} & h_5 & 0 & \delta^{(2)} \end{pmatrix} \end{array} . \tag{3.5.17}$$

A direct comparison with matrices in Eqs. (3.4.4) and (3.4.5) shows many additional features coming from this added thermal reservoir. It is curious that even in the absence of phonons in the reservoir, those terms should yet appear due to the photon-phonon coupling of the zero-temperature fluctuations. Nevertheless, these terms would be small in this case, and would not affect significantly the covariance, even though the resulting state of the field is no longer pure due to the coupling to extra modes of the crystal.

The behavior of all elements from the Eqs. (3.5.16) and (3.5.17) as functions of normalized pump power σ are presented in Fig. 18 for the same parameters used in Fig. 17. We can see that only terms that depend on quadratures of amplitude, in the symmetric description, are unaffected by the inclusion of phonons. This behavior is expected according to the semiclassical theory presented in [César 2009]. In addition, we note that phonons can considerably modify the quantum state (covariance matrix), so it is necessary to take this effect into account to completely characterize the state of the OPO.

3.6 Experimental results

In this section we will use experimental data found by the research group led jointly by professors Marcelo Martinelli and Paulo Nussenzveig of the University of São Paulo in Brazil, in order to compare with the predictions of our theoretical model for a triply resonant OPO operating above threshold. The specific details of the experiment together with the measurement techniques used are very well described in [Barbosa 2013c, Coelho 2013, Barbosa 2013a] and therefore, in what follows, we will only describe very briefly such aspects in order to establish the theory-experiment connection. It should be noted that this research group has more than 15 years of experience in working with OPOs and that among its most relevant results we can highlight the generation of entanglement between signal and idler beams with different wavelengths [Villar 2005], the theoretical demonstration of tripartite entanglement [Villar 2006], measures of correlation between the twin beams and the reflected pump beam [Cassemiro 2007], characterization of the spurious noise introduced by the phonons in the crystal lattice of the non-linear crystal [César 2009], the experimental verification of tripartite entanglement [Coelho 2009] and the characterization of the dynamics of entanglement as a function of the losses [Barbosa 2010].

3.6.1 *Reconstruction of the hexapartite quantum state*

The experimental system is a triply resonant OPO operating above threshold, and the setup is depicted in Fig. 19. The OPO cavity is pumped by the second harmonic of a doubled Nd:YAG laser, filtered with a mode cleaning cavity to ensure that pump fluctuations are reduced to the standard quantum level in amplitude and phase for frequencies above 20 MHz. The filtered pump beam is then injected in the OPO, with adjustable power,

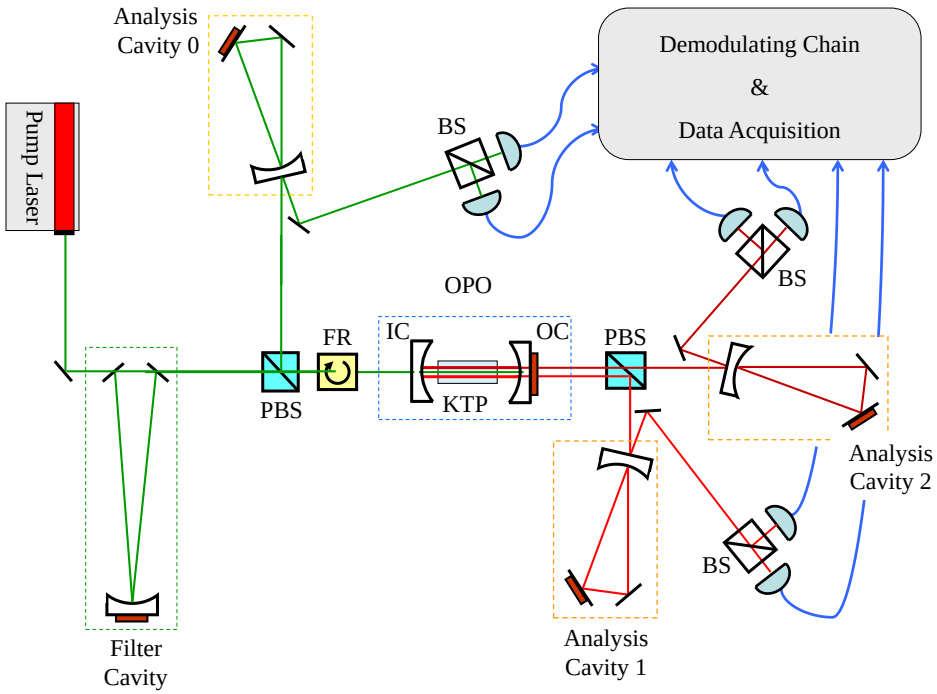

Figure 19: Setup for the reconstruction of the OPO beams' covariance matrix. PBS, polarizing beam splitter; BS, 50:50 beam splitter; IC, input coupler; OC, output coupler (OPO cavity); FR, Faraday rotator.

through the input coupler (IC) with a reflectivity of 70% for the pump field (532nm) and high reflectivity ($> 99\%$) at 1064nm. The reflected pump field is recovered from the Faraday rotator (FR). The infrared output coupler (OC) has a reflectivity of 96% at ≈1064 nm and high reflectivity ($> 99\%$) at 532 nm. Both mirrors are deposited on concave substrates with a curvature radius of 50 mm. The crystal is a type II phase-matched KTP (potassium titanyl phosphate, $KTiOPO_4$) with length $l = 12$ mm, average refractive index n=1.81(1) and antireflective coatings for both wavelengths. The average free spectral range for the three modes is found to be of 4.3(5) GHz. The cavity finesse for the pump mode is 15 and 124 for the signal and idler modes (the latter defined as the mode with the same polarization as the pump). The overall detection efficiencies are 87% for the infrared beams and 65% for the pump, accounting for detector efficiencies and losses in the beam paths. The threshold power is 60 mW, and the maximum pump power was 75% above the threshold. In order to reduce the effect of phonon noise on the system, the crystal is cooled to 260 K, and the OPO is kept in a vacuum chamber to avoid condensation.

Phase noise measurements were performed using the ellipse rotation method described in [Galatola 1991, Villar 2008], with the help of analysis cavities. Cavities 1 and 2 (for the transmitted infrared beams) have bandwidths of 14(1) MHz, and cavity 0 (for the reflected pump) has a bandwidth of 12(1) MHz. This ensures a full rotation of the noise ellipse for the chosen analysis frequency of 21 MHz. Mode matching of the beams to

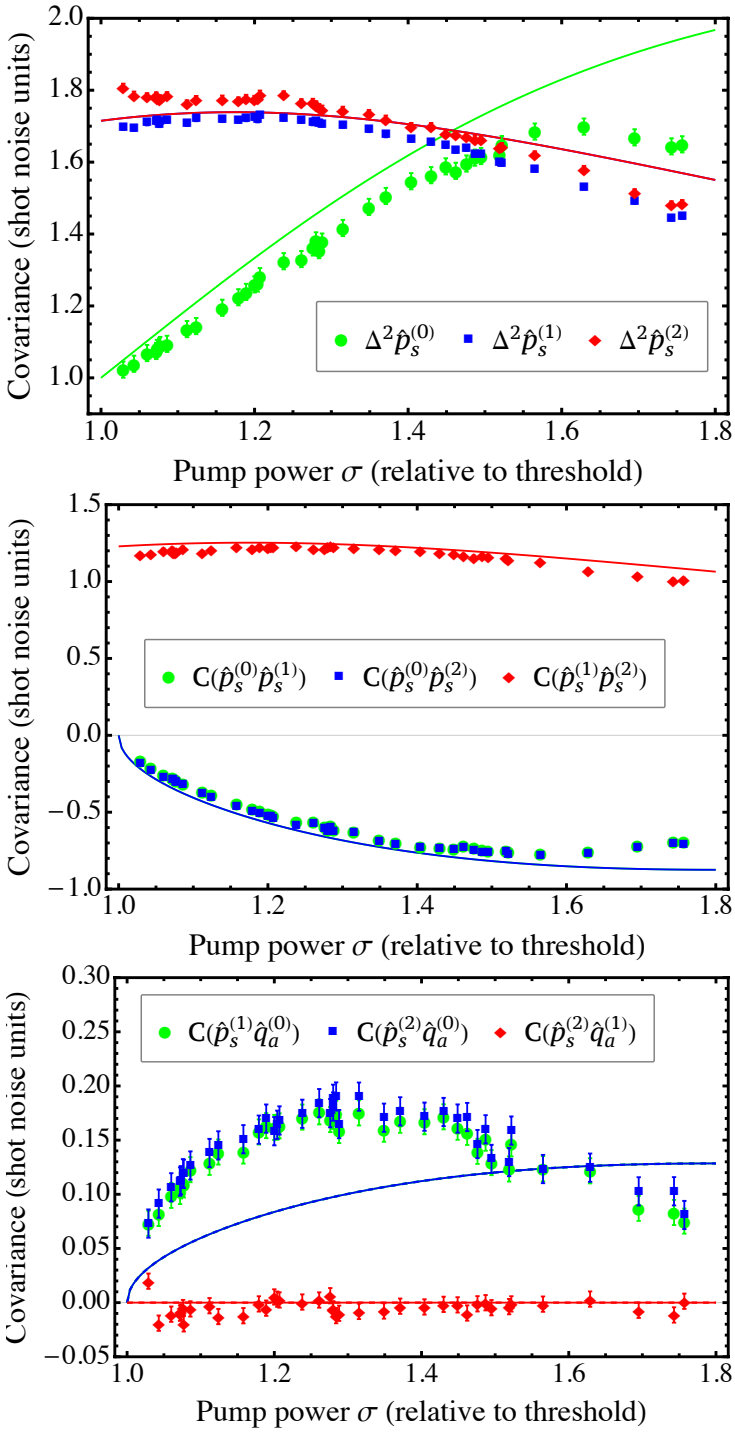

Figure 20: Measured variances of the amplitudes of the three fields coming from the OPO, in the symmetric description, followed by their respective correlations. Cross correlations between symmetric and antisymmetric modes are also displayed. Solid lines plot the corresponding theoretical curves of the theory developed in sections 3.1-3.5.

the analysis cavities was better than 95 %. Combining in-quadrature electronic local oscillators and cavity detection [Barbosa 2013c, Barbosa 2013b], the covariance matrix of the output sidebands was reconstructed. Since the detected modes are of Gaussian nature [Coelho 2015], determination of the covariance matrix is equivalent to the complete tomography of the output state of the sidebands of the involved intense optical fields.

Covariances for the intensity fluctuations are show in Fig. 20, in terms of the symmetric/antisymmetric modes, that results in a compact presentation of the covariance matrix. They present a good agreement between theory and experiment. Deviations for the pump field at higher pump power are consistent with the effects of mismatch in the pumping field, that are aggravated by thermal lensing on the crystal. The pump cavity mode will be more depleted with growing pump power, and the contributions of unmatched modes will be more relevant, degrading the measurement of the variance and contributing as an effective loss in detection. Nevertheless, correlations are less affected in this case, and present a better agreement. It is curious to notice that correlations between the symmetric and antisymmetric modes are observed for pump and signal (or idler) correlations, as predicted in [Barbosa 2013c], revealing that there is more information on the system beyond the three mode description. A full description of the measured state should necessarily involve six fields, and the distinct role of each sideband becomes relevant for the tomography of the system.

Phase quadrature measurements of fields of distinct colors are possible by the use of analysis cavities. The results shown in Fig. 21 were evaluated with a limited number of adjusting variables to describe the phonon coupling. The complete model involves three coupling channels between each mode of the carrier to distinct reservoirs, one for each oscillating mode of a crystal. Nevertheless, a toy model considering that pump and idler are coupled to the same reservoir (since they have the same polarization), and the orthogonally polarized signal with additional coupling to a second reservoir can be used to adjust the curves to the data. Best results were obtained with $g_{01} = 8.0\,\mathrm{mHz}$ for the pump coupling, $g_{21} = 3.6\,\mathrm{mHz}$ for the idler coupling, and $g_{11} = 1.9\,\mathrm{mHz}$ for signal coupling to one of the reservoirs, and $g_{12} = 2.7\,\mathrm{mHz}$ for signal coupling to the second reservoir. Thermal phonon population density was arbitrarily set to $\bar{n}_{\mathrm{th}} = 100$, acting just as a multiplicative constant in our model at high temperatures. It is curious to notice that $\sqrt{g_{11}^2 + g_{12}^2} \sim g_{21}$, and $g_{01} \sim 2g_{21}$, consistent with the scaling with wavelength described in the semiclassical model for the phonon noise [César 2009].

It is clear that the photon-phonon coupling leads to additional noise to the system, that should degrade the purity, if we compare with the expected results of the variance in absence of phonon noise, shown by dashed lines in Fig. 21. This coupling prevents the observation of phase squeezing for the pump mode in the present condition, and adds noise to signal and idler fields. Since this additional noise is not perfectly correlated, it will lead to degradation on the squeezing level at the sum of the phases, as we would expect

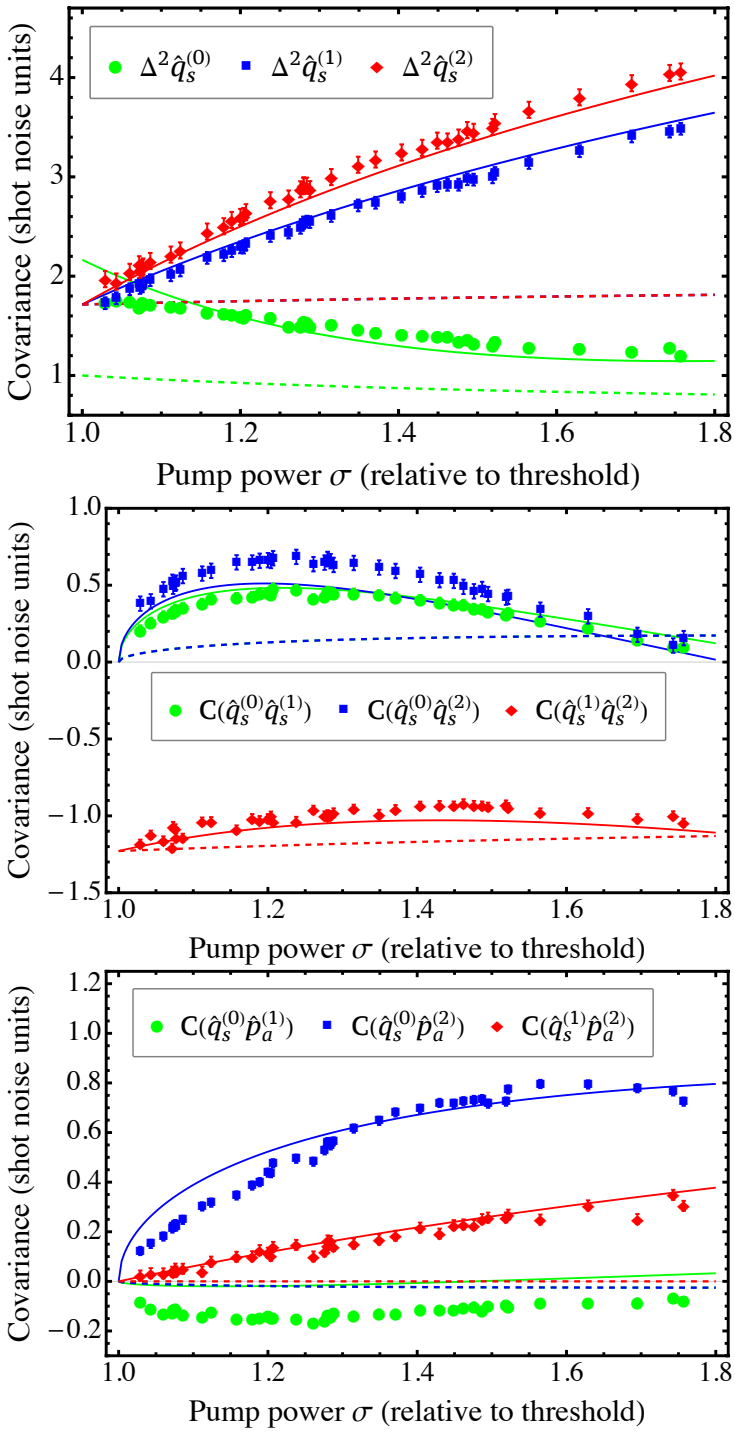

Figure 21: Measured variances of the phase of the three fields coming from the OPO, in the symmetric description, followed by their respective correlations. Cross correlations between symmetric and anti-symmetric modes are also displayed. Solid lines plot the corresponding theoretical curves of the theory developed in sections 3.1-3.5. Dashed lines are the result we would expect in the absence of phonons noise.

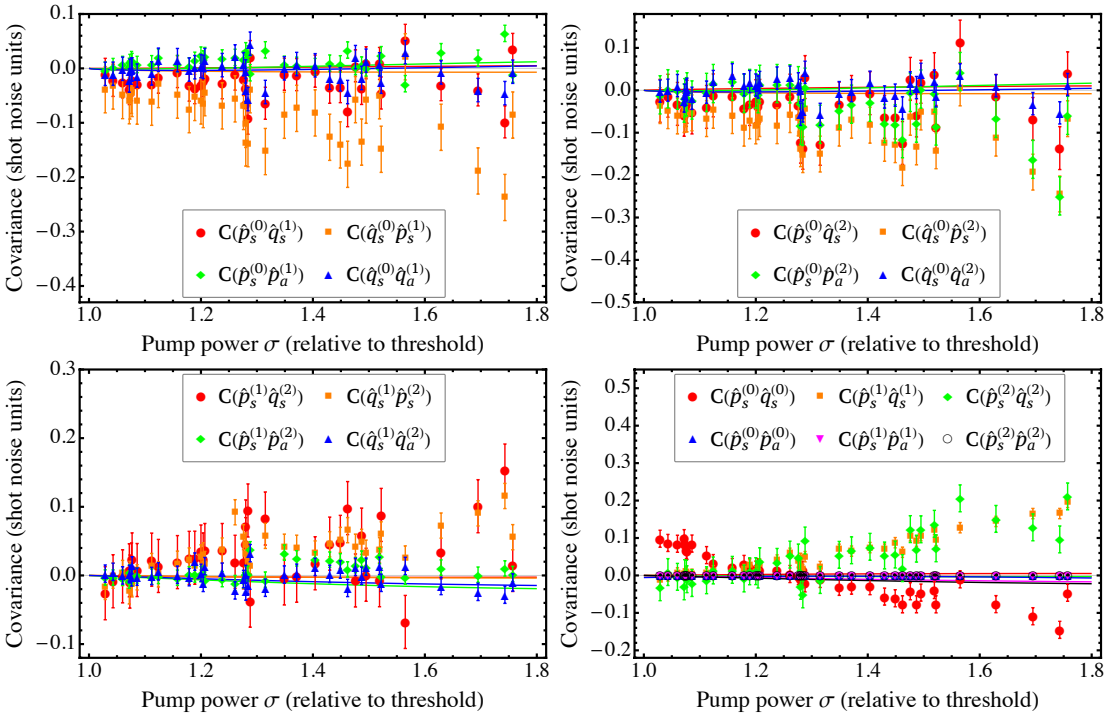

Figure 22: Measured correlations between amplitude and phase for each mode in symmetric/antisymmetric description. Solid lines plot the corresponding theoretical curves of the theory developed in sections 3.1-3.5.

in the generation of entangled modes of the field [Reid 1988, Reid 1989]. Nevertheless, quantum correlations for two [Villar 2005] and three modes [Coelho 2009] can be observed if adequate control of the phonons is available.

So far, we have presented all the measurements for the 18 non-zero terms on the matrices given in Eqs. (3.5.16) and (3.5.17). A complete description of the system should involve all the correlations between phase and amplitudes of each field in symmetric and antisymmetric description. The present model shows that for perfect resonance of the carriers, the contribution of the other terms in (3.5.16) and (3.5.17) should be zero. Experimental results are close to that, as can be seen in Fig. 22. These Cross-correlations may become effectively nonzero for growing pump powers, where thermal effects provide some change in the refractive index leading to small detunings of the carrier modes.

In conclusion, the experimental results are in good agreement with the simple model developed here, involving the transformation of the field operators in their reflection by a cavity, the nonlinear coupling among the fields by the crystal and the photon-phonon coupling. In the present case, discrepancies between this model and the semiclassical one are smaller than 4% of the standard quantum level[2] being both compatible with the experimental results.

Note that we had restricted the analysis to a linear model for the reconstruction of the covariance matrix, valid for small intracavity gain. Since the output fields are in a

[2]Except for amplitude variance of the pump, reaching 9%.

Gaussian state for all practical purposes [Coelho 2015], it characterizes a complete state tomography involving six modes of an OPO in a wide range of pump values, opening the path to explore the structure of hexapartite entanglement in this system as we will see below.

3.6.2 *Hexapartite entanglement*

As seen in Sec. 3.1, the Hamiltonian involving the specific sideband modes of the three carriers, with $\Omega > 0$, is given by [see Eq. (3.1.8)]

$$\hat{H}_\chi(\Omega) = -i\hbar\frac{\chi}{\tau}\Big[\alpha^*_{\omega_0}\left(\hat{a}^{(1)}_{\omega_1+\Omega}\hat{a}^{(2)}_{\omega_2-\Omega} + \hat{a}^{(1)}_{\omega_1-\Omega}\hat{a}^{(2)}_{\omega_2+\Omega}\right) + \alpha_{\omega_1}\left(\hat{a}^{(0)\dagger}_{\omega_0+\Omega}\hat{a}^{(2)}_{\omega_2+\Omega} + \hat{a}^{(0)\dagger}_{\omega_0-\Omega}\hat{a}^{(2)}_{\omega_2-\Omega}\right) + \alpha_{\omega_2}\left(\hat{a}^{(0)\dagger}_{\omega_0+\Omega}\hat{a}^{(1)}_{\omega_1+\Omega} + \hat{a}^{(0)\dagger}_{\omega_0-\Omega}\hat{a}^{(1)}_{\omega_1-\Omega}\right) - \text{h.c.}\Big], \quad (3.6.1)$$

and the total Hamiltonian is given by the sum of the contributions for each positive frequency Ω, as $\hat{H}_\chi = \int_\epsilon^\infty d\Omega \hat{H}_\chi(\Omega)$. Thus, the detailed treatment of the state of the sideband modes associated with a single analysis frequency Ω is decoupled from those of frequencies $\Omega' \neq \Omega$.

The resulting Hamiltonian includes, therefore, a pair of terms involving the creation and annihilation of pairs of photons in symmetric sideband modes of signal and idler fields, mediated by the mean pump field. This term is associated with two-mode squeezing operations, and it is the leading term when the OPO is below threshold, resulting in entangled EPR states [Ou 1992] or squeezing in the case of degenerate signal and idler modes [Wu 1986a]. Nevertheless, above threshold, mean field amplitudes for signal and idler are non-zero, and the other four terms will imply in photon exchange between the pump sidebands and the downconverted sidebands, mediated by the other downconverted mean field. These beam splitter operations will couple all the six sidebands in a ring, leading to a cascaded coupling among all modes. The result is an hexapartite entangled state, controlled by the mean fields (Fig. 23).

Therefore, the state of the sidebands will depend on the mean fields, and it can be directly related to the normalized pump power σ for exact resonance [see Eqs. (2.3.11)-(2.3.13)], taking the oscillation threshold as $\sigma = 1$. Variation of this single parameter will enable the exploration of this rich structure of nonclassical fields. The only missing part in the current discussion comes from phonon noise, responsible for degradation of the purity of the field state, that is treated in detail in the Sec. 3.5 and analized in the previous subsection. Moreover, since only bilinear terms are involved, the resulting state will be Gaussian, as experimentally observed in [Coelho 2015].

Entanglement will be studied by the analysis of the physicality of the smallest symplectic eigenvalue $\tilde{\nu}$ of the covariance matrix for partially transposed density operator of

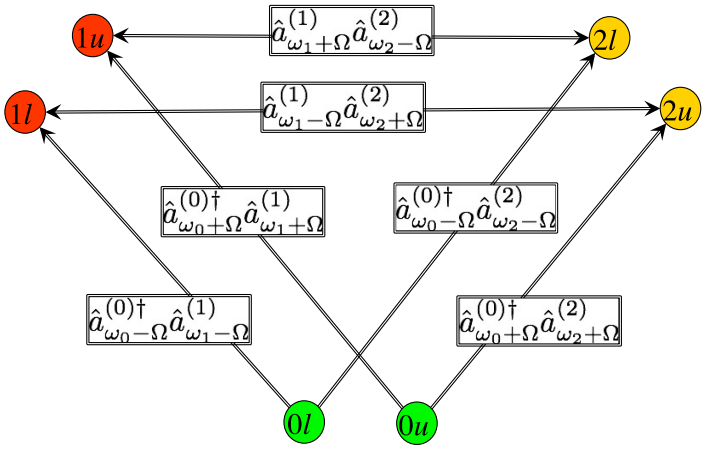

Figure 23: Coupling of the six sideband modes of the field. Signal and idler sidebands are coupled by photon pair creation and annihilation operators. All the other modes are pairwise coupled by beamsplitter operations.

the state [Simon 2000]. Whenever $\tilde{\nu} < 1$, there is entanglement between the bipartitions (further details in the subsection 2.1.2). In what follows, the superscript of $\tilde{\nu}$ denotes the modes that where selected among the six modes described in Fig. 23 as $n\ell$ for the mode at frequency $\omega_n - \Omega$ (i.e., at the lower sideband), and nu for modes at the upper sideband $\omega_n + \Omega$, n referring to the carrier frequency. Experimental data for the covariance matrices were presented in the previous subsection, as well as their theoretical values. They are used in the evaluation of $\tilde{\nu}$, as discussed in the subsection 2.1.2.

The error bars of the experimental symplectic eigenvalues are calculated from the measured covariance matrix (with the respective errors for each of its elements) and using the Monte Carlo method. Basically, a new random covariance matrix is constructed from the measured matrix and its uncertainties. Each element of the new matrix is calculated as the sum of the element of the matrix measured with a random Gaussian distribution of average null and standard deviation equal to the uncertainty of the measured matrix. We perform ten thousand simulations, each of them providing a symplectic eigenvalue. Once this is done, a histogram is constructed and, the uncertainty for $\tilde{\nu}$ is extracted from it. The details of this procedure are very well explained in [Cassemiro 2008a].

If we transpose the individual sidebands, in a 1×5 bipartition, we can observe that the measured states are fully entangled over the measured region (Fig. 24a), and although the phonon noise degrades the violation of the entanglement limit $\tilde{\nu} = 1$, it is not sufficient to lead to separability in this case. This is in contrast with the situation involving the pair of sidebands of a single field (Fig. 24b), where the phonon noise leads to an apparent decoupling of the pump field for powers beyond 65% above the threshold. The resulting curve is very close to the one obtained in the demonstration of tripartite entanglement [Coelho 2009], when it was considered the symmetric combination of sidebands as a single mode. We should notice that violation is always larger for bipartitions involving at least one of the sidebands of the downconverted fields. We can see that this violation

is maximized at the threshold, where we have the transition from a pure pair of bipartite states [Ou 1992] to the situation where depletion of the pump couples the amplitudes of the three modes, and energy conservation leads to phase correlations [Coelho 2009].

Next, we analyze 2×4 bipartitions. In Fig. (24c), upper and lower sidebands of pairs of distinct fields are transposed. In Fig. (24d), upper or lower sidebands of distinct fields are transposed. As far as just one of the sidebands of the downconverted fields is contained in the subset, the curves present a similar behavior to the one observed for 1×5 bipartition of a single sideband of the downconverted field, demonstrating that this is the leading term in the entanglement of the system. The situation changes if two modes of the downconverted fields are taken in the bipartition. If both upper sidebands are taken in one subsystem, the violation is maximized, and remains insensitive to the pump power. This is reminiscent of the Einstein-Podolsky-Rosen (EPR) entangled state generated below threshold, but also from the twin beam generation of the OPO above threshold. These modes, and their counterpart in the lower sidebands, are responsible for the so called amplitude correlation [Heidmann 1987], and are directly connected by two mode squeezed state operators in the scheme in Fig. 23. On the other hand, if upper and lower sidebands of the downconverted fields are taken in the subsystem, the violation is much smaller, but increases monotonically with the pump power within the studied range.

Finally, we analyze the six 3×3 bipartitions. In Fig. (24e), all modes come from different fields. Once again, maximal violation is obtained when a pair of upper and lower modes of each downconverted fields are in the same bipartition. But entanglement persists even if both upper, or both lower modes, are taken together with one of the pump modes. In Fig. (24f), bipartitions involve both sidebands of a field, and one sideband of other field. Therefore, the entanglement observed for single modes (Fig. 24a) is enhanced with the help of the split of the sidebands of a single field.

Some features are worth of notice. The stronger and more resilient entanglement occurs on bipartitions where the upper sidebands of signal and idler fields are split from their lower sidebands. That is exactly the modes that are directly connected by a two-mode squeezed state generator (Fig. 23), and are reminiscent of the sub-threshold entangled pair. It is important that this violation is insensitive to pump power, just as the twin beam noise compression in the OPO.

Next, when only one of the sidebands of the downconverted fields is kept apart in one partition, entanglement is yet strong, although not as strong as previously. This is the most common situation, occurring in 16 of the possible bipartitions. It is slightly dependent on the pump power, but remains entangled all over the range.

The next situation it the one where upper and lower sidebands of one downconverted field are split from its twin counterpart. In the four cases where this happens, entanglement is monotonically reduced for increasing pump power. Finally, there are situations

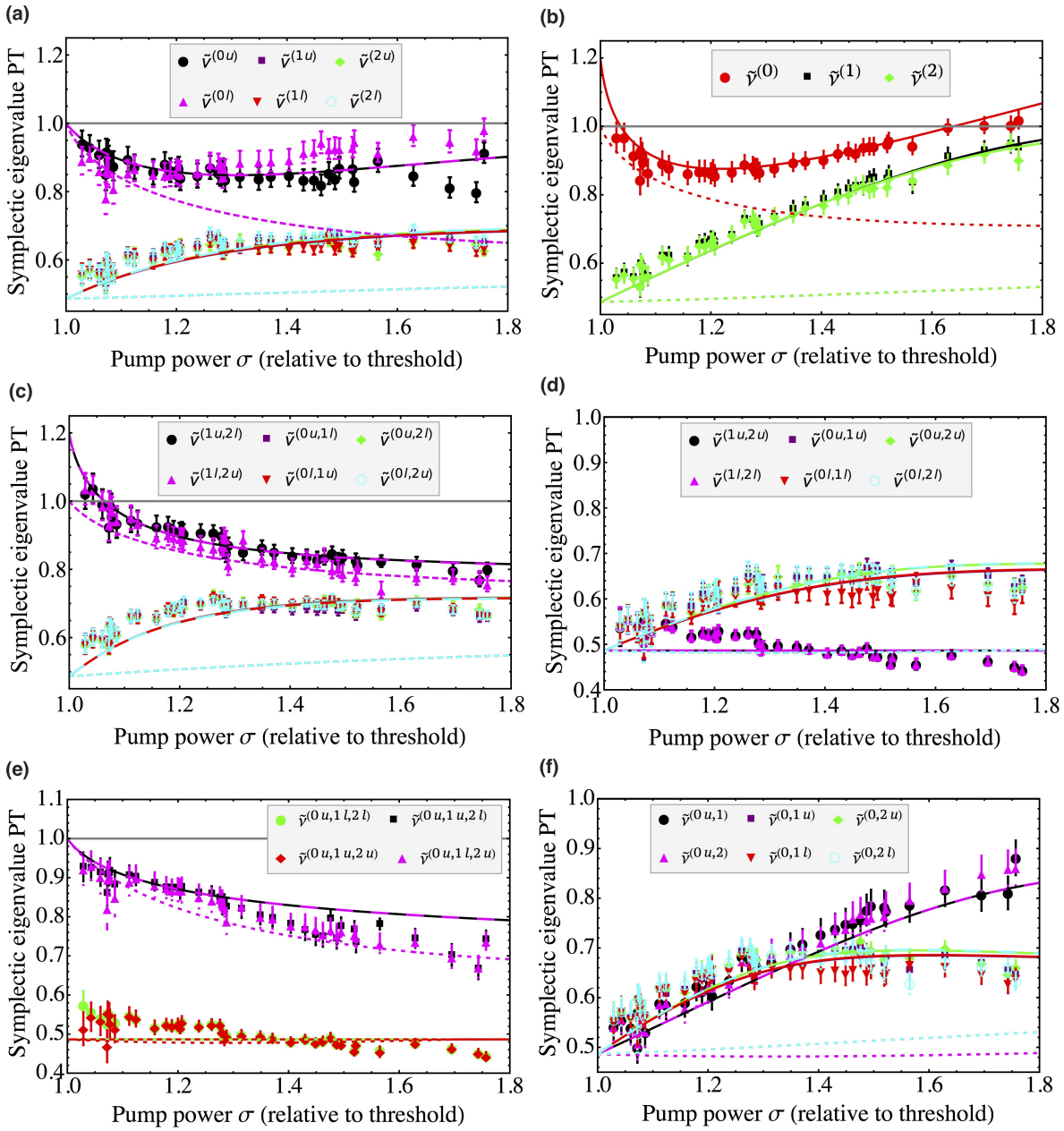

Figure 24: Smaller symplectic eigenvalues as an entanglement witness for normalized pump powers up to 80% above threshold: (a) (1×5) bipartition involving a single sideband, (b) (2×4) bipartition involving pairs of sidebands of a single carrier, (c) (2×4) bipartition involving upper and lower sidebands of a pair of fields, (d) (2×4) bipartition involving upper or lower sidebands of a pair of fields, (e) (3×3) bipartition involving at least one mode of each field, (f) (3×3) bipartitions involving a pair of modes of a single field and one mode of the remaining field.

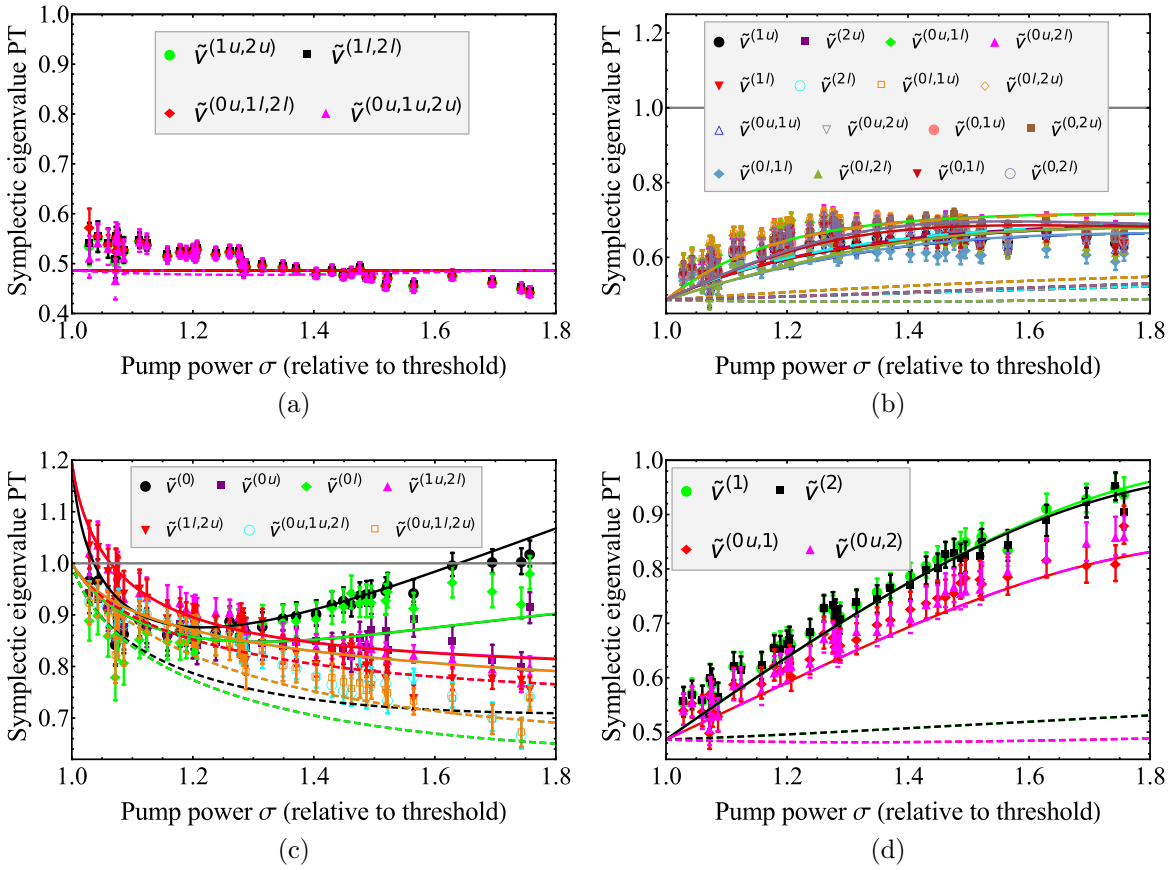

Figure 25: Ranking of entanglement. a) the strong entanglement-two squeezers, b) the resisting entanglement - single squeezer, c) the weak entanglement - the beam splitter and d) the declining entanglement - squeezers and beam splitter.

where entanglement is not observed close to threshold. It happens when the upper sideband of signal and lower sideband of idler are in the same partition, and their counterparts in the other. These are exactly the pair of modes connected by the squeezing operator, and close to threshold the beam splitter terms are negligible due to the low value of the mean field of signal and idler fields. Therefore, we have two independent sets of modes. They only become entangled when the pump power is increased, and the intense mean downconverted fields begin to enable the photon exchange of these modes with the pump, leading finally to entanglement. For this same reason, the situation where the partition involving only upper and/or lower sidebands of the pump have negligible entanglement close to threshold: the pump field is barely connected to the downconverted modes. Although entanglement grows with the pump power, phonon noise on signal and idler begins to reduce their correlation with the pump, eventually leading to disentanglement for higher pump power. In summary, we can say that we have 4 types of entanglement for the analyzed partitions: strong, resisting, weak, and declining entanglement as shown in Fig. 25.

In conclusion, the system presents hexapartite entanglement for pump power in the range from 1.1 to 1.6 above threshold. Entanglement can be revealed by stronger violations

if the modes directly coupled by two mode squeezing are split, but the beam splitter operations acting recursively over the modes in the cavity feedback lead to multimode entanglement involving all the fields. Better results can be expected if phonon noise is suppressed (dashed lines in Figs. 24 and 25).

4 Generation and characterization of CAEs from a cold atomic ensemble

In this chapter, the main experimental results in our study of the storage and extraction process of up to two CAEs in a cold atomic ensemble are shown. A portion of these results was published in [Ortiz-Gutiérrez 2018].

In section 4.1, we begin by describing how to create a cold atomic ensemble in our laboratory. Next, in section 4.2, we describe our series of experiments which were conducted in three stages. In the first two stages, subsections 4.2.1 and 4.2.2, the single and two-photon superradiances are investigated simultaneously through the same experiment, just being heralded by different types of events during the writing process. Possible correlations between the two photons on the two-photon wavepacket are also investigated. As discussed in subsection 2.6.3, the theory presented in [Barros 2018] is developed neglecting any effect of reabsorption of photons by the ensemble in the reading process, in which case no correlation between the two photons should be observed. In this case, the two-photon wavepacket should be simply the product of two independent single-photon emissions, as stated in Eq. (2.6.45). In this way, we are able to investigate possible correlations between the two photons emitted in the reading process by comparing the experimentally measured two-photon wavepackets with the expected curves coming from the experimentally measured single-photon wavepackets, and assuming independence between the emitted photons. Finally, in the third stage (subsection 4.2.3), a statistical characterization of the fields is performed in order to demonstrate the presence of quantum correlations between the photons emitted in the writing and reading processes, and also to characterize the quantum state of the system. All the experimental work was done jointly with Luis Ortiz Gutiérrez, and his doctoral thesis [Ortiz-Gutiérrez 2017] contains extra details on the experimental system.

4.1 Atomic ensemble production

For all experiments below, a cold ensemble of N rubidium 87 (^{87}Rb) atoms, obtained from a MOT, was used. These atoms belong to the family of alkaline metals, so they have sev-

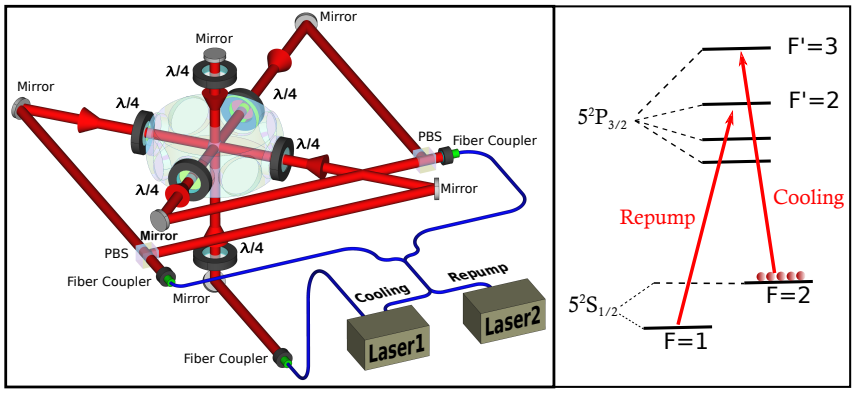

Figure 26: The configuration of the laser beams in our magneto-optical trap.

eral properties that facilitate their cooling and trapping [Steck 2015].The most important of these properties is that they have a cyclical transition between levels $\left|5^2S_{1/2}, F = 2\right\rangle$ and $\left|5^2P_{3/2}, F' = 3\right\rangle$, as mentioned in the section 2.5. The particular experimental setup of our MOT is shown in Fig. 26. In this configuration, there are 4 perpendicular independent beams in the horizontal plane and only the vertical axis is constituted by a single retroflected beam. In order to achieve the configuration of circular polarizations necessary for the cooling process to take place (see section 2.5), we use a set of six quarter-wave ($\lambda/4$) plates right before the vacuum chamber. The four beams of the horizontal plane come from two beams through PBS cubes, as shown in Fig. 26. However, these two beams, in turn, come from the two outputs of a Fiber Beam Splitter (FBS), whose two inputs are, on the one hand, cooling light (red detuned from the $|F = 2\rangle \rightarrow |F' = 3\rangle$ transition) and, on the other hand, repumping light (resonant with the $|F = 1\rangle \rightarrow |F' = 2\rangle$ transition). In this way, we see that the repumping light is going to be involved in the four beams of the horizontal plane, all being bichromatic. All light beams are derived from diode lasers (THORLABS DL7140-201S) modulated by Acoustic-Optic Modulators (AOMs) to address the D_2 line of ^{87}Rb at 780 nm. In the end, we combine a magnetic field gradient of 10 G/cm, generated through two coils in anti-Helmholtz configuration (not shown on Fig. 26), with the cooling light and the repumping light to load up to $N \approx 10^8$ Rubidium atoms into the MOT with temperatures below 1 mK.

The trap was kept on for 23 ms, before the trapping beams and the magnetic field were turned off for 2 ms, as shown in Fig. 27. The MOT repumping light is kept on for an extra 0.9 ms to pump all atoms to the $|F = 2\rangle$ state, the initial $|g\rangle$ state of our scheme. After the repumping light is turned off, the ensemble is kept in the dark from all MOT light fields during 1.1 ms, the period in which the experiments take place. This whole process is repeated with a frequency of 40 Hz. The residual magnetic field is minimized up to a ground state linewidth of about 100 kHz, corresponding to magnetic fields on the order of 36 mG, by means of three pairs of compensating coils in Helmholtz configuration and performing microwave spectroscopy between the two hyperfine ground states [de Almeida 2016]. Such linewidth should lead to a coherence time on the order

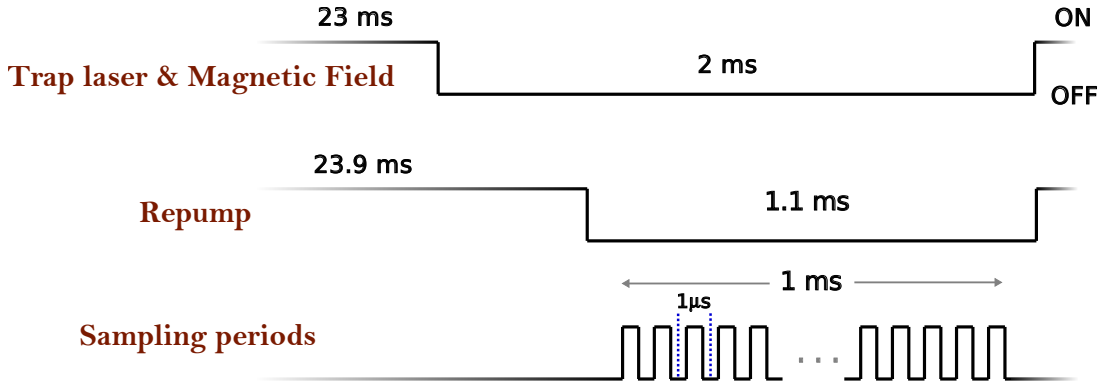

Figure 27: Timing for all the experiments in section 4.2.

of 1.6 μs, much larger than the separation between write and read processes employed in our experiments.

In all the experiments in the next section, during the dark period of the MOT, a sequence of 1000 sampling periods of 1 μs duration is executed (see Fig. 27). Since the temperature of the atoms is less than 1 mK, their motion can be neglected during a sampling period. At each sampling period, a sequence of write and read pulses excite the ensemble. The time duration of each of these pulses will depend on the specific experiment that we are considering.

4.2 Experiments

4.2.1 *First configuration: linear polarizations*

The setup for our first stage of experiments is shown in Fig. 28. Each atom exhibits a Λ-type level scheme consisting of a ground state $|g\rangle = |F = 2\rangle$ a storage state $|s\rangle = |F = 1\rangle$ and a excited state $|e\rangle = |F' = 2\rangle$ (see Fig. 29). The atoms are initially prepared in the ground state by the MOT repumping light, as explained in section 4.1. The write pulse has a duration of about 50 ns and is 22 MHz red-detuned to the $|g\rangle \rightarrow |e\rangle$ transition. Its duration and frequency are controlled by a sequence of two AOMs, one of them in a double-pass configuration. The 4σ diameter of the write beam in the MOT region is 420 µm. As a result of its action, photons may be emitted in the mode, called field 1, coupled to an input of a single-mode FBS that divides the output to two Avalanche Photo-Detectors (APDs), D1a and D1b. The field responsible for our signal is emitted in the $|e\rangle \rightarrow |s\rangle$ transition. In this way, the detection of n photons in field 1 heralds the storage of n CAEs in the atomic ensemble.

The Optical Depth (OD) of the atomic ensemble is measured by sending a very weak long pulse (about 1 μs long) in the write-field spatial mode, with an adapted detuning Δ to the $|g\rangle \rightarrow |F' = 3\rangle$ transition, and observing its transmission $T(\Delta)$ after propagation in the atomic ensemble. More specifically, from the full-width at half-maximum δ of the transmission curve $T(\Delta)$, we could calculate directly the OD of the ensemble through

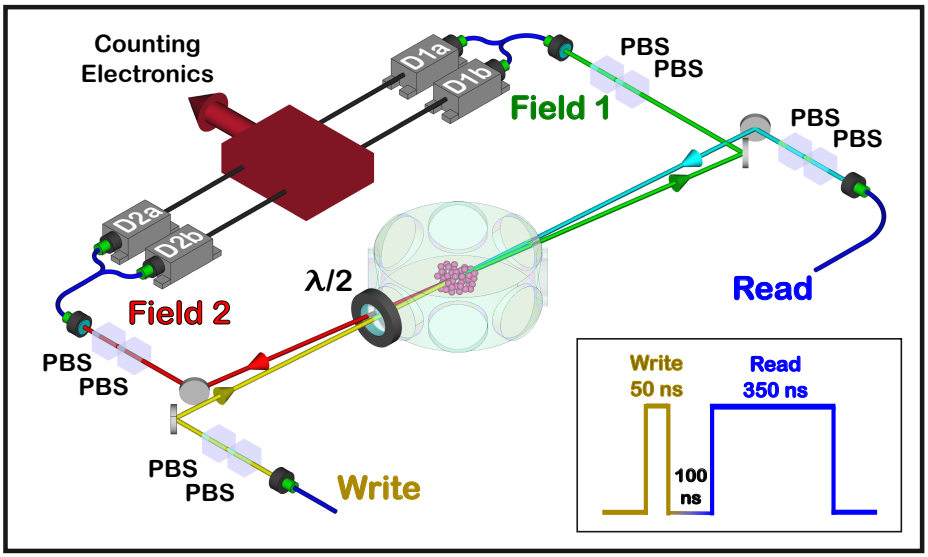

Figure 28: Experimental setup for the first configuration considered in our experiments: linear polarizations.

the expression $OD = \ln(2)\left[1 + (\delta/\Gamma)^2\right]$ [Gattobigio 2010], where $\Gamma/2\pi = 6$ MHz is the inverse lifetime of the $|F' = 3\rangle$ state. This measurement technique allows one to measure in a reliable fashion large optical depths, which is not possible by measuring directly $T(\Delta = 0)$ due to finite signal-to-noise ratio and probe laser spectral width. The OD is a crucial parameter [de Oliveira 2014], since it is proportional to the number of atoms in the system and is easily accessible experimentally. The number of atoms controls, for example, the decay time of the collective superradiant emission [Mendes 2013b]. The measurement of OD was performed typically in the center of the dark period of the MOT, without write or read fields acting on the ensemble, and was changed by tuning the power of the trap laser (laser 1 in Fig. 26).

In the MOT region, field 1 has a 4σ diameter of 150 μm and "passes" through the middle of the write beam forming an angle of about 2° with it. The polarizations of write beam and field 1 are linear and orthogonal to each other (see Fig. 29), with extinction ratios on the order of 10^5 for the orthogonal polarization in each field. This degree of polarization of the fields is achieved by the transmission through a pair of PBSs, and the rotation of the polarization of the write beam is done by a half-wave ($\lambda/2$) plate right before the vacuum chamber with the addition a $\lambda/4$ plate (not shown on Fig. 28) to correct for small polarization distortions on the optical pathway.

About 100 ns after the write field is turned off, the read pulse is turned on for 350 ns (see inset of Fig. 28) by a single AOM. This pulse is resonant with the $|s\rangle \rightarrow |e\rangle$ transition and maps the collective state with n CAEs in $|s\rangle$ to a collective state with n CAEs in $|e\rangle$, which then decay superradiantly back to the initial state $|g\rangle$ [Ortiz-Gutiérrez 2018], emitting photons in a second light mode, called field 2, coupled to the input of a single-mode FBS that divides the output to two APDs, D2a and D2b. We call field 2 this final

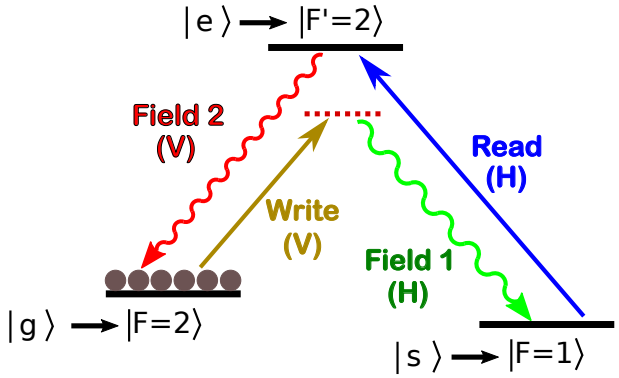

Figure 29: Lambda scheme for the configuration of linear polarizations. H and V denote horizontal and vertical polarization, respectively.

superradiant emission of the overall, parametric four-wave-mixing process [Felinto 2005]. The polarizations of read pulse and field 2 are linear and orthogonal to write pulse and field 1, respectively, as shown in Fig. 29. In addition, the read and field-2 beams are mode matched and counterpropagating to the write and field-1 beams, respectively. This configuration results in single-photon superradiance with negligible propagation effects [Mendes 2013b, de Oliveira 2014]. For alignment, the write beam may be coupled to the read-beam fiber, and vice versa, with about 80% coupling efficiency. On the other hand, an alignment laser field coming out of the field-2 fiber may be coupled with about 70% efficiency to the field-1 fiber.

As mentioned above, after the photons emitted in fields 1 and 2 are coupled to their respective single-mode FBSs, they reach two independent pairs of APDs, as shown in Fig. 28. The output of the APDs are directed then to a counting card (MCS6A from FAST ComTec), which records all photodetection events for later analysis by software, with 0.1 ns time resolution. In this way we may compute the various integrated quantities $N_{1a1b2a2b}$ giving the joint clicks-number for all detection events in a single sampling period. Note that the subscripts represent the different APD's in the way they were named in Fig. 28, and the possible values that these subscripts can take are only 0, 1 and X. It takes the value 0 when the detector corresponding to the subscript has not tired, the value 1 when the detector detects a photon, and we use the value X to indicate that we are not interested in this information, i.e. we are going to count here both cases, when the corresponding APD fires and when it does not. For example, N_{10XX} means that the detector 1a detected a photon, while we are sure that the other detector of field 1 (1b) hasn't detected anything and that both detectors of field 2 (2a and 2b) may have clicked or not. From these quantities we may calculate, for example, three important normalized correlations:

$$g_{11} = \frac{N_{11XX}}{(N_{1XXX})(N_{X1XX})} N_{\mathrm{SP}}, \tag{4.2.1}$$

$$g_{22} = \frac{N_{XX11}}{(N_{XX1X})(N_{XXX1})} N_{\mathrm{SP}}, \tag{4.2.2}$$

$$g_{12} = \left[\frac{N_{1XX1}}{(N_{1XXX})(N_{XXX1})} + \frac{N_{1X1X}}{(N_{1XXX})(N_{XX1X})} + \frac{N_{X1X1}}{(N_{X1XX})(N_{XXX1})} + \frac{N_{X11X}}{(N_{X1XX})(N_{XX1X})} \right] \frac{N_{\mathrm{SP}}}{4}, \tag{4.2.3}$$

where N_{SP} is the total number of sampling periods performed during the whole measurement time. The first two of these quantities measure the auto-correlations for fields 1 and 2, respectively. The third one measures cross-correlations between the two photon fields, giving the probability of generating a photon pair divided by the probability of observing an accidental coincidence event. The singular quantum nature of the correlations between fields 1 and 2 may be directly verified by the violation of a Cauchy-Schwartz inequality,

$$R = \frac{g_{12}^2}{g_{11} g_{22}} \leq 1, \tag{4.2.4}$$

valid for classical fields [Kuzmich 2003, Clauser 1974]. Since g_{11} and g_{22} are typically bounded by a maximum value of 2 for our system [Kuzmich 2003], we have that $g_{12} > 2$ also indicates purely quantum correlations between the fields.

Another important quantity, is

$$p_c = \left[\frac{N_{1X1X} + N_{1XX1}}{N_{1XXX}} + \frac{N_{X11X} + N_{X1X1}}{N_{X1XX}} \right] /2, \tag{4.2.5}$$

which provides the conditional probability of detecting a photon in field 2 once a photon in field 1 was previously detected in the same sampling period. In other words, it is the probability of generating a photon in field 2 once the creation of the corresponding collective state is heralded by the detection a photon in field 1. Finally, it is worth noting that we may also compute all these quantities as a function of time inside each excitation pulse. This last measurement then provides the various wavepackets for the photons, together with the corresponding details of the dynamic of the reading process.

In order to identify the operating regime of our system, where one or two CAEs are efficiently stored in the atomic ensemble, it was necessary to perform a preliminary characterization. In Fig. 30 we plot then p_c, g_{12}, R, and the Twin Generation Rate (TGR) versus $p_1 \equiv (N_{1XXX} + N_{X1XX})/N_{\mathrm{SP}}$ [1], for an OD=31.4 and a read power of 9.50 mW[2].

[1] In order to be able to vary $p_1$in a controlled way, which corresponds to the probability that a photon is detected by one of the APDs of field 1 regardless of how many photons were detected on field 2,it is necessary to vary the power of the write beam. The way in which we vary the write power is by using different filters before the coupling of this beam into its optical fiber.

[2] The read power is fixed at a much greater value, since the extraction of the field-2 photon is a process that must be implemented with greater efficiency [Mendes 2013b].

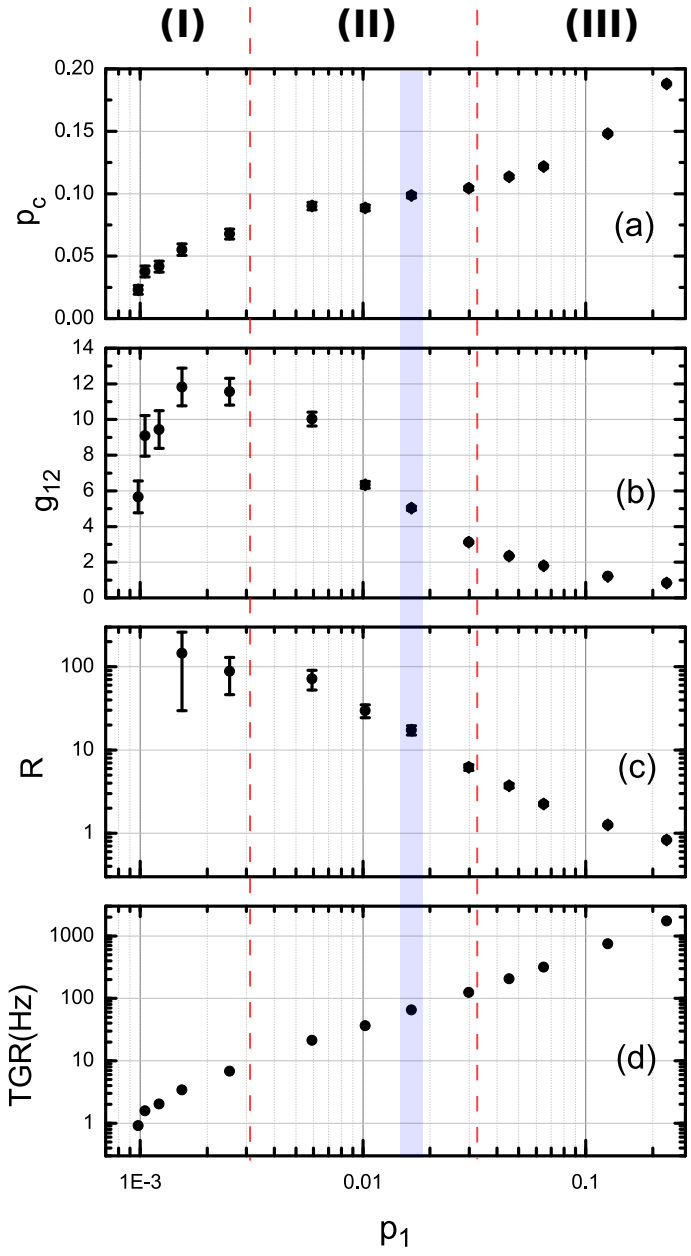

Figure 30: Characterization of the system for the first configuration considered. Panel (a) shows the conditional probability p_c, (b) the normalized cross-correlation function between fields 1 and 2, g_{12}, (c) the parameter R (directly related to the Cauchy-Schwartz inequality) that indicates the non-classical nature between fields 1 and 2 for R$>$ 1, and (d) the twin generation rate TGR. The wave packets measured in this configuration correspond to $p_1 = 0.0164$, highlighted on a blue vertical bar, where $p_c = 9.51\%$, $g_{12} = 5.25$, R= 19 and TGR=62.5Hz. The graphs show the transition of the region (I) dominated by spurious noises, passing through the region (II) that characterizes a region of individual CAEs, reaching the region (III) where multiple CAEs are generated.

The TGR represents the rate of coincidence counts for second and can be obtained by multiplying $(N_{1X1X} + N_{1XX1} + N_{X11X} + N_{X1X1})/N_{\mathrm{SP}}$ by the number of sampling periods per second (40000 in our case). The four panels in Fig. 30 were obtained from the same data set with around 10^6 sampling periods. Error bars come from the uncertainty in the accumulation of detection events, proportional to the square root of the number of detections. As can be observed in Fig. 30(a), the curve for the conditional probability p_c presents several regimes for the generation of pairs of photons. For high values of p_1, indicated by region III, p_c decreases as p_1 is reduced. This behavior indicates that processes of multiple CAEs decrease with the write-pulse energy, while the correlations g_{12} and the parameter R enter the nonclassical region with $g_{12} > 2$ and R> 1 [see Figs. 30(b) and 30(c)]. On the other hand, in region II, we can see that p_c remains almost constant, which indicates that we are in the single-photon regime where the detection of a photon in field 1 can lead to the detection of just one photon in field 2 [Laurat 2006]. Note that in this region g_{12} and R increase monotonically with the decrease in p_1. Finally, when passing to the region I, where p_1 is very low, spurious noises dominate the system and the conditional probability decreases rapidly as p_1 goes to zero. A similar behavior can be observed in the graphs of g_{12} and R . The explication for this behavior is because in the region of $p_1 \to 0$ the write power is so low that the detectors click more frequently because of spurious light than for the photons emitted in the write and read processes. As the spurious light has no correlation (g_{12}=1), the coincidence detections are much less likely than the singles ($p_{1,1} \ll p_1$), in this way $p_c \to 0$.

In principle, in order to measure the wavepackets of the photons emitted in the reading process, any value of p_1, that is within the region II shown in Fig. 30(a), can be selected. However, from the experimental point of view, only the larger values of p_1 in this region are suitable for this type of measurements. The reason for this is that many events of double and quadruple coincidences are needed in order to generate such wave packets with good temporal resolution. As shown in Fig. 30(d), the TGR in the region II is between 10 and 100 Hz. It is found that in this region the ratio between TGR and the four coincidences rate (detection of two photons in field 1 and two in field 2) is $\approx 2 \times 10^3$. Taking this into account and always trying to have values of g_{12} and R high enough, we have decided that the point to make this measurement would be $p_1 \approx 0.0164$, where we can see that $g_{12} = 5.25$, $p_c = 9.51\%$ and TGR= 62.5 Hz. The choice of these values corresponds finally to the choice of a certain write power.

The **single-photon wavepacket** is obtained from the quantity

$$\rho^c_{1,1}(t) = \left[\frac{N_{1010}(t) + N_{1001}(t) + N_{0110}(t) + N_{0101}(t)}{N_{10XX} + N_{01XX}} \right], \tag{4.2.6}$$

where the quantity in the numerator is proportional to the joint probability density of detecting a single photon in field 1 and a single photon in field 2 in a time window Δt

around t with $t = 0$ as the moment the read field is turned on. In this way, $\rho^c_{1,1}(t)$ provides the conditional probability density of detecting a single photon in field 2 around t after the detection of a photon in field 1. From this definition, we have

$$p^c_{1,1} = \int_0^\infty \rho^c_{1,1}(t)dt. \tag{4.2.7}$$

Therefore, the normalized single-photon wavepacket is obtained from

$$\widetilde{\rho}^c_{1,1}(t) = \frac{\rho^c_{1,1}(t)}{p^c_{1,1}}. \tag{4.2.8}$$

On the other hand, the **two-photon wavepacket** is obtained from the quantity

$$\rho^c_{2,2}(t,t') = \frac{N_{1111}(t,t')}{N_{11XX}}, \tag{4.2.9}$$

where the quantity in the numerator is proportional to the joint probability density of detecting two events in field 1 and two events in field 2, where $t + \Delta t$ and $t' + \Delta t'$ are the time windows[3] where the two events in field 2 are detected, respectively. In this way, $\rho^c_{2,2}(t,t')$ provides the conditional probability density of detecting two events in field 2, around t and t', respectively, after the detection of two events in field 1. The information contained in $\rho^c_{2,2}(t,t')$ can be divided into different wavepackets depending on the conditions we impose on the times t and t':

- If we do not consider any sort of ordering on times t and t', then we can define a wavepacket, independent of the detection order of the two photons in field 2, in the following way:

$$\rho^c_{2,2}(t) \equiv \left[\int_0^\infty \rho^c_{2,2}(t,t')dt' + \int_0^\infty \rho^c_{2,2}(t',t)dt'\right]/2. \tag{4.2.10}$$

- If $t = t_1$ and $t' = t_1 + \tau > t_1$, we can integrate over τ to obtain the conditional probability density to detect in t_1 the first photon of the pair in field 2:

$$\rho^{c1}_{2,2}(t_1) \equiv \int_0^\infty \rho^c_{2,2}(t_1, t_1+\tau)d\tau + \int_0^\infty \rho^c_{2,2}(t_1+\tau, t_1)d\tau. \tag{4.2.11}$$

  On the other hand, if the integration run over t_1, we obtain the conditional probability density to detect the second photon in field 2 at a time τ after the first one was detected:

$$\rho^{c\tau}_{2,2}(\tau) \equiv \int_0^\infty \rho^c_{2,2}(t_1, t_1+\tau)dt_1 + \int_0^\infty \rho^c_{2,2}(t_1+\tau, t_1)dt_1. \tag{4.2.12}$$

The corresponding normalized wavepackets for each of the expressions given in (4.2.10), (4.2.11), and (4.2.12), are denoted by $\widetilde{\rho}^c_{2,2}$, $\widetilde{\rho}^{c1}_{2,2}$ and $\widetilde{\rho}^{c\tau}_{2,2}$, respectively [4].

[3] $t, t' = 0$ at the moment when the read field is turn on.

[4] From now on, every time we use the word "wavepacket", we will be referring to the "normalized wavepacket".

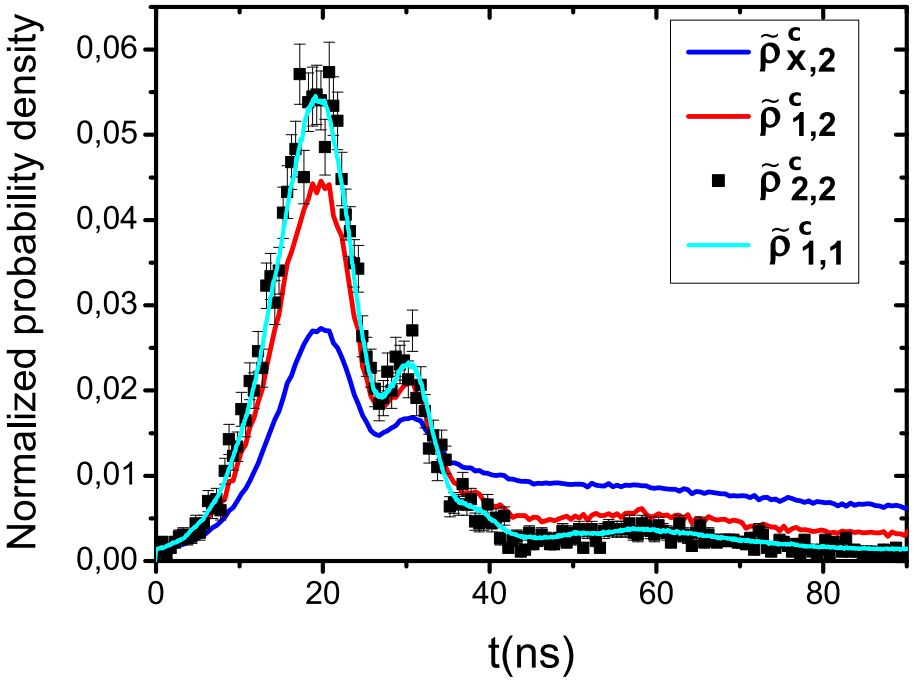

Figure 31: **Single-photon wavepacket (cyan curve)** compared with the normalized probability densities $\widetilde{\rho}^{c}_{X,2}(t)$, $\widetilde{\rho}^{c}_{1,2}(t)$ and $\widetilde{\rho}^{c}_{2,2}(t)$ to detect either field-2 photons at time t in the configuration of linear polarizations.

Before showing the measured wavepackets, it is worth saying that for the configuration considered in this subsection, where all atoms are initially prepared at the hyperfine level $|F = 2\rangle$, it is not possible to perform a direct comparison between the measured single- and two-photon wavepackets and their respective theoretical expressions deduced on section 2.6. The reason of this is because the theory considers simple three-level atoms in Λ configuration. However, what is actually possible to investigate with the experimental results and with the help of the theory, are the possible correlations between the two photons on the measured two-photon wavepacket, as will be seen below.

The measured single-photon wavepacket and the measured normalized conditional probability densities of detecting two photons in field 2 (irrespective to the detection order) conditioned over the different detections in field 1, for $\Delta t = 0.5$ ns, are plotted in Fig. 31. All these plots were obtained from the same data set with about 10^{10} sampling periods. In this figure we can see that the wavepackets clearly present beatings coming the various Rabi oscillations involved in the reading process through different Zeeman sublevels. As mentioned previously, this behavior was expected since we didn't use an optical pump in order to prepare the atoms in a particular Zeeman sublevel. Also, it can be seen that the two-photon wavepacket (squares in Fig. 31) is close to the single-photon wavepacket (cyan curve in Fig. 31). These results reflect the fact that emissions of the two photons in field 2 are close to independent, and each one is approximated to a single-photon emission from a atomic ensemble containing a single CAE. This conclusion is not valid anymore for the wavepackets $\widetilde{\rho}^{c}_{X,2}$ and $\widetilde{\rho}^{c}_{1,2}$, which present significant differences with

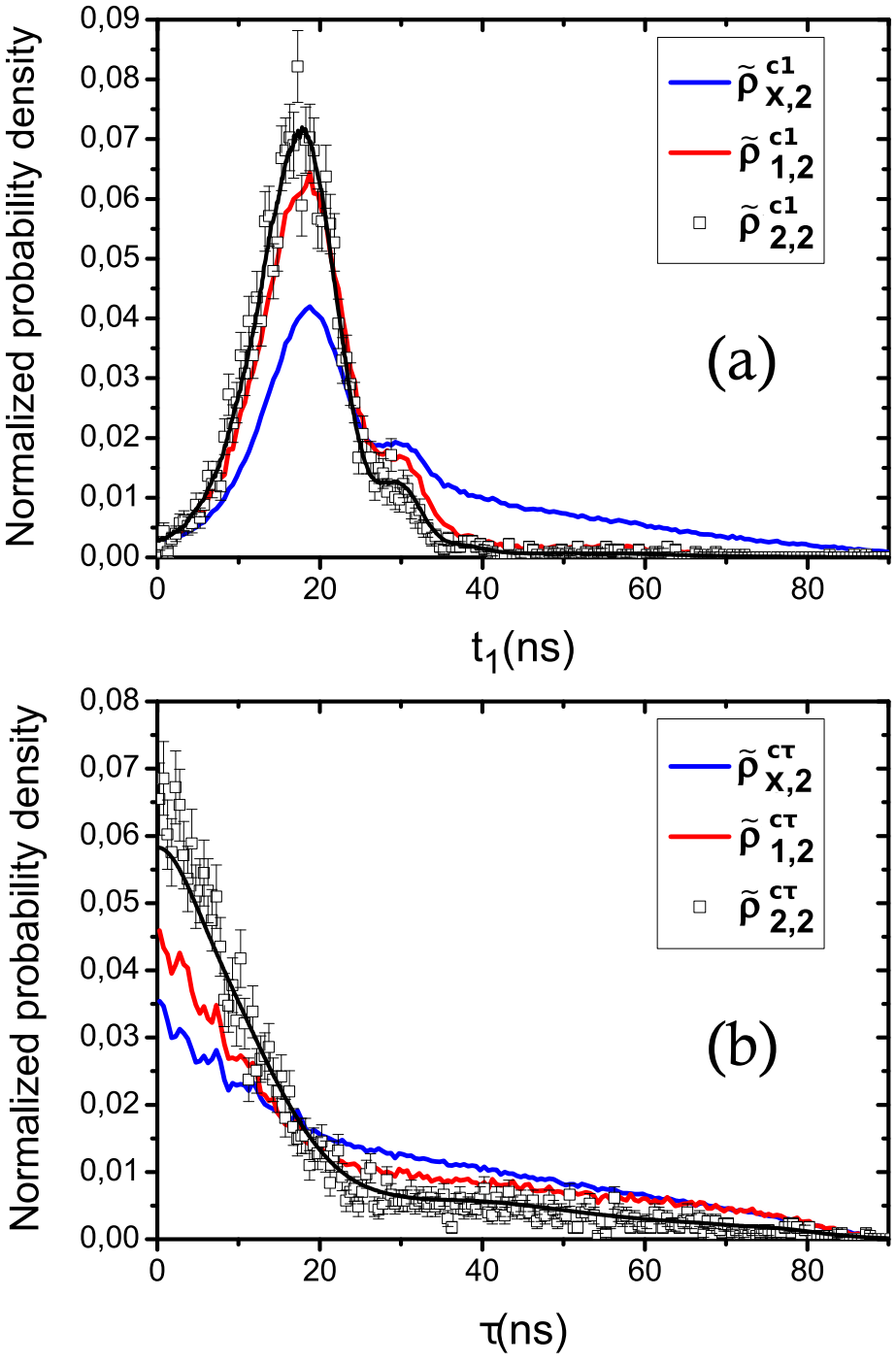

Figure 32: **Two-photon wavepackets (empty squares curves)** for the configuration of linear polarizations. Normalized probability densities $\widetilde{\rho}_{i,2}^{c1}(t_1)$ and $\widetilde{\rho}_{i,2}^{c\tau}(\tau)$, conditioned on the detection of i photons in field 1, to detect (a) the first field-2 photon at t_1 and (b) the second field-2 at time τ after the first detection, respectively. The black curves in (a) and (b) are obtained from Eq. (2.6.45) and the measured single-photon wavepacket (cyan curve in Fig. 31).

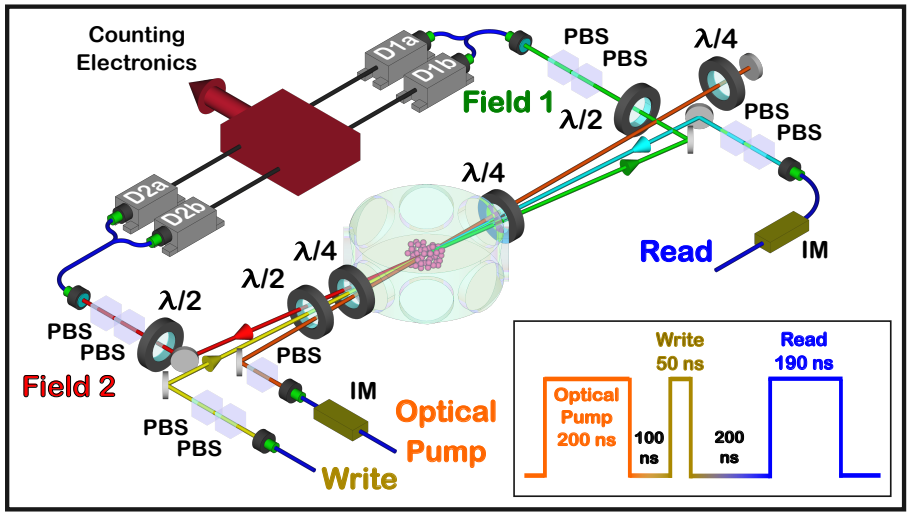

Figure 33: Experimental setup for the second configuration considered in our experiments: circular polarizations with optical pumping.

respect to the single-photon wavepacket.

As discussed in subsection 2.6.3, if we neglect the reabsorption of the field-2 photons by the atomic ensemble, the two-photon wavepacket can be found from the product of two independent single-photon wavepackets, as stated in Eq. (2.6.45). In what follows, to the two-photon wavepacket found in this way (using the measured single-photon wavepacket), it will be called the *numerical two-photon wavepacket*. In order to investigate if this approximation is valid in our system, in Fig. 32 it is shown the complete measured two-photon wavepacket (empty square curve) and the numerical two-photon wavepacket (black curve) As a comparison, wavepackets with other conditioning on the field 1 are also included. Since there are two detections in field 2, the wavepacket information was divided in two parts. In Fig. 32(a) we plot the normalized conditional probability densities $\widetilde{\rho}^{c1}_{X,2}$, $\widetilde{\rho}^{c1}_{1,2}$ and $\widetilde{\rho}^{c1}_{2,2}$ of detecting the first photon of the pair in field 2 at a time t_1 after turning on the read field. In Fig. 32(b) we plot the normalized conditional probability densities $\widetilde{\rho}^{c\tau}_{X,2}$, $\widetilde{\rho}^{c\tau}_{1,2}$ and $\widetilde{\rho}^{c\tau}_{2,2}$, of detecting the second photon of the pair at a time τ after the first one. As can be seen in Fig. 32(a) and (b), the numerical two-photon wavepackets successfully reproduce the behavior of the measured two-photon wavepackets. This clearly shows that the approach of considering independence in the emission of the two photons in field 2 is valid in our system. Once again this conclusion is not valid for wavepackets with other conditionings.

4.2.2 *Second configuration: circular polarizations with optical pumping*

In order to explore the single- and two-photon superradiances with a single Rabi frequency for the atoms and thus to be able to compare with their respective theoretical predictions, the experimental setup of Fig. 28 was modified as shown in Fig. 33. Two large modifications had to be introduced. First, an optical pump beam has been incorporated. Second,

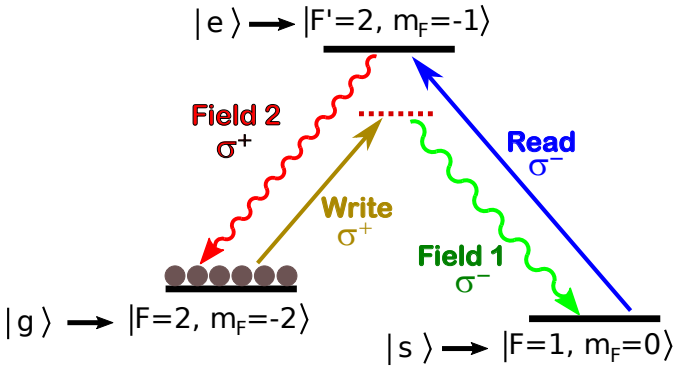

Figure 34: Lambda scheme for the configuration of circular polarizations.

two 10 GHz in-fiber Mach-Zehnder Intensity Modulators (IMs) has been incorporated in order to control the pulse durations in the experiment [5](see Fig. 33).

In this configuration, at each sampling period an optical pumping pulse of 200 ns duration prepares the atoms at the $|g\rangle = |F = 2, m_F = -2\rangle$ state. This beam is red-detuned 32 MHz from the $|F = 2\rangle \rightarrow |F' = 3\rangle$ transition and has circular σ^- polarization, being retro-reflected to reduce its mechanical action over the atoms. Once in state $|g\rangle$, the atoms are excited during 50 ns by a circular, σ^+ write pulse 22 MHz red-detuned from the $|g\rangle \rightarrow |e\rangle$ transition, with $|e\rangle = |F' = 2, m_F = -1\rangle$. With small probability, n atoms may be transferred to the state $|s\rangle = |F = 1, m_F = 0\rangle$ spontaneously emitting n σ^- photons in field 1 (see Fig. 34). These are coupled to a single-mode FBS, leading to two APDs, $D1$a and $D1$b.

After a storage time of 200 ns, the atoms are excited by a strong, 190 ns read pulse resonant with the $|s\rangle \rightarrow |e\rangle$ transition. This pulse maps the stored collective state into the state of a second light mode, field 2, leaving the whole ensemble again in state $|g\rangle$. Field 2 is then directed to the analysis by a single-mode FBS, leading again to two APDs, $D2$a and $D2$b.

As observed in Fig. 33, we use a combination of additional $\lambda/4$ and $\lambda/2$ plates, compared to the experimental setup for linear polarizations (see Fig. 28), to transmit only the photons with the correct polarizations. With the exception of these modifications, the remaining aspects of our first series of experiments remained unchanged.

On the other hand, in order to directly address the superradiant aspects of the problem, we now focus only on the single- and two-photon wavepackets of the retrieved photons on field 2. Our guide are the theoretical expressions derived in section 2.6 [see Eqs. (2.6.44), (2.6.46) and (2.6.47)]. The measurement of these wavepackets was performed for two different ODs. The single-(cyan curves) and two-photon (squares) wavepackets are

[5]The use of IMs instead of AOMs to control the duration of the read and optical pump pulses is motivated by two reasons: first, because the optical pump pulse has to be switched fast enough so that it does not interfere in the temporal window where the write pulse is acting on the ensemble; and secondly, because the read pulse has to be as close as possible to a rectangular pulse to be able to compare our measured wavepackets with their respective theoretical predictions derived in section 2.6.

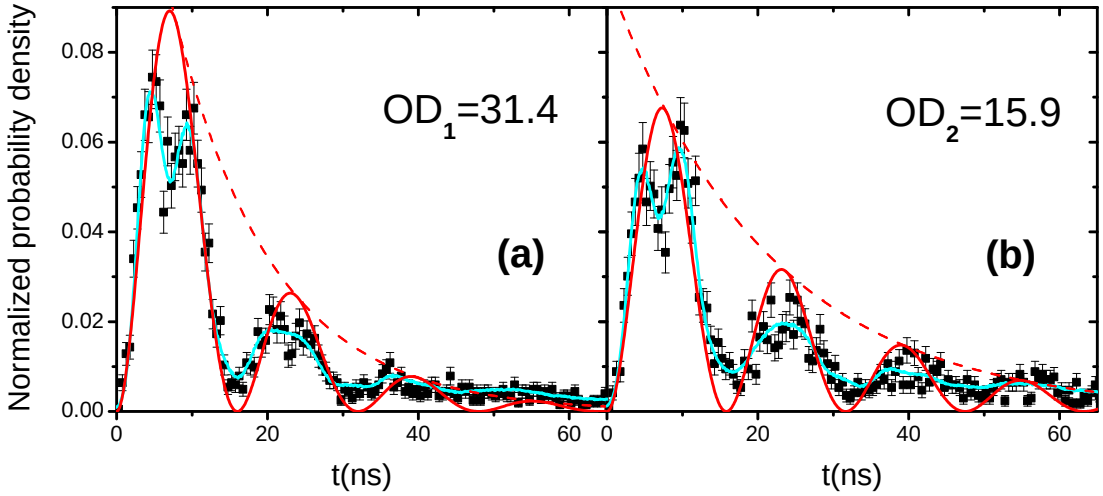

Figure 35: **Single-photon wavepackets (cyan curves)** for OD_1 (a) and OD_2 (b), compared to their respective independent-detections two-photon wavepackets (squares curves). Red solid lines provide the corresponding theoretical curves according to Eq. (2.6.44). Dashed lines plot the respective pure exponential decays.

plotted in Fig. 35 for $p_1 = 0.015$ and a read-beam power of 3.95 mW. For each OD, around 10^{10} sampling periods were used to generate the graphs. The cyan curve on Fig. 35(a) is the measured single-photon wavepacket for our maximum optical deph ($OD_1 = 31.4$), which corresponds to $N \approx 1.9 \times 10^6$ Rubidium atoms [de Oliveira 2014]. Since $OD \propto N$, maximum OD enhances the collective effects behind superradiance. Other important parameters for this curve are $\Delta t = 0.5$ ns, $p_c = 6.27\%$, and $g_{12} = 7.50$. The red curve in this figure provides the theory of Eq. (2.6.44), for $\Omega_0 = 0.4 \times 10^9$rad/s, $\chi = 4.0$, and $\Gamma/2\pi = 6.065$ MHz (natural linewidth of $|e\rangle$). The numerical values for Ω_0 and χ were assumed in order to match the observed Rabi oscillation and its exponential decay, respectively. These theoretical values would correspond to a read-beam power of 2.1 mW and $N \approx 1.1 \times 10^6$ [de Oliveira 2014], lying within a factor of two of our estimation for these experimental parameters.

The cyan curve on Fig. 35(b) represents the measured single-photon wavepacket with the optical depth reduced to $OD_2 = 15.9$. The red curve is for $\chi = 2.52 = 1+(4.0-1)(OD_2/OD_1)$, since $\chi-1$ and OD are both proportional to N [Mendes 2013b,de Oliveira 2014]. Other important parameters for this curve are $p_c = 4.5\%$ and $g_{12} = 6.35$. It can be seen that the modification of the number of atoms changes the superradiant decay rate, but not the frequency of the Rabi oscillations. On the other hand, once again it is interesting to note that the independent-detections two-photon wavepacket (squares curves in Fig. 35) is almost identical to the single-photon wavepacket for the two ODs considered, indicating a possible independence in the emission of the two field-2 photons.

The measured single-photon wavepackets on Fig. 35 follow Eq. (2.6.44) with a few remarks. For start, the first minimum of the experimental curves, at $t = 7$ ns, has no

relation to the underlining dynamics we are investigating, coming from a small ringing on the beginning of the read pulse that we were not able to fully eliminate. Note that its temporal position does not vary with optical depth. Moreover, we also verify that it does not vary with read power [Ortiz-Gutiérrez 2018]. Second, the single-photon wavepacket reaches a small plateau for long times. This comes from a larger noise level due to the fact that we do not use any frequency filter in field 1, resulting in significant increase in TGR, up to 40 Hz. Finally, the number of atoms was changed by a relatively small amount between the cyan curves in Fig. 35, to avoid decreasing the rate of four-photons detections. Both compromises to improve the count rates were crucial for the two-photon wavepackets measurements.

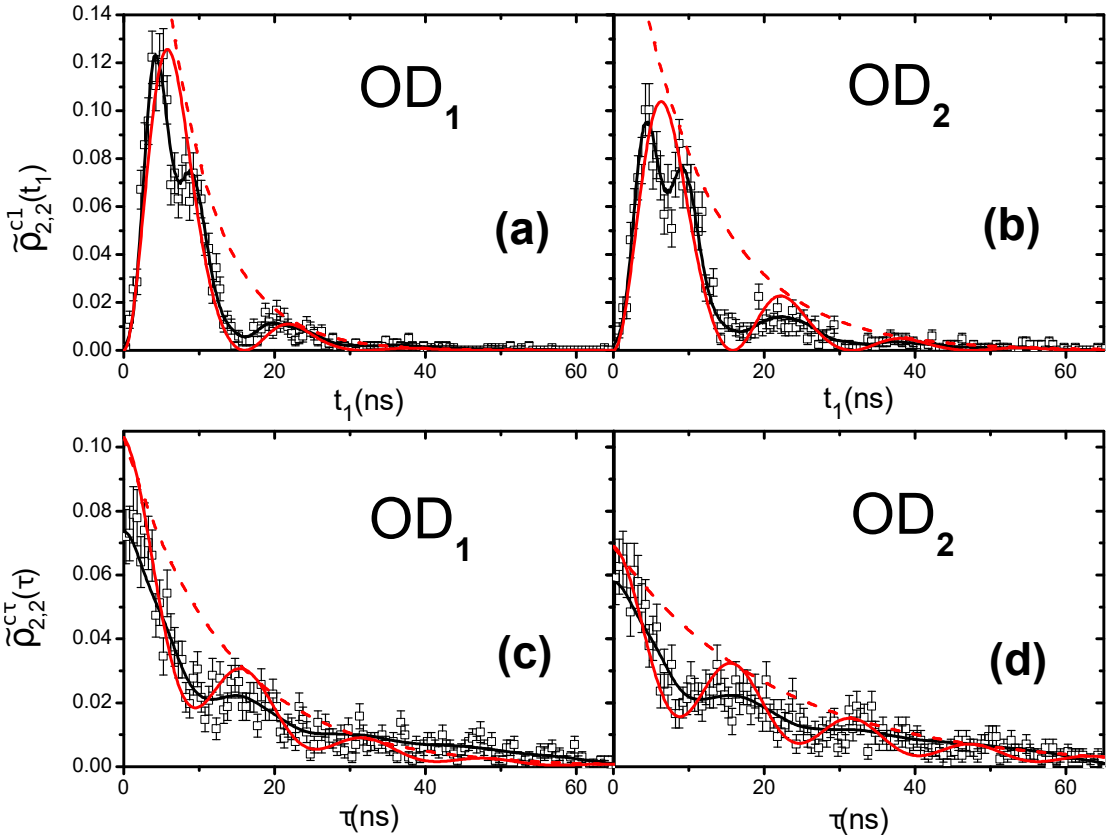

Figure 36: **Two-photon wavepackets** for circular polarizations and optical pumping. Panels (a) and (b): Normalized probability density $\widetilde{\rho}^{c1}_{2,2}(t_1)$ to detect the first field-2 photon at time t_1. Panels (c) and (d): Normalized probability density $\widetilde{\rho}^{c\tau}_{2,2}(\tau)$ to detect the second field-2 photon at time τ after the first detection. Data on panels (a) and (c) [(b) and (d)] resulted from the same measurements as for the experimental cyan curve on Fig. 35(a) [Fig. 35(b)]. Red solid lines provide the theory from Eqs. (2.6.46) and (2.6.47), for the same parameters of the red curves in Fig 35. Dashed lines plot the respective pure exponential decays. Black solid lines plot the respective numerical two-photon wavepackets.

Finally, our measurements for the complete superradiant two-photon wavepackets are shown in more details in Fig. 36 for the two optical depths of Fig. 35. Note that the corresponding numerical two-photon wavepackets have also been included (black curves). Figures 35(a) and 35(c) were obtained for OD_1, and figures 35(b) and 35(d) for OD_2. In panels (a) and (b) we plot the normalized probability density $\widetilde{\rho}^{c1}_{2,2}(t_1)$ of detecting the

first photon of the pair in field 2 at a time t_1 after turning on the read field. In panels (c) and (d) we plot the normalized conditional probability density $\widetilde{\rho}^{c\tau}_{2,2}(\tau)$ of detecting the second photon of the pair at a time τ after the first one. Our largest rate of four-photon generation, for OD_1, was 14 mHz. Equation (2.6.46) [(2.6.47)] is plotted as the red curves on Figs. 35(a) and 35(b) [35(c) and 35(d)], for the same parameters, respectively, as the red curves of Figs. 35(a) and 35(b). The results of Eqs. (2.6.46) and (2.6.47) capture the essential aspects of the measured two-photon wavepackets, with the decay of $\widetilde{\rho}^{c1}_{2,2}(t_1)$ with twice the rate of $\widetilde{\rho}^{c\tau}_{2,2}(\tau)$and Rabi oscillations in both curves. Moreover, it is interesting to note that the numerical two-photons wavepackets successfully describe all the experimental curves in Fig 36, including the first spurious minimum. All these results clearly demonstrate the superradiant emission of the biphoton, with the proper enhanced decay rates, and largely validates our hypothesis of independence in the emission of the two photons. These results are consistent with Dicke's theory for superradiance [Dicke 1954], which also neglects interactions between the outgoing photons.

As a complement to the measures presented in this second stage of our series of experiments, a statistical characterization of fields 1 and 2 will be presented in the next subsection with the main purpose of characterizing the quantum state of the system. This will also help us to demonstrate the existence of quantum correlations between the photons emitted in fields 1 and 2.

4.2.3 *Statistical characterization of the fields*

As discussed in subsection 2.6.1, the ideal joint state between the photons emitted in field 1 and the associated CAEs, is described by a two-mode squeezed vacuum state as [see Eq. (2.6.4)]

$$|\psi_{a,1}\rangle = \sqrt{1-p}\left[|0_a\rangle|0_1\rangle + \sqrt{p}\,|1_a\rangle|1_1\rangle + p\,|2_a\rangle|2_1\rangle + \mathcal{O}\left(p^{3/2}\right)\right], \tag{4.2.13}$$

where the parameter p indicates, for $p \ll 1$, the probability to create a single CAE correlated with a single photon in field 1. Using non-number-resolving detection with low efficiency (the usual case), no detection in field 1 ideally projects the ensemble in the state

$$|\psi_0\rangle \propto |0_a\rangle + p^{1/2}|1_a\rangle + p\,|2_a\rangle + p^{3/2}|3_a\rangle + \ldots \quad . \tag{4.2.14}$$

On the other hand, one and two detections in field 1 would result in the states

$$|\psi_1\rangle \propto |1_a\rangle + p^{1/2}|2_a\rangle + p\,|3_a\rangle + \ldots \quad , \tag{4.2.15}$$

and

$$|\psi_2\rangle \propto |2_a\rangle + p^{1/2}\,|3_a\rangle + \ldots \quad , \tag{4.2.16}$$

respectively.

In order to experimentally characterize the quantum state of our atomic memory and test how close it is to the ideal state given by Eq. (4.2.13), two modifications had to be introduced on the setup of Fig. 33. First, the single-mode FBS in field 2 was substituted by a Time-Multiplexing Detection (TMD) apparatus, consisting of a sequence of two single-mode FBS with a fiber loop delaying in 100 ns one of the arms in the middle (left side in Fig. 37). The outputs of the second FBS reach two detectors (D_{2a},D_{2b}). This apparatus corresponds to a cascade of beam splitters leading to four detectors [Fitch 2003], as shown on the right side in Fig. 37, with D'_{2a},D'_{2b} representing the 100 ns delayed responses of D_{2a},D_{2b}. Second, the read pulse duration was decreased to 30 ns. With these modifications, our experimental setup was prepared for the detection of up to two photons in field 1 and up to four photons in field 2.

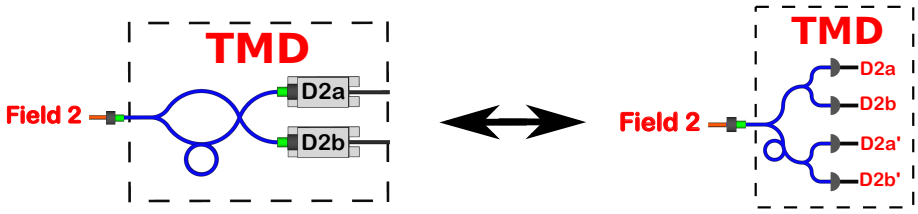

Figure 37: Time-Multiplexing Detection (TMD) apparatus.

The photon-number analysis of field 2 conditioned on zero, one, or two detections in field 1 are presented in Figs. 38(a), 38(b) and 38(c), respectively, as a function of the probability p_1 for a detection in field 1 (ratio between number of detections in field 1 and number of sampling periods). P_{ij} indicates the probability for j detections in field 2 conditioned on i detections in field 1. In this way, Fig. 38(a) plots the values of $P_{0,j}$, related to $|\psi_0\rangle$, Fig. 38(b) the values of $P_{1,j}$, related to $|\psi_1\rangle$, and Fig. 38(c) the values of $P_{2,j}$, related to $|\psi_2\rangle$. The three panels were obtained from the same data set. Error bars come from the uncertainty in the accumulation of detection events, proportional to the square root of the number of detections.

To compare Fig. 38 to the predictions of Eq. (4.2.13), note that $p_1 \approx \eta_1 p$, with η_1 the detection efficiency. As p_1 decreases, with decreasing write intensities, we observe two plateaus forming for $P_{1,1}$ and $P_{2,2}$, since those quantities should be roughly independent of p in this limit [see Eqs. (4.2.15) and (4.2.16) for $|\psi_1\rangle$ and $|\psi_2\rangle$, respectively]. Although $P_{0,0}$ has not been plotted in Fig. 38(a), it also remains constant (at a value very close to 1) when p1 decreases. For perfect detection, 100% efficiency and number resolving, we should not see a $P_{2,1}$. However, in our limit of low efficiency, the loss of a photon in the pair leads to a plateau on $P_{2,1}$ with twice (≈ 0.017) the value of $P_{1,1}$ (≈ 0.0085), since now two photons enter the TMD apparatus.

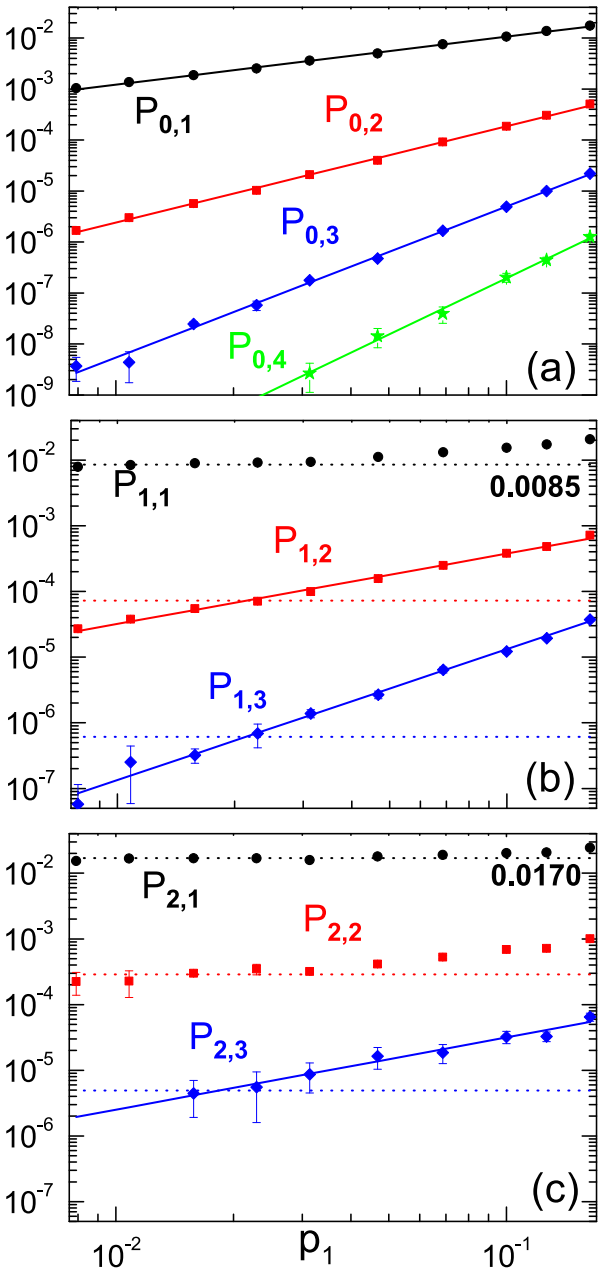

Figure 38: Log-log graphs of probabilities $P_{i,j}$ to detect j photons in field 2 conditioned on the detection of i photons in field 1 as a function of the probability p_1 to detect one photon in field 1, with $i = 0$ (a), 1 (b) and 2 (c). Circles, squares, diamonds and triangles plot the probabilities of detecting one, two, three and four photons in field 2. The solid lines are linear fits. The dashed lines provide the values for the plateau of $P_{1,1}$ and $P_{2,1}$[0.0085 for (b) and 0.0170 for (c)]. The red and blue dashed lines gives the square and cube, respectively, of the black one, corresponding to the Poisson levels for the two and three photons components.

Fock states $|0_a\rangle$, $|1_a\rangle$ and $|2_a\rangle$ are limits of $|\psi_0\rangle$, $|\psi_1\rangle$ and $|\psi_2\rangle$ when $p \to 0$. For finite p, there are always some higher order components. For instance, from Eq. (4.2.14) we expect the probabilities $P_{0,1}$, $P_{0,2}$, $P_{0,3}$ and $P_{0,4}$ to decrease proportionally to p, p^2, p^3 and p^4, respectively. From the log-log plot in Fig. 38(a), we obtain $P_{0,1} \propto p_1^{s_{01}}$, $P_{0,2} \propto p_1^{s_{02}}$, $P_{0,3} \propto p_1^{s_{03}}$ and $P_{0,4} \propto p_1^{s_{04}}$, with $s_{01} = 0.94 \pm 0.01$, $s_{02} = 1.89 \pm 0.02$, $s_{03} = 2.96 \pm 0.07$ and $s_{04} = 3.67 \pm 0.11$, as expected. From Eq. (4.2.15), on the other hand, we expect $P_{1,2} \propto p$ and $P_{1,3} \propto p^2$. From the log-log plot in Fig. 38(b), we obtain $P_{1,2} \propto p_1^{s_{12}}$ and $P_{1,3} \propto p_1^{s_{13}}$, with $s_{12} = 1.07 \pm 0.02$ and $s_{13} = 1.99 \pm 0.07$, once again compatible with the expected. Finally, from Eq. (4.2.16), we expect $P_{2,3}$ to be proportional to p, obtaining $P_{2,3} \propto p_1^{s_{23}}$ with $s_{23} = 1.10 \pm 0.07$ from Fig 38(c). All these results allow us to conclude that the Fock states of our system comes from the two-mode squeezed vacuum state given by Eq. (4.2.13).

Finally, besides observing the predicted suppression of higher order components in the reading process of an atomic memory with one or two CAEs, it is also interesting to compare some of their values to the expectation for a coherent state with single-photon components consistent with the plateaus of Figs. 38(b) and 38(c) (upper dashed lines). In both panels, the dashed lines in the middle and on the bottom give the square and the cube of the value for the upper line, the expected results for a coherent state. We measure then clear suppressions of $P_{1,2}$ and $P_{1,3}$ down to sub-poissonian levels. On the other hand, due to the low efficiency for detecting coincidences between five events (two in field 1 and three in field 2), we could not measure $P_{2,3}$ in a clear sub-poissonian regime.

4.3 Summary of experimental results

In what follows, we summarize the main results of our series of experiments in the previous section.

In the first one, described in subsection 4.2.1, we employed an experimental configuration with linear polarizations on all fields and without optical pumping to a specific Zeeman sublevel. The results allowed for an investigation on the independence of the photons on the two-photon superradiant emission, but not for a direct comparison with the final theoretical expressions deduced on subsection 2.6.3. The experimental wavepackets clearly presented beatings coming from the various Rabi oscillations involved in the reading process through different Zeeman sublevels, while the theory considered a simpler three-level atom in Λ configuration.

In the second stage of the experiments, described in subsection 4.2.2, we optically pumped the atoms to a specific Zeeman sublevel and employed circular polarizations for all fields, in order to guarantee a single Rabi frequency on the reading process. We also observed a significant enhancement on the Rabi oscillations by turning on faster the read beam, through the use of an in-fiber intensity modulator, which approximates

the experiment to the theoretical assumption of a step function for the turning on of the read field. With these modifications, we were finally able to directly compare our experimental wavepackets to the theory of section 2.6, reaching a reasonable agreement. As in subsection 4.2.1, we also analyzed for this new configuration the independence of the two emitted photons in the two-photon superradiant wavepacket, by directly comparing it to the expected results obtained from the experimental single-photon wavepackets.

Finally, in a third stage of experiments, we introduced a TMD system for the field extracted in the reading process. This allowed us to detect up to four photons on the superradiantly emitted field, and to characterize it, then, up to this amount of photons on the Fock basis. Such analysis offered an important support for our claim that the Fock states in our system comes from the two-mode squeezed vacuum state, expected to be generated in our experimental conditions [Duan 2001]. It also offers some measure for the purity of the superradiant Fock states as a function of the probability to generate the corresponding collective states on the write process.

5 Conclusions

OPO

In the continuous variables domain, the combined use of self-homodyning [Villar 2004] and demodulation by in-quadrature local oscillators [Barbosa 2013c] allows the complete reconstruction of the state of the six modes of the field in a triply resonant OPO operating above the threshold. These modes are related to the sidebands of the downconverted fields, generated by the nonlinear process, and the pump field, reflected by the cavity. The experimental results obtained in a scientific collaboration with Marcelo Martinelli's group, at IFUSP, are in good agreement with the detailed model developed in this thesis, involving the transformation of the field operators in their reflection by the cavity, the nonlinear coupling among the fields by the crystal and the photon-phonon coupling. For the chosen linear approach, the model reproduces the so-called "semiclassical model" of the OPO, where quantized fields can be associated to stochastic fluctuations in a Langevin equation, leading to a spectral matrix, associated with the Fourier transform of the two-time correlation of the output fields. In the present case, discrepancies between the model and the semiclassical one are smaller than 4% of the standard quantum level (except for the amplitude variance of the pump, reaching 9%) being both compatible with the experimental results.

The main result of the developed model is the demonstration that the imaginary part of the spectral matrix, i.e. the correlations between symmetric and asymmetric combinations of sidebands [Barbosa 2013c], has not its physical origin in the nonlinear process but on the evolution of the fields inside the cavity, combined with the effective beam splitter transformation for downconverted and pump modes, explicitly derived in the linearized model. This particular effect is not explicit in the semiclassical treatment. The asymmetries in phase evolution of upper and lower sidebands lead to the coupling of their symmetric and antisymmetric combinations. These effects are more important for low analysis frequencies and are maximized as they get closer to the OPO cavity bandwidth.

Using the PPT criterion in the continuous variables regime, the entanglement structure in this system is experimentally and theoretically investigated. We were able to show

that the system presents hexapartite entanglement for pump powers in the range from 1.1 to 1.6 times the oscillation threshold. More specifically, entanglement is revealed by stronger violations if the modes directly coupled by two-mode squeezing are split, but the beam splitter operations acting recursively over the modes in the cavity feedback lead to multimode entanglement involving all the fields. Better results can be expected if phonon noise is suppressed.

Finally, it is curious that the former tripartite treatment of the problem, although valid, does not explore the stronger entanglement in this system. Much better results are obtained using a single mode, or playing with smart combinations of modes. This will be relevant for applications of this source in future quantum communication protocols, like teleportation of entanglement swapping.

Cold atomic ensemble

From a cold atomic ensemble of ^{87}Rb and implementing a "write-read" scheme of counter-propagating beams, inspired by the DLCZ protocol, successfully generation and characterization of the quantum state between individual photons in a mode of the electromagnetic field and CAEs were achieved, which is compatible with a two-mode squeezed vacuum state, as expected. The state characterization is done through a photon statistics analysis of the emitted light in the writing and reading process for different probabilities of excitation of the atoms.

We also investigated the temporal dynamics of the photons emitted during the reading process. To do so, we measure the wavepackets of the single-photon and bi-photon emissions, evidencing superradiant acceleration in both cases. The photon statistics analysis confirmed that the emitted light was close to Fock states. We show that the theoretical models presented in [Mendes 2013b] and [Barros 2018] successfully interprets this superradiant behavior in the Fock-state regimes with one and two photons, respectively.

There are still experimental features to improve in the system both in terms of four-photon generation rate and number of atoms in the ensemble. Larger generation rates may lead to purer single- and two-excitation states, but also to investigations of larger collective states, with three or four excitations. On the other hand, larger number of atoms, through larger optical depths of the atomic ensemble, may lead to different superradiant regimes, possibly presenting some interaction between the extracted photons which in turn will present an additional challenge in the detection system. All these developments point out to the feasibility of a new approach to generate and control larger and purer Fock states connected to long-lived atomic memories, useful for quantum metrology [Holland 1993] and helping to lift the usually assumed restriction to single-photon sources as a possible resource in the designing of new quantum information protocols [van Loock 2011].

References

[Adesso 2004] Gerardo Adesso, Alessio Serafini and Fabrizio Illuminati. *Extremal entanglement and mixedness in continuous variable systems*. Phys. Rev. A, vol. 70, page 022318, Aug 2004.

[Araújo 2016] Michelle O. Araújo, Ivor Krešić, Robin Kaiser and William Guerin. *Superradiance in a Large and Dilute Cloud of Cold Atoms in the Linear-Optics Regime*. Phys. Rev. Lett., vol. 117, no. 7, page 073002, August 2016.

[Barbosa 2010] F. A. S. Barbosa, A. S. Coelho, A. J. de Faria, K. N. Cassemiro, A. S. Villar, P. Nussenzveig and M. Martinelli. *Robustness of bipartite Gaussian entangled beams propagating in lossy channels*. Nat. Photonics, vol. 4, page 858, Aug 2010.

[Barbosa 2013a] F. A. S. Barbosa. *Robustez do Emaranhamento em Variáveis Contínuas e Fotodetecção de Feixes Intensos no Domínio Espectral*. PhD thesis, Universidade de São Paulo, 2013.

[Barbosa 2013b] F. A. S. Barbosa, A. S. Coelho, K. N. Cassemiro, P. Nussenzveig, C. Fabre, M. Martinelli and A. S. Villar. *Beyond Spectral Homodyne Detection: Complete Quantum Measurement of Spectral Modes of Light*. Phys. Rev. Lett., vol. 111, page 200402, Nov 2013.

[Barbosa 2013c] F. A. S. Barbosa, A. S. Coelho, K. N. Cassemiro, P. Nussenzveig, C. Fabre, A. S. Villar and M. Martinelli. *Quantum state reconstruction of spectral field modes: Homodyne and resonator detection schemes*. Phys. Rev. A, vol. 88, page 052113, Nov 2013.

[Barbosa 2017] F. A. S. Barbosa, A. S. Coelho, L. F. Muñoz Martínez, L. Ortiz-Gutiérrez, A. S. Villar, P. Nussenzveig and M. Martinelli. *Hexapartite entanglement in a CW Optical Parametric Oscillator*. ArXiv e-prints, 1712.01756, December 2017.

[Barros 2018] D. F. Barros, L. F. Muñoz Matínez, L. Ortiz-Gutiérrez, R. S. N. Moreira, J. E. O. Morales, N. D. Alves, A. F. G. Tieco, D. Felinto and P. L. Saldanha. *Fock-State Superradiance in a Cold Atomic Ensemble*. In preparation, 2018.

[Bennett 1992] Charles H. Bennett and Stephen J. Wiesner. *Communication via one- and two-particle operators on Einstein-Podolsky-Rosen states.* Phys. Rev. Lett., vol. 69, pages 2881–2884, Nov 1992.

[Bennett 1993] Charles H. Bennett, Gilles Brassard, Claude Crépeau, Richard Jozsa, Asher Peres and William K. Wootters. *Teleporting an unknown quantum state via dual classical and Einstein-Podolsky-Rosen channels.* Phys. Rev. Lett., vol. 70, pages 1895–1899, Mar 1993.

[Bimbard 2010] Erwan Bimbard, Nitin Jain, Andrew MacRae and A. I. Lvovsky. *Quantum-optical state engineering up to the two-photon level.* Nature Photonics, vol. 4, page 243, February 2010.

[Boller 1991] K-J Boller, A Imamoğlu and Stephen E Harris. *Observation of electromagnetically induced transparency.* Phys. Rev. Lett., vol. 66, no. 20, page 2593, 1991.

[Boyd 1992] R. W. Boyd. Nonlinear optics. Academic Press, Inc., San Diego, 1992.

[Breunig 2011] I. Breunig, D. Haertle and K. Buse. *Continuous-wave optical parametric oscillators: recent developments and prospects.* Applied Physics B, vol. 105, no. 1, page 99, Sep 2011.

[Briegel 1998] H.-J. Briegel, W. Dür, J. I. Cirac and P. Zoller. *Quantum Repeaters: The Role of Imperfect Local Operations in Quantum Communication.* Phys. Rev. Lett., vol. 81, pages 5932–5935, Dec 1998.

[Burnham 1970] David C Burnham and Donald L Weinberg. *Observation of simultaneity in parametric production of optical photon pairs.* Phys. Rev. Lett., vol. 25, no. 2, page 84, 1970.

[Cassemiro 2007] K. N. Cassemiro, A. S. Villar, M. Martinelli and P. Nussenzveig. *The quest for three-color entanglement: experimental investigation of new multipartite quantum correlations.* Opt. Express, vol. 15, no. 26, pages 18236–18246, Dec 2007.

[Cassemiro 2008a] K. N. Cassemiro. *Correlações Quânticas Multicolor no Oscilador Paramétrico Ótico.* PhD thesis, Universidade de Sao Paulo, 2008.

[Cassemiro 2008b] Katiuscia N. Cassemiro and Alessandro S. Villar. *Scalable continuous-variable entanglement of light beams produced by optical parametric oscillators.* Phys. Rev. A, vol. 77, page 022311, Feb 2008.

[Cavalcanti 2008] Daniel Cavalcanti. *Entanglement: from its mathematical description to its experimental observation.* PhD thesis, Universitat de Barcelona, 2008.

[Caves 1981] Carlton M. Caves. *Quantum-mechanical noise in an interferometer.* Phys. Rev. D, vol. 23, pages 1693–1708, Apr 1981.

[César 2009] J. E. S. César, A. S. Coelho, K. N. Cassemiro, A. S. Villar, M. Lassen, P. Nussenzveig and M. Martinelli. *Extra phase noise from thermal fluctuations in nonlinear optical crystals.* Phys. Rev. A, vol. 79, page 063816, Jun 2009.

[Chen 2014] Moran Chen, Nicolas C. Menicucci and Olivier Pfister. *Experimental Realization of Multipartite Entanglement of 60 Modes of a Quantum Optical Frequency Comb.* Phys. Rev. Lett., vol. 112, page 120505, Mar 2014.

[Choi 2008] K. S. Choi, H. Deng, J. Laurat and H. J. Kimble. *Mapping photonic entanglement into and out of a quantum memory.* Nature, vol. 452, page 67, March 2008.

[Choi 2010] K. S. Choi, A. Goban, S. B. Papp, S. J. van Enk and H. J. Kimble. *Entanglement of spin waves among four quantum memories.* Nature, vol. 468, page 412, November 2010.

[Chou 2005] C. W. Chou, H. de Riedmatten, D. Felinto, S. V. Polyakov, S. J. van Enk and H. J. Kimble. *Measurement-induced entanglement for excitation stored in remote atomic ensembles.* Nature, vol. 438, page 828, December 2005.

[Chou 2007] Chin-Wen Chou, Julien Laurat, Hui Deng, Kyung Soo Choi, Hugues de Riedmatten, Daniel Felinto and H. Jeff Kimble. *Functional Quantum Nodes for Entanglement Distribution over Scalable Quantum Networks.* Science, vol. 316, no. 5829, page 1316, June 2007.

[Clauser 1974] John F. Clauser. *Experimental distinction between the quantum and classical field-theoretic predictions for the photoelectric effect.* Phys. Rev. D, vol. 9, no. 4, pages 853–860, February 1974.

[Coelho 2009] A. S. Coelho, F. A. S. Barbosa, K. N. Cassemiro, A. S. Villar, M. Martinelli and P. Nussenzveig. *Three-Color Entanglement.* Science, vol. 326, pages 823–826, Nov 2009.

[Coelho 2013] A. S. Coelho. *Emaranhamento Multicolor para Redes de Informaço Quântica.* PhD thesis, Universidade de Sao Paulo, 2013.

[Coelho 2015] A. S. Coelho, F. A. S. Barbosa, K. N. Cassemiro, M. Martinelli, A. S. Villar and P. Nussenzveig. *Analyzing the Gaussian character of the spectral quantum state of light via quantum noise measurements.* Phys. Rev. A, vol. 92, page 012110, Jul 2015.

[Collaboration 2011] The LIGO Scientific Collaboration. *A gravitational wave observatory operating beyond the quantum shot-noise limit.* Nature Phys., vol. 7, pages 962–965, Aug 2011.

[Collett 1984] M. J. Collett and C. W. Gardiner. *Squeezing of intracavity and traveling-wave light fields produced in parametric amplification.* Phys. Rev. A, vol. 30, pages 1386–1391, Sep 1984.

[Collett 1988] MJ Collett. *Exact density-matrix calculations for simple open systems.* Phys. Rev. A, vol. 38, no. 5, page 2233, 1988.

[Cooper 2013] Merlin Cooper, Laura J. Wright, Christoph Söller and Brian J. Smith. *Experimental generation of multi-photon Fock states.* Opt. Express, vol. 21, no. 5, pages 5309–5317, March 2013.

[de Almeida 2016] A. J. F. de Almeida, M.-A. Maynard, C. Banerjee, D. Felinto, F. Goldfarb and J. W. R. Tabosa. *Nonvolatile optical memory via recoil-induced resonance in a pure two-level system.* Phys. Rev. A, vol. 94, no. 6, page 063834, December 2016.

[de Andrade 2017] R. B. de Andrade, B. A. F. Ribeiro, A. G. Arciniegas, P. Nussenzveig and M. Martinelli. *Multipartite entanglement in doubly resonant optical parametric oscillators.* In preparation, 2017.

[de Oliveira 2014] Rafael A de Oliveira, Milrian S Mendes, Weliton S Martins, Pablo L Saldanha, José WR Tabosa and Daniel Felinto. *Single-photon superradiance in cold atoms.* Phys. Rev. A, vol. 90, no. 2, page 023848, 2014.

[Debuisschert 1993] T. Debuisschert, A. Sizmann, E. Giacobino and C. Fabre. *Type-II continuous-wave optical parametric oscillators: oscillation and frequency-tuning characteristics.* J. Opt. Soc. Am. B, vol. 10, no. 9, pages 1668–1680, Sep 1993.

[Deesuwan 2010] T. Deesuwan. Entanglement criteria for continuous-variable states. Master's thesis, Imperial College london, 2010.

[Dicke 1954] Robert H Dicke. *Coherence in spontaneous radiation processes.* Phys. Rev., vol. 93, no. 1, page 99, 1954.

[Duan 2001] L.-M. Duan, M. D. Lukin, J. I. Cirac and P. Zoller. *Long-distance quantum communication with atomic ensembles and linear optics.* Nature, vol. 414, page 413, November 2001.

[Ekert 1991] Artur K. Ekert. *Quantum cryptography based on Bell's theorem.* Phys. Rev. Lett., vol. 67, pages 661–663, Aug 1991.

[Felinto 2005] D Felinto, CW Chou, H De Riedmatten, SV Polyakov and HJ Kimble. *Control of decoherence in the generation of photon pairs from atomic ensembles.* Phys. Rev. A, vol. 72, no. 5, page 053809, 2005.

[Fitch 2003] M. J. Fitch, B. C. Jacobs, T. B. Pittman and J. D. Franson. *Photon-number resolution using time-multiplexed single-photon detectors.* Phys. Rev. A, vol. 68, no. 4, page 043814, October 2003.

[Fleischhauer 2000] M. Fleischhauer and M. D. Lukin. *Dark-State Polaritons in Electromagnetically Induced Transparency.* Phys. Rev. Lett., vol. 84, no. 22, pages 5094–5097, May 2000.

[Foot 2005] C. J. Foot. Atomic physics. Oxford University Press, 2005.

[Furusawa 1998] A. Furusawa, J. L. Sørensen, S. L. Braunstein, C. A. Fuchs, H. J. Kimble and E. S. Polzik. *Unconditional Quantum Teleportation.* Science, vol. 282, no. 5389, pages 706–709, 1998.

[Galatola 1991] P. Galatola, L.A. Lugiato, M.G. Porreca, P. Tombesi and G. Leuchs. *System control by variation of the squeezing phase.* Optics Communications, vol. 85, no. 1, pages 95 – 103, 1991.

[Gattobigio 2010] G L Gattobigio, T Pohl, G Labeyrie and R Kaiser. *Scaling laws for large magneto-optical traps.* Physica Scripta, vol. 81, no. 2, page 025301, 2010.

[Glauber 1963] Roy J. Glauber. *The Quantum Theory of Optical Coherence.* Phys. Rev., vol. 130, pages 2529–2539, Jun 1963.

[Gross 1976] M. Gross, C. Fabre, P. Pillet and S. Haroche. *Observation of Near-Infrared Dicke Superradiance on Cascading Transitions in Atomic Sodium.* Phys. Rev. Lett., vol. 36, no. 17, pages 1035–1038, April 1976.

[Gross 1982a] M. Gross and S. Haroche. *Superradiance: An essay on the theory of collective spontaneous emission.* Physics Reports, vol. 93, no. 5, pages 301–396, December 1982.

[Gross 1982b] Michel Gross and Serge Haroche. *Superradiance: an essay on the theory of collective spontaneous emission.* Phys. Rep., vol. 93, no. 5, pages 301–396, 1982.

[Hammerer 2010] Klemens Hammerer, Anders S Sørensen and Eugene S Polzik. *Quantum interface between light and atomic ensembles.* Rev. Mod. Phys., vol. 82, no. 2, page 1041, 2010.

[Heidmann 1984] A. Heidmann, S. Reynaud and C. Cohen-Tannoudji. *Photon noise reduction and coherence properties of squeezed fields.* Optics Communications, vol. 52, no. 4, pages 235 – 240, 1984.

[Heidmann 1987] A. Heidmann, R. J. Horowicz, S. Reynaud, E. Giacobino, C. Fabre and G. Camy. *Observation of Quantum Noise Reduction on Twin Laser Beams.* Phys. Rev. Lett., vol. 59, pages 2555–2557, Nov 1987.

[Holland 1993] M. J. Holland and K. Burnett. *Interferometric detection of optical phase shifts at the Heisenberg limit.* Phys. Rev. Lett., vol. 71, pages 1355–1358, Aug 1993.

[Hong 1985] CK Hong and L Mandel. *Theory of parametric frequency down conversion of light.* Phys. Rev. A, vol. 31, no. 4, page 2409, 1985.

[Hong 1987] CK Hong, Zhe-Yu Ou and Leonard Mandel. *Measurement of subpicosecond time intervals between two photons by interference.* Phys. Rev. Lett., vol. 59, no. 18, page 2044, 1987.

[Horodecki 1996] Michał Horodecki, Paweł Horodecki and Ryszard Horodecki. *Separability of mixed states: necessary and sufficient conditions.* Physics Letters A, vol. 223, no. 1, pages 1 – 8, 1996.

[Ismail 2016] Nur Ismail, Cristine Calil Kores, Dimitri Geskus and Markus Pollnau. *Fabry-Pérot resonator: spectral line shapes, generic and related Airy distributions, linewidths, finesses, and performance at low or frequency-dependent reflectivity.* Opt. Express, vol. 24, no. 15, pages 16366–16389, Jul 2016.

[Kasai 1997] K. Kasai, Gao Jiangrui and C. Fabre. *Observation of squeezing using cascaded nonlinearity.* EPL (Europhysics Letters), vol. 40, no. 1, page 25, 1997.

[Kuzmich 2003] A. Kuzmich, W. P. Bowen, A. D. Boozer, A. Boca, C. W. Chou, L.-M. Duan and H. J. Kimble. *Generation of nonclassical photon pairs for scalable quantum communication with atomic ensembles.* Nature, vol. 423, page 731, June 2003.

[Lan 2009] S.-Y. Lan, A. G. Radnaev, O. A. Collins, D. N. Matsukevich, T. A. B. Kennedy and A. Kuzmich. *A Multiplexed Quantum Memory.* Opt. Express, vol. 17, no. 16, pages 13639–13645, August 2009.

[Laurat 2006] Julien Laurat, Hugues de Riedmatten, Daniel Felinto, Chin-Wen Chou, Erik W. Schomburg and H. Jeff Kimble. *Efficient retrieval of a single excitation stored in an atomic ensemble.* Opt. Express, vol. 14, no. 15, pages 6912–6918, Jul 2006.

[Laurat 2007] Julien Laurat, Chin wen Chou, Hui Deng, Kyung Soo Choi, Daniel Felinto, Hugues de Riedmatten and H J Kimble. *Towards experimental entanglement connection with atomic ensembles in the single excitation regime.* New Journal of Physics, vol. 9, no. 6, page 207, 2007.

[Law 1995] C. K. Law. *Interaction between a moving mirror and radiation pressure: A Hamiltonian formulation.* Phys. Rev. A, vol. 51, pages 2537–2541, Mar 1995.

[Mandel 1995] Leonard Mandel and Emil Wolf. Optical coherence and quantum optics. Cambridge university press, 1995.

[Martinelli 2002] M Martinelli. *Compressão de Ruído Quântico e Efeitos Transversos em Osciladores Paramétricos Óticos.* PhD thesis, Universidade de Sao Paulo, 2002.

[Mendes 2011] Milrian S. Mendes and Daniel Felinto. *Perspectives for laboratory implementation of the Duan-Lukin-Cirac-Zoller protocol for quantum repeaters.* Phys. Rev. A, vol. 84, page 062303, Dec 2011.

[Mendes 2013a] Milrian da Silva Mendes. *Dinâmica do processo de leitura de memórias quânticas em átomos frios.* Tese de Doutorado., 2013.

[Mendes 2013b] Milrian S Mendes, Pablo L Saldanha, José W R Tabosa and Daniel Felinto. *Dynamics of the reading process of a quantum memory.* New Journal of Physics, vol. 15, no. 7, page 075030, 2013.

[Monken 2013] Carlos Monken and Pablo L. Saldanha. *Interaction Between Light and Matter: A Photon Wave Function Approach.* The Rochester Conferences on Coherence and Quantum Optics and the Quantum Information and Measurement meeting, 2013.

[Moretti 2008] D. Moretti, N. Gonzalez, D. Felinto and J. W. R. Tabosa. *Dynamics of Bragg diffraction in a stored light grating in cold atoms.* Phys. Rev. A, vol. 78, no. 2, page 023811, August 2008.

[Muñoz Martínez 2017] L. F. Muñoz Martínez, F. A. S. Barbosa, A. S. Coelho, L. Ortíz-Gutiérrez, M. Martinelli, P. Nussenzveig and A. S. Villar. *Exploring six modes of an optical parametric oscillator.* arXiv:1710.02905, 2017.

[Ortiz-Gutiérrez 2017] L. Ortiz-Gutiérrez. *Application of atomic systems for computation and fundamental studies on superradiance.* PhD thesis, Universidade Federal de Pernambuco, 2017.

[Ortiz-Gutiérrez 2018] L. Ortiz-Gutiérrez, L. F. Muñoz Martínez, D. F. Barros, J. E. O. Morales, R. S. N. Moreira, N. D. Alves, A. F. G. Tieco, P. L. Saldanha and

D. Felinto. *Experimental Fock-State Superradiance.* Phys. Rev. Lett., vol. 120, page 083603, Feb 2018.

[Ou 1992] Z. Y. Ou, S. F. Pereira, H. J. Kimble and K. C. Peng. *Realization of the Einstein-Podolsky-Rosen paradox for continuous variables.* Phys. Rev. Lett., vol. 68, pages 3663–3666, Jun 1992.

[Ourjoumtsev 2006] Alexei Ourjoumtsev, Rosa Tualle-Brouri and Philippe Grangier. *Quantum Homodyne Tomography of a Two-Photon Fock State.* Phys. Rev. Lett., vol. 96, page 213601, Jun 2006.

[Peres 1996] Asher Peres. *Separability Criterion for Density Matrices.* Phys. Rev. Lett., vol. 77, pages 1413–1415, Aug 1996.

[Pinel 2012] Olivier Pinel, Pu Jian, Renné Medeiros de Araújo, Jinxia Feng, Benoît Chalopin, Claude Fabre and Nicolas Treps. *Generation and Characterization of Multimode Quantum Frequency Combs.* Phys. Rev. Lett., vol. 108, page 083601, Feb 2012.

[Pu 2017] Y.-F. Pu, N. Jiang, W. Chang, H.-X. Yang, C. Li and L.-M. Duan. *Experimental realization of a multiplexed quantum memory with 225 individually accessible memory cells.* Nature Communications, vol. 8, page 15359, May 2017.

[Raab 1987] E. L. Raab, M. Prentiss, Alex Cable, Steven Chu and D. E. Pritchard. *Trapping of Neutral Sodium Atoms with Radiation Pressure.* Phys. Rev. Lett., vol. 59, pages 2631–2634, Dec 1987.

[Radnaev 2010] A. G. Radnaev, Y. O. Dudin, R. Zhao, H. H. Jen, S. D. Jenkins, A. Kuzmich and T. A. B. Kennedy. *A quantum memory with telecom-wavelength conversion.* Nature Physics, vol. 6, page 894, September 2010.

[Reid 1988] M. D. Reid and P. D. Drummond. *Quantum Correlations of Phase in Nondegenerate Parametric Oscillation.* Phys. Rev. Lett., vol. 60, pages 2731–2733, Jun 1988.

[Reid 1989] M. D. Reid and P. D. Drummond. *Correlations in nondegenerate parametric oscillation: Squeezing in the presence of phase diffusion.* Phys. Rev. A, vol. 40, pages 4493–4506, Oct 1989.

[Roof 2016] S. J. Roof, K. J. Kemp, M. D. Havey and I. M. Sokolov. *Observation of Single-Photon Superradiance and the Cooperative Lamb Shift in an Extended Sample of Cold Atoms.* Phys. Rev. Lett., vol. 117, no. 7, page 073003, August 2016.

[Sangouard 2011] Nicolas Sangouard, Christoph Simon, Hugues de Riedmatten and Nicolas Gisin. *Quantum repeaters based on atomic ensembles and linear optics*. Rev. Mod. Phys., vol. 83, pages 33–80, Mar 2011.

[Schumaker 1984] Bonny L. Schumaker. *Noise in homodyne detection*. Opt. Lett., vol. 9, no. 5, pages 189–191, May 1984.

[Scully 1997] M. O. Scully and M. S. Zubairy. Quantum optics. New York: Cambridge University Press, 1997.

[Shapiro 1979] J. Shapiro, H. Yuen and A. Mata. *Optical communication with two-photon coherent states–Part II: Photoemissive detection and structured receiver performance*. IEEE Transactions on Information Theory, vol. 25, no. 2, pages 179–192, March 1979.

[Shapiro 1985] J. Shapiro. *Quantum noise and excess noise in optical homodyne and heterodyne receivers*. IEEE Journal of Quantum Electronics, vol. 21, no. 3, pages 237–250, Mar 1985.

[Simon 1987] R. Simon, E. C. G. Sudarshan and N. Mukunda. *Gaussian-Wigner distributions in quantum mechanics and optics*. Phys. Rev. A, vol. 36, pages 3868–3880, Oct 1987.

[Simon 1994] R. Simon, N. Mukunda and Biswadeb Dutta. *Quantum-noise matrix for multimode systems: U(n) invariance, squeezing, and normal forms*. Phys. Rev. A, vol. 49, pages 1567–1583, Mar 1994.

[Simon 2000] R. Simon. *Peres-Horodecki Separability Criterion for Continuous Variable Systems*. Phys. Rev. Lett., vol. 84, pages 2726–2729, Mar 2000.

[Simon 2007a] Christoph Simon, Hugues de Riedmatten, Mikael Afzelius, Nicolas Sangouard, Hugo Zbinden and Nicolas Gisin. *Quantum Repeaters with Photon Pair Sources and Multimode Memories*. Phys. Rev. Lett., vol. 98, page 190503, May 2007.

[Simon 2007b] Jonathan Simon, Haruka Tanji, James K. Thompson and Vladan Vuletić. *Interfacing Collective Atomic Excitations and Single Photons*. Phys. Rev. Lett., vol. 98, page 183601, May 2007.

[Skribanowitz 1973] N. Skribanowitz, I. P. Herman, J. C. MacGillivray and M. S. Feld. *Observation of Dicke Superradiance in Optically Pumped HF Gas*. Phys. Rev. Lett., vol. 30, no. 8, pages 309–312, February 1973.

[Steck 2015] Daniel A. Steck. *Rubidium 87 D Line Data*. http://steck.us/alkalidata (revision 2.1.5), 2015.

[Takeda 2013] Shuntaro Takeda, Takahiro Mizuta, Maria Fuwa, Peter Van Loock and Akira Furusawa. *Deterministic quantum teleportation of photonic quantum bits by a hybrid technique.* Nature, vol. 500, pages 315–318, Jun 2013.

[Träger 2007] Frank Träger. Handbook of lasers and optics. Springer, 2007.

[van Loock 2011] P. van Loock. *Optical hybrid approaches to quantum information.* Laser & Photonics Reviews, vol. 5, no. 2, pages 167–200, 2011.

[Vidal 2002] G. Vidal and R. F. Werner. *Computable measure of entanglement.* Phys. Rev. A, vol. 65, page 032314, Feb 2002.

[Villar 2004] A.S. Villar, M. Martinelli and P. Nussenzveig. *Testing the entanglement of intense beams produced by a non-degenerate optical parametric oscillator.* Optics Communications, vol. 242, no. 4, pages 551 – 563, 2004.

[Villar 2005] A. S. Villar, L. S. Cruz, K. N. Cassemiro, M. Martinelli and P. Nussenzveig. *Generation of Bright Two-Color Continuous Variable Entanglement.* Phys. Rev. Lett., vol. 95, page 243603, Dec 2005.

[Villar 2006] A. S. Villar, M. Martinelli, C. Fabre and P. Nussenzveig. *Direct Production of Tripartite Pump-Signal-Idler Entanglement in the Above-Threshold Optical Parametric Oscillator.* Phys. Rev. Lett., vol. 97, page 140504, Oct 2006.

[Villar 2007] A. S. Villar. *Emaranhamento Multicolor entre Feixes Intensos de Luz.* PhD thesis, Universidade de Sao Paulo, 2007.

[Villar 2008] Alessandro S. Villar. *The conversion of phase to amplitude fluctuations of a light beam by an optical cavity.* American Journal of Physics, vol. 76, no. 10, pages 922–929, 2008.

[Walls 2008] D. F. Walls and G. J. Milburn. Quantum optics. Springer, 2008.

[Wang 2017] Hailong Wang, Claude Fabre and Jietai Jing. *Single-step fabrication of scalable multimode quantum resources using four-wave mixing with a spatially structured pump.* Phys. Rev. A, vol. 95, page 051802, May 2017.

[Werner 1989] Reinhard F. Werner. *Quantum states with Einstein-Podolsky-Rosen correlations admitting a hidden-variable model.* Phys. Rev. A, vol. 40, pages 4277–4281, Oct 1989.

[Werner 2001] R. F. Werner and M. M. Wolf. *Bound Entangled Gaussian States.* Phys. Rev. Lett., vol. 86, pages 3658–3661, Apr 2001.

[Wu 1986a] Ling-An Wu, H. J. Kimble, J. L. Hall and Huifa Wu. *Generation of Squeezed States by Parametric Down Conversion.* Phys. Rev. Lett., vol. 57, pages 2520–2523, Nov 1986.

[Wu 1986b] Ling-An Wu, HJ Kimble, JL Hall and Huifa Wu. *Generation of squeezed states by parametric down conversion.* Phys. Rev. Lett., vol. 57, no. 20, page 2520, 1986.

[Yokoyama 2013] S. Yokoyama, R. Ukai, S. C. Armstrong, C. Sornphiphatphong, T. Kaji, S. Suzuki, J. Ichi Yoshikawa, H. Yonezawa, N. C. Menicucci and A. Furusawa. *Ultra-large-scale continuous-variable cluster states multiplexed in the time domain.* Nat. Photonics, vol. 7, page 982, Sept 2013.

[Yuan 2008] Zhen-Sheng Yuan, Yu-Ao Chen, Bo Zhao, Shuai Chen, Jörg Schmiedmayer and Jian-Wei Pan. *Experimental demonstration of a BDCZ quantum repeater node.* Nature, vol. 454, page 1098, August 2008.

[Yuen 1978] H. Yuen and J. Shapiro. *Optical communication with two-photon coherent states–Part I: Quantum-state propagation and quantum-noise.* IEEE Transactions on Information Theory, vol. 24, no. 6, pages 657–668, November 1978.

[Yuen 1980] H. Yuen and J. Shapiro. *Optical communication with two-photon coherent states–Part III: Quantum measurements realizable with photoemissive detectors.* IEEE Transactions on Information Theory, vol. 26, no. 1, pages 78–92, Jan 1980.

[Yuen 1983] Horace P. Yuen and Vincent W. S. Chan. *Noise in homodyne and heterodyne detection.* Opt. Lett., vol. 8, no. 3, pages 177–179, Mar 1983.

[Yurke 1985a] Bernard Yurke. *Squeezed-coherent-state generation via four-wave mixers and detection via homodyne detectors.* Phys. Rev. A, vol. 32, pages 300–310, Jul 1985.

[Yurke 1985b] Bernard Yurke. *Wideband photon counting and homodyne detection.* Phys. Rev. A, vol. 32, pages 311–323, Jul 1985.

[Zhang 2001] K. S. Zhang, T. Coudreau, M. Martinelli, A. Maître and C. Fabre. *Generation of bright squeezed light at 1.06 μm using cascaded nonlinearities in a triply resonant cw periodically-poled lithium niobate optical parametric oscillator.* Phys. Rev. A, vol. 64, page 033815, Aug 2001.